COUPLING CELLS AND BIOMOLECULES WITH CMOS FLOATING GATE TRANSISTORS

A Dissertation

Presented to the Faculty of the Graduate School

of Cornell University

In Partial Fulfillment of the Requirements for the Degree of

Doctor of Philosophy

by

Krishna Jayant

May, 2014

COUPLING CELLS AND BIOMOLECULES WITH CMOS FLOATING GATE TRANSISTORS

Krishna Jayant, Ph. D.

Cornell University 2014

Charge based detection of bio-analytes using field-effect-transistors (FET's) presents an attractive route towards realizing low cost, ultrasensitive and label-free electronic biosensors. The first realization of such a biosensor was based on the Ion-Sensitive Field Effect Transistor (ISFET), developed by Piet Bergveld and has been instrumental in inspiring many FET based bio-sensor designs and concepts. This thesis takes inspiration from the ISFET, builds on well understood CMOS technology, integrates neuromorphic style operation and flash memory principles to realize floating-gate ISFET's capable of charge sensing, simultaneous ionic actuation and co-localized impedance spectroscopy based detection. The device termed the Chemoreceptive Neuron MOS Transistor (CvMOS) is theoretically and experimentally investigated for both biomolecular sensing and secretory analysis from cells.

Chapter 1 describes a brief background to the field of ISFET based biosensing. The relative merits and challenges associated with FET based biosensing are discussed.

Chapter 2 describes the sensor structure, tunneling operation and interface physics under study in this dissertation. The structure takes inspiration from multi-input floating gate memories. The interface between the transistor and the fluid is modeled incorporating effects such as surface equilibrium constants and ion size. Actuation by non-volatile charge injection is introduced and is shown to tune the pH sensitivity thus

realizing a single transistor sensor-actuator hybrid. Multivalent ion induced co-relations such as charge inversion is described.

Chapter 3 describes the device as a DNA sensor. Physics of the DNA-transistor interface is presented. Electric field induced DNA desorption and refreshabilty is discussed. Impedance spectroscopy using split signal delivery is outlined.

Chapter 4 outlines factors that affect DNA detection, role of background electrolyte composition, surface properties and methods to improve sensitivity at the transistor interface.

Chapter 5 introduces the use of split signal delivery and impedance spectroscopy for ultrasensitive pathogenic DNA detection. SPICE simulations depict dominant poles and zeros in the system and their relative dependence on analyte properties. The use of branched Y-DNA motifs and target induced self-assembly are introduced as signal amplification mechanisms pushing the limits of target detection down to ~100fM on CMOS.

Chapter 6 describes the coupling between excitable chromaffin cells and non-excitable RBL-2H3 mast cells with floating gate transistors. The mechanisms of electrochemical and electrical activity detection are discussed. Simultaneous charge and impedance sensing is introduced.

Chapter 7 presents the conclusion and future outlook.

BIOGRAPHICAL SKETCH

Krishna Jayant was born in Chennai, India. His early education was in India and later in the Middle East, namely, Bahrain, Dubai and finally in Muscat. After completing high school from the Indian School in Muscat, Krishna returned to India and enrolled for a B.Tech degree at the National Institute of Technology, Tiruchirappalli (NITT) in the Department of Electrical Engineering. He considers his undergraduate research stint under the supervision of Prof. K. Sundareswaran as an inspirational time, when he researched biologically inspired optimization techniques for power quality improvement. This experience convinced him to pursue academics further and he joined the Indian Institute of Science in Bangalore, as a research assistant to Prof. Navakanta Bhat, working on MEMS. Krishna counts this as a career-defining period in his academic life. In 2006, Krishna was awarded a scholarship to work with Prof. Roberto Guerrieri's group at the University of Bologna, where he worked on portable lab-on-chip technologies for rare cell handling. Armed with this experience, Krishna joined Cornell University's Department of Electrical and Computer Engineering in fall of 2007 for doctoral studies and worked with Prof. Edwin C. Kan's group with a focus on CMOS sensors. During the winter of 2011, he visited the Kavli Institute of Nanoscience at TU Delft, Netherlands and worked with Prof. Cees Dekker's group on Graphene Nanopores. In January, 2012 Krishna received an M.S degree and his PhD in May of 2014 from Cornell University's Department of Electrical and Computer Engineering.

To Amma, Appa, Ashima and Keshav

ACKNOWLEDGMENTS

This thesis would not have been possible without the help, assistance and guidance from a number of people.

First and foremost, I would like to thank my advisor Prof. Edwin C. Kan for his mentorship, expression of confidence in my abilities and constant encouragement throughout my PhD. He provided an excellent work environment, gave me the freedom to explore and his patient outlook helped ease difficult times when results seemed elusive. I am indebted to him for his support and instilling in me the confidence to march down the academic path.

I thank my committee members Prof. Manfred Lindau and Prof. Alyosha Molnar for their support, ideas and encouragement. I am especially grateful to Prof. Lindau for his help and guidance throughout my PhD, from providing me chromaffin cells , to dissecting my results piece by piece , teaching me the art of being a good scientist and inculcate in me the ability to ask the right questions. I am also thankful to Prof. David Holowka and Prof. Barbara Baird for their invaluable advice, infusing in me the attention to detail and their constant feedback on my work which helped shape my research tremendously. I thank Amit Singhai, from the Baird-Holowka group who apart from being a wonderful friend was an excellent collaborator, put up with my crazy schedules and incessant sample requests. My work on cell-transistor coupling would not have been possible without his assistance.

A large part of my work on DNA-transistor coupling was inspired through a discussion with Prof. Lois Pollack in 2008. I thank her for the immense guidance and support she has provided me over the years. I also thank Kshitij Auluck for working with me on interface modeling. The discussions we had helped shape my research tremendously. I also express my deepest gratitude to Prof. Dan Luo and Mark

Hartman for their collaboration and guiding me in my research on spectroscopy based pathogen detection. I thank Prof. Cees Dekker (TU Delft) for giving me the opportunity to visit TU Delft, and for guiding my research on graphene nanopores with Gregory Schneider. The visit was extremely educational and one that I will cherish lifelong. I thank Qinghua Fang and Annita Nagtchou of Prof. Lindau's group for help with chromaffin cells and media preparation. I thank Prof. Sunil Bhave and his group for the generous loan of their Lock in Amplifier whenever I required it. I also sincerely thank all my previous advisors Prof. Kinnatingal Sundareswaran (NIT), Prof. Navakanta Bhat (IISc) and Prof. Roberto Guerrieri (UniBo) for their support and encouragement over the years. I also express my deepest gratitude to my grand uncle Prof. Srinivasa Ranganathan (IISc Bangalore) for his immense guidance during the early stages of my education.

A hearty high-five to all members of the Kan group, both past and present who made working in lab extremely enjoyable - Keith Lyon, Alex Hou, Jonathan Shaw, Jaegoo Lee, Hassan Raza, Xiaoyang Li, Fan Yu, Nini Munoz, Shantanu Rajwade, Kshitij Auluck, Adrian Tung, Yingqiu Cao, Yun Fei, Joshua Phelps, Phillip Gordon, Sarah Xu and Yinglei Wang. A special thanks to Shantanu Rajwade, with whom I shared an office for 5 years and had amazing discussions on a wide range of topics. I also thank him for his support and assistance whenever I required it. Working in lab would have been dull if it weren't for our friendship. Thanks to my REU's Mary Funke, Sharlin Anwar and Sergio Rodriguez who worked tirelessly with me over the summers keeping up with my weird working hours. Thank to Paul Swirhun, my first undergraduate hire for his exceptional Matlab skills. Thanks to Teressa Porri for teaching me the basics of cell culture, surface preparation and fluorescence microscopy. I also thank Noah Clay and CNF staff members for assistance during the REU program.

A big cheer to my ECE friends - Mustansir Mukadam, Shantanu Rajwade, Suresh Sridaran, Adarsh Kowdle , Siddharth Tallur, Shriram Shivaramakrishnan, Tanay Gosavi and Ajay Bhat, for the endless Mattin's coffee sessions we had, which made every working day all the more enjoyable. Thanks to Ved Gund, Sachin Nadig, Po Cheng Chen, Matthew Storey, and Jonathan Puder for the amazing table tennis sessions and the workout that I badly needed. Thanks to Ben Johnson (Molnar group), for discussions on MEA's and cell recording. A high five to all my friends in Ithaca and the members of the Cornell India Association (both past and present), remembering the good times we had.

Family has been an integral part of my life and has contributed in plenty to my success in completing this PhD. I thank my parents, who believed in me, worked tirelessly to educate me, never doubted my capabilities and always lent a helping hand whenever I felt down. Thank you, Amma and Appa for all your love, support and kindness. In the end it all worked out!! I thank my brother, Keshav for his affection, wishes and encouragement. I also thank my in-laws for their support and wishes. I fondly remember the affection and care my grandparents, periamma, periappa, mama's and mami's gave me during my undergraduate years which has helped shape the person I am today. Thanks to my aunt Bamini, in NJ who has been of great help whenever I have required it.

Finally, and most importantly, I want to dedicate the last few years of all the hard work that has gone into this dissertation to my wife Ashima, who I am extremely lucky to have met at Cornell. She has been a pillar of strength, and a shoulder to cry on through all my phases of frustration. This thesis would not have been completed without her incredible and unconditional love and support.

TABLE OF CONTENTS

LIST OF FIGURES

during the transient recordings. At $pH_B = 7$ the current levels flip when E_{SG_OX} is switched from positive to negative since ψ_O is positive at the positive E_{OX} and negative at negative E_{OX}. At $pH_B = 3$, ψ_O is net positive and increases with decreasing n_O. In all three cases, the drain current is higher between 230 – 285 seconds than the initial state between 0 and 60 seconds. This is attributed to net positive charge due to field-induced protonation which remains after the negative gating pulse is relaxed. This is similar to the observed hysteresis in Fig. 3. The regions between the dotted lines in (d-f) represent the fields during readout. Solid arrows in (d-f) represent the direction of increasing n_O. 35

Figure 5. (a) ΔV_{th} (Representative of ψ_O) as a function of pH_B for varying n_O. The slope of the pH_B response reduces in the range between $pK's$ while it increases at extreme pH_B values. Cations are presumed to contribute to the slight increase in ψ_O at high pH_B. Arrow indicates increasing order of n_O (b) Theoretical fit to the experimental pH_B response reveals ΔpK of 5 for a given surface site density of $10^{17} m^{-2}$. ψ_O vs. pH_B for varying E_{OX} with (c) $pK_a < pK_b$ and (d) $pK_a > pK_b$. Both responses indicate a shift in pH_{PZC} (star) towards higher pH_B as E_{OX} is increased while the pH insensitive region shifts towards higher pH_B (c) and lower pH_B (d), with increasing E_{OX} respectively. This is primarily due to the different ionization states of the surface dependent on the choice of pK_a and pK_b. (e) Experimentally extracted pH_B response as a function of positive E_{OX} in the SG oxide, achieved by $+Q_{FG}$.

LIST OF TABLES

CHAPTER-1: INTRODUCTION

The ability to rapidly detect and characterize bio-molecules finds tremendous application in the fields of biophysics, biochemistry and personalized medicine [1-3]. Conventional procedures often employ the use of optics which requires the use of molecular labeling [3]. While labeling has proven to be extremely useful it can often interfere with basic molecular function and preclude real time detection unless pre-treated[4]. Moreover when dealing with low analyte concentrations, conventional optical readout suffers from low signal to noise ratios[5]. On the other hand nano-electronics and integrated circuit (IC) enabled platforms based on planar[6, 7], nanowire[8, 9] , nanotube[5, 10] transistors with associated signal conditioning circuitry offer[11, 12] high sensitivity, improved SNR, multiplexing, high temporal resolution and re-usability at low overall costs. This would additionally allow for high-throughput analysis and cost-effective disposable chips. In this thesis we investigate the use of CMOS (complementary metal oxide semiconductor) compatible bio-transistors with a focus on molecular and cellular bio-sensing and associated interface phenomena. A literature review is generally in order to put the dissertation work in perspective of contemporary science and technology. In this thesis, a concise state-of-the-art and motivation has been described in the introduction of individual chapters. Additionally the thesis of Blake Jacquot [13] provides a good introduction to the field of FET based sensing in general.

Briefly, the basic transistor based biosensor is based on a concept termed the ISFET (ion sensitive field effect transistor) , invented by Piet Bergveld in the 1970's[6]. The ISFET is simply a MOSFET with the metal gate replaced by a solution reference electrode (Ag/AgCl) which then maintains the overall electrochemical potential. Surface hydroxyl groups on the exposed gate dielectric (normally SiO2) when in contact with the electrolyte are sensitive to protons. When protons bind, the surface charge and hence surface potential change and it is this physical aspect that gives rise to the ISFET's use a pH sensor. Alternatively the oxide-electrolyte interface can be functionalized with a self-assembled monolayer (SAM) or specific surface coating which then allows for specific molecular binding and recognition. Molecules that are charged (i.e. also depending on electrolyte composition) shift the surface potential upon adsorption which subsequently via the field effect modulates the drain current in the channel. Most ISFET's studies however use custom in-house fabrication [7, 8, 14] to realize devices with the gate oxide directly exposed to the electrolyte of interest. Due to the proximity of the electrolyte to the channel (i.e. the gate oxide barrier) such schemes often suffer from current drift due to slow ion penetration[13] into the oxide degrading the stability of recording. Also the reference electrode stability and overall interface quality plays an important role in determining overall sensitivity[15] as conventionally there is no other independent handle available to control the channel potential. A good reference electrode is required to maintain a stable electrochemical potential under varying pH and ionic conditions. Tiny voltage offsets at the reference electrode interface can induce ~mV shifts in surface potential which can drastically influence the quality of sensing[16].

Another area of intense study in the field of integrated biochips is the ability to control and manipulate biomolecules and cells Controlled manipulation of matter is advantageous in a variety of disciplines ranging from engineering to basic biophysics. A stark example is the field effect control of electrons in a transistor channel. In the same token, manipulation of ions and molecules in fluids are also sought through the application of electric fields. It would be extremely beneficial if transistor based sensors capable of charge sensing were also inherently capable of charge manipulation. However the basic ISFET structure would not suffice for such dual operation modalities. So we ask ourselves (a) is it possible to improve current ISFET technology by incorporating mechanisms that improve stability, reduce drift, reduce the burden on reference electrode quality, incorporate actuation and (b) can such device be realized in foundry CMOS?

The transistor under study in this thesis, termed the chemoreceptive neuron MOS (CνMOS) is inspired by the original neuron MOS concept developed by Shibata and Ohmi [17]. The CνMOS features extended sensing and control gates coupled to a common floating gate. The control gate is used as an independent handle to tune the operating point, provide bias offsets when required, reduce the burden on reference electrode biasing and influence the conditions for tunneling. The electrolyte is biased using a reference electrode which in addition to a DC bias can also provide an AC small signal when working in impedance mode. The floating-gate is capable of storing discrete charge of either polarity which gives rise to the concept of programmability (Chapter 2 and 3).

The CνMOS structure was first proposed by Nick Shen [18] for chemical sensing and electro-wetting applications and later investigated for protein binding and ionic sensing by

Blake Jacquot[13]. This thesis in addition to previous efforts introduces the ability to control and detect ions and biomolecules using the CvMOS, focuses on coupling excitable and non-excitable cells to the extended sensing gate and outlines a theory for the sensing gate electrolyte interface under the influence of applied electric fields and in the presence of biomolecules. This thesis is organized as follows;

(Chapter 2) outlines interface theory, surface modeling, device operation under different terminal conditions (for ex: reference electrode floating vs. pinned), principles of the tunneling mechanism, transient and quasi-static measurements of gating effects and the ability to tune the surface pH using stored non-volatile charge.

Chapter-3 describes simultaneous sensing and manipulation of adsorbed DNA using static charge injection, sheds light on the influence of applied electric fields on signal sensitivity and outlines a theory for signal generation including permittivity effects.

Chapter-4 describes the influence various factors such as SAM's, pH, electric field, ionic concentration, multivalent ions, have on signal generation when dealing with DNA biosensing.

Chapter-5 introduces the concept of split signal delivery for impedimetric detection of biomolecules. DNA nanostructures are introduced as amplifying agents to improve the limit of target detection to ~100fM.

Chapter-6 describes the coupling of excitable chromaffin and non-excitable RBL-2H3 mast cells to the CvMOS. Action potential activity is measured from chromaffin cells in addition to catecholamine release. RBL-2H3 degranulation response is also measured. Simultaneous charge and impedance is measured using the split signal delivery approach.

REFERENCES

[1] M. R. Hartman *et al.*, Nanoscale **5**, 10141 (2013).

[2] P. Yager, G. J. Domingo, and J. Gerdes, Annu. Rev. Biomed. Eng. **10**, 107 (2008).

[3] J. M. Rothberg *et al.*, Nature **475**, 348 (2011).

[4] Y.-S. Sun *et al.*, Langmuir **24**, 13399 (2008).

[5] S. Sorgenfrei *et al.*, Nature nanotechnology **6**, 126 (2011).

[6] P. Bergveld, Biomedical Engineering, IEEE Transactions on **BME-19**, 342 (1972).

[7] F. Uslu *et al.*, Biosensors and Bioelectronics **19**, 1723 (2004).

[8] E. Stern *et al.*, Nature **445**, 519 (2007).

[9] F. Patolsky *et al.*, Science **313**, 1100 (2006).

[10] I. Heller *et al.*, Nano Letters **8**, 591 (2008).

[11] I. Hafez *et al.*, Proceedings of the National Academy of Sciences of the United States of America **102**, 13879 (2005).

[12] B. Eversmann *et al.*, Solid-State Circuits, IEEE Journal of **38**, 2306 (2003).

[13] B. C. Jacquot, *CMOS-compatible charge sensing technology based on non-volatile memory* (Cornell University, Aug., 2007).

[14] G. Zeck, and P. Fromherz, Proceedings of the National Academy of Sciences **98**, 10457 (2001).

[15] E. D. Minot *et al.*, Applied Physics Letters **91**, 093507 (2007).

[16] L. Larrimore *et al.*, Nano Letters **6**, 1329 (2006).

[17] T. Shibata, and T. Ohmi, Electron Devices, IEEE Transactions on **39**, 1444 (1992).

[18] Y.-M. Shen, *Charge-based sensors and actuators with silicon integration* (Cornell University, Jan., 2004).

CHAPTER 2- PROGRAMMABLE ION SENSITIVE TRANSISTOR INTERFACES: ELECTROCHEMICAL GATING

CHAPTER OVERVIEW

Electrochemical gating is the process in which an electric field normal to the insulator electrolyte interface shifts the surface chemical equilibrium and further affects the charge in solution [Z. Jiang, and D. Stein, Langmuir 26, (2010)]. The surface chemical reactivity and double-layer charging at the interface of electrolyte-oxide-semiconductor (EOS) capacitors is first investigated. We find a strong pH-dependent hysteresis upon DC potential cycling. Varying salinity at a constant pH did not change the hysteretic window, implying that field-induced surface pH regulation is the dominant cause of hysteresis. We then propose and investigate this mechanism in foundry-made floating-gate ion-sensitive field-effect transistors (ISFET's), which can serve both as an ionic sensor and actuator. Termed as the chemoreceptive neuron MOS transistor (C*v*MOS), it features independently-driven control (CG) and sensing gates (SG) that are capacitively coupled to an extended floating gate (FG). The SG is exposed to fluid, CG is independently driven and the FG is capable of storing charge (Q_{FG}) of either polarity. Asymmetric capacitive coupling between the CG/SG to FG results in intrinsic amplification of the measured surface potential shifts, and

influences the FG charge injection mechanism. This modified SG surface condition was monitored through transient recordings of the output current, performed under alternate positive and negative CG pulses. Transient recordings revealed a hysteresis where the current was enhanced under negative pulsing and reduced after positive pulsing. This hysteresis effect is similar to that observed with EOS capacitors suggesting a field dependent surface charge regulation mechanism at play. At high CG biases, non-volatile charge (Q_{FG}) tunneling into the FG occurs, which creates a larger field and tunes the pH response and the point of zero charge. This mechanism gives rise to *surface programmability*. In chapter I, we describe the operational principles, tunneling mechanism, and the role of electrolyte composition under field modulation. The experimental findings are then modeled by a Poisson Boltzmann (PB) formulation with surface pH regulation. We find that surface ionization constants play a dominant role in determining the pH tuning effect. In chapter II, we extend the dual-gate operation to molecular sensing, and demonstrate the use of Q_{FG} to achieve manipulation of surface-adsorbed DNA.

INTRODUCTION

Transistor-based biological/chemical transducers have gained considerable attention over the last decade [1-3]. The Ion Sensitive Field Effect Transistor (ISFET) [2] has its gate oxide directly exposed to the electrolyte with its electrochemical potential set by a solution reference electrode. The oxide interface possesses a net surface charge due to hydroxyl groups upon exposure to the electrolyte. The charge density and the electrostatic potential then decay from the interface into the solution bulk over the characteristic distance of the Debye length. A change in the oxide-electrolyte interface potential due to ionic adsorption or reference-electrode biasing then induces a shift in the channel current via a change in the electric field in the gate oxide. The change in the reference electrode potential with respect to the transistor source bias to achieve a constant channel current (i.e. a constant field in the gate oxide) is thus a direct measure of the oxide-electrolyte interface potential shift [4]. The transistor is typically only sensitive to ionic and molecular charges within a few Debye lengths from the interface. While numerous examples of FET-based ionic and molecular sensors have been demonstrated [3, 5-7], the ability to dissect the complex interplay between pH, salinity and surface chemistry is still unclear. In addition, the ability to impart electrical control over the sensing interface concomitantly is still elusive. Dynamic control of surface charge can potentially realize reversible interfaces [8], addressable sensor pixels in large-scale arrays, controlled charge modulation [9], and even local pH titration [10] with simultaneous detection. However, since ISFET generally has an exposed dielectric interface which consists of amphoteric surface groups, a change in

electric field within the oxide would not only modulate ions in solution but also affect the chemical composition of the interface.

Similarly, when an electrode covered by an insulator is biased in an electrolytic medium, the field in the insulator would thereby modulate the ionic double layer [9]. The applied potential to such an electrode or static stored charge on a buried floating electrode can in turn influence the insulator's surface charge according to its amphoteric nature, which then affects the proton binding affinity, the adsorption equilibrium and the net charge in the double layer. The interplay between the applied field and the chemical equilibrium at the interface is termed as "electrochemical gating" [9]. The first examples of electrochemical gating in microfluidic systems by Ghowsi et al. [11] and Schassfoort et al. [12] demonstrated that local fields could modulate the electroosmotic flow in micro-channels, but did not elaborate on the chemical properties of the interface. Karnik et al. [13], Fan et al. [14] and Guan et al. [15] demonstrated field-effect control within fluidic channels, which leads to ionic modulation and subsequent protein transport. Fan and coworkers [14] further highlighted that chemical functionalization strongly affected the ionic polarity within the channel. Several recent examples, including three-terminal control within a fluidic network [16] and electrically gated nanopores [17-21], show similarities to gate modulation of the channel carriers in MOSFET, which can be viewed as fluidic analogues of electronic transistors. Jiang et al. [9, 21] highlighted the effect of surface chemistry on ionic regulation in the electrolyte at an electrically gated dielectric interface. They found that surface charge density and hence protonation and deprotonation impose limits on the nonlinear charging property of the double layer.

The pH at the interface was observed to be field-dependent, which further affected ion modulation. This is specifically important in manipulating molecules by Coulombic forces with careful consideration of the hydration and ionic screening effects. Recently McKinnon and colleagues [22] theoretically showed that changing the field in the gate oxide had a profound effect on biomolecular sensitivity primarily due to ionic depletion at the interface. This implies a possible strategy to implement chemical/bio sensors with an electrically tunable interface to achieve high sensitivity and specificity.

In order to develop an intuitive understanding of our approach, we first consider a conventional electrolyte-oxide-semiconductor (EOS) [Fig. 1(a), Appendix-A Fig. 31(a)] system, where electrochemical gating modulates the surface charge. AC measurements using capacitive electrode structures are frequently employed to measure the net charge modulation in the electrolyte. However, measuring capacitances on the order of pF to aF in many lab-on-chip (LOC) systems often requires complex circuitry and a long averaging time, and is thus prone to noise. It is much easier to measure charge via transistors at such scales, as the output current can be sampled more easily. If one intentionally introduces a highly conductive slab as a floating gate (FG) [Appendix A, Fig. 31(b)] in between the reference electrode and oxide-electrolyte interface, the charge modulation in the electrolyte now depends on the electric field between the FG and electrolyte bulk. The FG potential is determined by the weighted inputs of all capacitors coupled to the FG and additionally the nonvolatile charge it stores. The change in surface charge or ionic charge in the double layer will thus affect the FG potential. The question remains as whether one can

measure the FG potential directly to estimate the electrolyte charge. By coupling a transistor capacitively to the FG, the current output is an accurate measure of the FG potential. This transistor concept is termed as the chemoreceptive neuron MOS transistor (CvMOS) [23] [Fig. 1(b), Appendix-A, Fig. 31(c)].

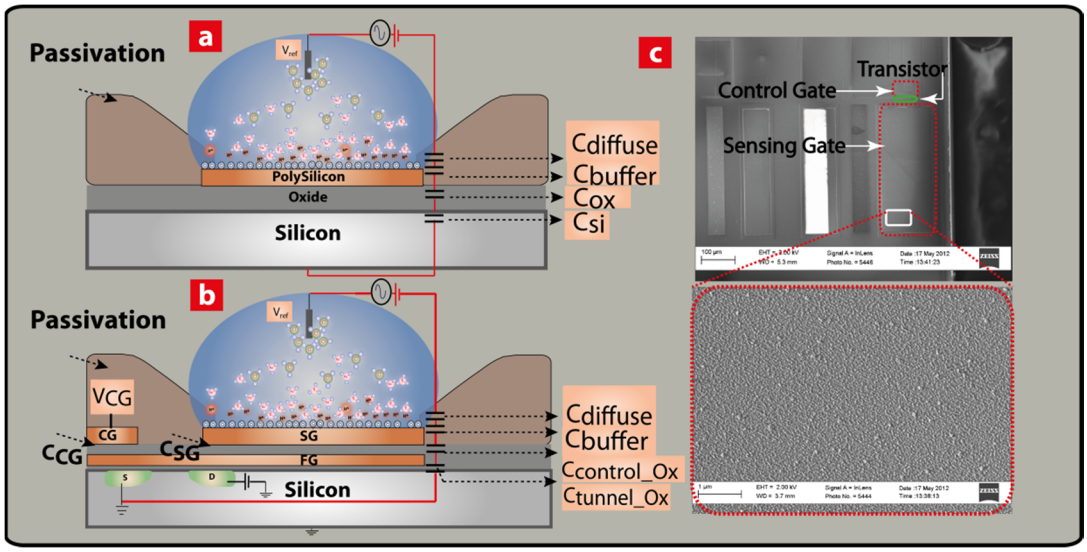

Figure 1: (a) The EOS capacitor used in the CV analysis. (b) The CvMOS transistor with two independently driven gates: (control) CG and (sensing) SG coupled to a common (floating gate) FG. The FG to electrolyte capacitive coupling is mimicked by the EOS structure. The CG is shielded from the solution via a thick oxide (2µm) passivation. (c) An SEM image of the fabricated transistors showing the SG, CG and transistor regions, respectively.

The CvMOS [23] [Fig. 1(b)] is a multi-gate transistor with control (CG) and sensing gates (SG) coupled to FG. The CG alleviates the sole reliance on biasing from the reference electrode V_{REF}, which is important from a reliability and pixel-level biasing perspective. The reference electrode (Ag/AgCl) can still be used to pin the electrolyte bulk. This scheme has multiple advantages: (i) suitable fluid biasing can lower the read voltage from the control gate and enlarge the sensing range, (ii) the pinned electrolyte potential results in fast ion settling time, and (iii) the CG can be used in feedback to maintain the optimal signal-to-noise ratio (SNR) condition without

changing the reference electrode bias. Due to the possible asymmetric capacitances between the two gates, the voltage measured from the CG to maintain the same channel current can be intrinsically amplified if $C_{CG} < C_{SG}$. At high CG biases, Fowler-Nordheim (FN) tunneling ensues to inject nonvolatile charge onto the FG, which can in turn render a strong field in the SG oxide even after the CG bias is removed. We experimentally investigate the role of electrolyte composition on the transistor characteristic both with and without FG charges and corroborate our measurements against standard (EOS) capacitors with similar chemically reactive interfaces.

METHODS

A. Materials

EOS capacitors [Fig. 1(a)] were fabricated on p-type silicon wafers after standard MOS cleaning. About 20nm of thermal SiO_2 was grown, followed by 30nm growth and patterning of LPCVD polysilicon with n^+ doping. Atomic-layer deposition (ALD) of nitride as a protective coating was then deposited and patterned to expose only the polysilicon gate to solution. The CvMOS transistors were fabricated in a $1.5\mu m$ AMI foundry process as described previously [23]. Briefly, the tunnel oxide refers to the oxide between the channel and the FG, while the control oxides represent the oxide between the CG/SG and FG. The FG is electrically floating and does not have any direct conducting path to the electrolyte or other electrodes. The reference electrode pins the electrolyte bulk to (V_{REF}) while the CG can be pulsed to program or erase the

device. The tunnel and control oxide thicknesses are 10nm and 35nm, respectively. The control gate area is $25\mu m \times 40\mu m$ while sensing gates vary between $5\mu m \times 400\mu m$ and $200\mu m \times 400\mu m$. An SEM image of the fabricated chip is shown in Fig. 1(c). The chip was cleaned with DI water and isopropyl-alcohol (IPA) before each test. A small reservoir made of epoxy was created to isolate the fluid from the bond pads.

Electrolytes containing $NaCl, MgCl_2$ and $Co(NH_3)_6Cl_3$ salts (Sigma Aldrich) were made up to the desired dilution using Millipore de-ionized H_2O. The pH of the solutions was regulated using conjugate acid-base mixtures. TE buffer (10mM TRIS pH 8, 10mM NaCl and 1mM EDTA) was added to test for buffering effects. Electrodes made of $Ag/AgCl$ were used as reference electrodes. Experiments were performed in a light-tight environment.

B. Electrical instrumentation

Capacitance-voltage (CV) measurements were performed using a Keithley 4200 semiconductor parameter analyzer. CV profiles were recorded at various small-signal frequencies. The reference electrode was supplied with an AC signal superimposed on a slow DC sweep, while the wafer chuck was used as ground. The transistor transfer characteristics (the drain current I_D vs. the CG bias (V_{CG})) were recorded using a Keithley 236 source measure unit (SMU) for the drain ($V_D = 1V$) and a Keithley 2400 was used to sweep V_{CG}. Programming was carried out by applying a large positive voltage to V_{CG} with a +1V bias on V_D unless otherwise specified, while erasing was by a large-magnitude negative voltage. The transient measurements at constant V_{CG} were

recorded by the trans-impedance amplifier (TIA, Stanford Research Systems SR570, CA, USA) with a sensitivity of $100\frac{\mu A}{V}$ and low-pass filtering at 3KHz. The data was collected on a computer through a data acquisition test board (NI BNC 2110 and NI USB 6259). The bias on the TIA was set to 1V. Prior to measurements, the transconductance (g_m) seen from both the CG and SG was recorded in order to calibrate the capacitance ratio.

DEVICE OPERATION AND SENSING PRINCIPLES

A. Capacitive amplification

The CvMOS sensor works on the principle of the conventional neuron MOS transistor [23, 24] where two input gates are coupled to a common FG. The potential on the FG (V_{FG}) can be calculated by the capacitive divider model shown in Fig. 32 (Appendix A). Additonally, a net charge Q can be stored on FG via tunneling. The constant current readout implies that V_{FG} is brought back to the same point. This can be achieved via V_{CG} or V_{REF}. The capacitance ratio between the SG and CG to the FG ($\frac{C_{SG}}{C_{CG}}$)sets the scaling factor. Thus an asymmetric CvMOS structure can lead to a magnification of the threshold voltage shift (Eq. 1) as observed from the control gate when the sensing gate experiences a load from the electrolyte.

$$\Delta V_{th\_CG} = \frac{C_{SG}}{C_{CG}} \cdot (\Delta \psi_O) \qquad (1)$$

The governing equations are listed in Table 3 (see Appendix A). Recent reports [6, 25]

have proposed similar concepts and claimed to have beaten the Nernst sensitivity limit of 59mV/pH. We reitierate that this technique merely scales the surface potential shift and does not signify any change in the intrinsic properties [5, 26] of the electrolyte interface. The amplification method does however reduce the burden on supporting circuitry to sense the voltage shift [26]. Theoretically, the capacitive amplification factors should have achieved values between 70~90 for the layouts used in this study. However, due to parasitics we experimentally observed factors of 10~30 [Appendix A, Fig. 36(a)].

B. Programming and erase operations

In conventional Flash memory devices when the CG bias is swept to a large magnitude, sufficient electric field can develop across the gate stack enabling electron/hole tunneling from the silicon channel onto the FG (Q_{FG}). "Programming" is the condition when the FG has a net stored charge state, while "erase" is the condition under which that charge is removed (Appendix A, Fig. 33). The field in the oxide during tunneling is quite high ($0.8 \sim 1\frac{V}{nm}$) which is a pre-requisite for Fowler-Nordheim (FN) tunneling. Such fields are quite common in Flash memory devices [27] and can be employed many times without permanent breakdown [28]. The CvMOS has an EOT (effective oxide thickness) of approximately 50nm and the maximum CG bias for programming does not exceed 40V.

The CG is shielded from the solution by a large passivation oxide ($> 2\mu m$) and hence the CG bias has no direct influence on the electrolyte except through the FG and SG

coupling. The SG surface is highly-doped polysilicon which is widely being considered for biosensing applications [3, 29, 30]. At high V_{CG}, the electric field in the CG control oxide (E_{CG_OX}) increases. Normally V_{FG} would rise together with V_{CG}. However the FG is coupled to V_{REF} through the large SG which ensures that V_{FG} does not increase much with an increase in V_{CG}. This directly affects E_{CG_OX} as it rises considerably higher than the field in the tunnel oxide (E_{TOX}).

For example, given a capacitvie ratio of 20, a 40V CG bias induces only a ~2V rise in V_{FG}. Evidently this would cause a larger change in E_{CG_OX} than in E_{TOX}. Electrons thus tunnel out of the FG onto the CG faster than they tunnel onto the FG from the channel. This causes a net positive stored charge on the FG and lowers the threshold voltage V_{th}. However, if V_{CG} is large and negative, the opposite occurs resulting in net electron storage. The energy band diagrams depicting this operation are shown in (Appendix A, Fig. 33).

If the reference electrode is left floating, the capacitive coupling in the SG branch is much weaker and V_{FG} is then allowed to track V_{CG}. The E-field in this case aids electron injection from the channel into the FG during programming and hole storage during erase [Appendix A, Fig.S3 (c&e)], similar to conventional Flash memory operation.

Thus by flipping the reference electrode between floating and biasing conditions during the programming process, the polarity of stored charge on the floating node can be significantly changed. This nonvolatile charge then capacitively interacts with the

fluid via the field effect. A simulation of the tunneling effect with and without the reference electrode is shown in Fig. 36(b) (see Appendix A). Electrostatics of the system is represented by the capacitors C_{DL} (double layer), C_{SG} (sensing gate), C_{CG} (control gate) and C_{tunnel} (tunnel oxide), respectively. This network is solved self-consistently with a Tsu-Esaki tunneling formulation [31] which is represented by voltage-controlled current sources.

The SG-fluid interface is considered to be in steady state during the program pulse and V_{th} measurement ramp. Dynamic processes of ion or water dipole rearrangement are assumed to occur at time scales much faster than tunneling. The double layer capacitance (C_{DL}) is modeled based on a Poisson-Boltzmann formulation including ion Steric effects [32].

C. Role of surface groups and electrochemical gating

The ISFET or EOS response is generally dictated by the protonation behavior of the interfacial inorganic oxide in direct contact with the electrolyte. Surface hydroxyl groups are amphoteric in nature, protonated or deprotonated depending on the solution bulk pH (pH_B), resulting in a net surface charge σ_O. It is this shift in charge that determines the net pH_B sensitivity of the underlying transistor. Jiang and Stein [9] theoretically proved that in addition to pH_B, the field in the underlying oxide profoundly affected σ_O, which further influenced the surface pH sensitivity (pH_S). We adopt a hydroxyl surface group model [9, 33]where the basic acid-base equilibrium at the interface is given by Eq. (2).

$$A-OH \overset{K_a}{\Leftrightarrow} A-O^- + H_B^+ \qquad (2)$$

$$A-OH + H_B^+ \overset{K_b}{\Leftrightarrow} A-OH_2^+$$

Here K_a and K_b are the dissociation constants and H_B^+ is the bulk proton concentration. At a particular pH_B, the interface is charge neutral. This is termed as pH_{PZC}, i.e., the pH at the point of zero surface charge. However, when pH_B is not equal to pH_{PZC}, the surface pH (pH_S) shifts in response to the change in pH_B. The number of surface groups that ionize in response to varying pH_S is termed as the buffer capacity (β_S) and its associated capacitance [4] is termed as C_{Buffer}. By definition, β_S is the ratio of the change in net surface charge to that in pH_S.

$$\beta_S = \frac{d[\sigma_O]}{dpH_S} \qquad (3)$$

Here σ_O is equal to the net number of titrated groups per area:

$$\sigma_O = -e \cdot \Gamma^{O-} + e \cdot \Gamma^{OH_2^+} \qquad (4)$$

where $N_S = \Gamma^O = \Gamma^{O-} + \Gamma^{OH_2^+} + \Gamma^{OH}$ is the total number density of ionizable surface groups and is a constant for a given surface depending on the chemical composition and surface functionalization. Using the relationship between $K_a = \frac{H_S^+ \cdot \Gamma^{O-}}{\Gamma^{OH}}$, $K_b = \frac{H_S^+ \cdot \Gamma^{OH}}{\Gamma^{OH_2^+}}$ and Γ^O, and under the assumption of a single pK model (i.e. $pK_a = -\log_{10}(K_a)$), i.e., when only one type of surface group of O^- is considered, Eq.

(4) can be rewritten as,

$$\sigma_O = \frac{-e \cdot \Gamma^O}{1 + \frac{H_S^+}{K_a}} \tag{5}$$

If we consider both surface ionization reactions i.e., a 2pK site-binding model, Eq. (4) then becomes

$$\sigma_O = e \cdot \Gamma^{OH} \cdot \left(\frac{H_S^+}{K_b} - \frac{K_a}{H_S^+} \right) \tag{6}$$

We can then solve for Γ^{OH} by using the relationship between K_a, K_b and Γ^O.

Here the surface proton activity H_S^+ is related to the bulk proton activity H_B^+ by the Boltzmann relation

$$H_S^+ = H_B^+ \cdot \exp\left(- \frac{e(\psi_O - V_{REF})}{kT} \right) \tag{7}$$

The simulation considers a metal electrode below an insulator exposed to the electrolyte (Metal-oxide-electrolyte) [Fig. 1(a)] similar to the model structure considered by Jiang and Stein [9]. The electrolyte bulk potential (V_{REF}) is held at ground. On applying a potential sweep to the metallic electrode with respect to V_{REF}, two compensating charges at the electrolyte-oxide interface will respond: 1) protonation/deprotonation of the surface hydroxyl groups, denoted by σ_O, and 2) the double layer charge, σ_{DL} (see next section). The field in the oxide is then given by

$$E_{OX} = \frac{-[\sigma_O + \sigma_{DL}]}{\varepsilon_{OX}} \tag{8}$$

Equation (8) is then solved self consistently for the entire electrostatic system.

D. Electrical double layer charge (σ_{DL})

The SG-electrolyte interface is commonly described by the Gouy-Chapman-Stern (GCS) model which considers ions as point charges. When a solid interface is exposed to electrolyte, ionization or ion adsorption creates a net surface charge density σ_O. This results in a strong attraction of counterions towards the interface to neutralize the immobile surface charge denoted by σ_{DL}. Co-ions on the contrary are repelled away from the wall. The capacitance at the wall is generally described by a Stern capacitance C_{Stern} from the inner immobile or specifically adsorbed layer and the outer diffuse layer capacitance C_{DL}. A value of 18 $\frac{\mu F}{cm^2}$ is assumed for the Stern layer capacitance (i.e. considering an approximate thickness of 5 $\mathring{A}$ and a dielectric constant of 10). The charge distribution is traditionally described by the Poisson-Boltzmann (PB) equation[32]:

$$\varepsilon \frac{\partial^2 \psi}{\partial x^2} = -2zen_O \sinh \frac{(ze\psi)}{kT} \qquad (9)$$

For a z:z electrolyte, where the mobile diffusive charge is confined to a thin capacitor with a width governed by the Debye length.

$$\lambda_D = \sqrt{\frac{\varepsilon kT}{2z^2 e^2 n_O}} \qquad (10)$$

Here z is the valency, n_O the bulk ion concentration, e the elementary charge, kT is the thermal energy and ε is the dielectric constant of the solvent. Equation (9) stems from a mean-field formulation where ions are treated as point charges, i.e., ion-ion and

ion-wall interactions are ignored. In the conventional PB formalism, charge density generally blows up due to the exponential dependence on surface potentials which is unrealistic under moderate to high ψ_O values. By accounting for close packing of ions at the interface, a limit is imposed on the maximum achievable charge density. In this work we model the NaCl system alone using the PB approximation since the effect of size was found to be negligible within the range of ψ_O obtained. However when dealing with multivalent ions the ion distribution from the interface is described using a 1:z approximation [34] including Steric effects (see Appendix A, Fig. 34). We find that Steric effects become prominent when considering large multivalent ions as layering and charge density saturation occurs for surface potentials $\sim 4-6\frac{kT}{e}$ (see Appendix A, Fig. 34).

Steric related phenomena are generally weak under low monovalent (NaCl) electrolyte concentrations and moderate σ_O conditions. Using the modeling framework presented in the previous section ion size effects were only marginally observed at E-fields above $\sim 0.5\frac{V}{nm}$ (not shown) with NaCl salts. We do however point out that in a recent theoretical study, Gillespie et al. [35] showed that with surface charge densities approaching $\sim 0.2\frac{C}{m^2}$ (which is typical of pristine dielectric interfaces) significant ion layering was observed even at low saline concentrations. It is thus paramount to understand the interfacial charge conditions as ion size effects can preclude a proper assessment of the observed signals with sensitive field effect devices. To accurately

model ionic layering especially with multivalent salts, we invoke the modified Poisson-Boltzmann (MPB) theory [32, 36] [see Eq. (11)] which includes the hard-sphere Steric effect between ions owing to their finite size but ignores correlations. A Stern layer capacitance is not assumed in the MPB formulation.

$$\varepsilon\nabla^2\psi = -2zen_\infty \frac{\sinh\left(\frac{ze\psi}{k_B t}\right)}{1+2\nu\sinh^2\left(\frac{ze\psi}{2k_B T}\right)} \tag{11}$$

where $\nu = 2a^3 n_O$ is the volume packing factor of ions and a is the size of the ion. The packing factor sets a limit on the maximum achievable charge density at the interface. The charge within the double layer is then given by

$$q_{MPB} = \sigma_{DL} = -\mathrm{sgn}(\psi_{DL})2zen_O\lambda_D\sqrt{\frac{2}{\nu}\ln\left(1+2\nu\sinh^2\left(\frac{ze\psi_{DL}}{2kT}\right)\right)} \tag{12}$$

The electric field originating from the potential across the solid/electrolyte interface ($\psi_O \geq \frac{kT}{e}$) attracts counterions to the surface forming an initial screening layer. If the surface potential rises further ($\sim 5\frac{kT}{e}$), the electric field strength becomes high enough to cause layering of counterions against the solid interface (Appendix A, Fig. 34), leading to an effective increase in the double layer thickness, which extends further into the electrolyte bulk. From the capacitive point of view if one were to assume an additional Stern layer, C_{Stern} could help relieve the excess condensation of ions, but would not be able to withstand a large voltage drop $\sim 5-10\frac{kT}{e}$ due to the

Steric constraint. Under such field conditions, the region of ion accumulation extends away from the surface into the solution where ions do not exhibit specific interactions with the solid interface. This causes a further increase in the thickness of the double layer, leading to a decrease in the differential capacitance of the diffusive layer. As mentioned previously this effect becomes significant with large multivalent ions.

E. Multivalent ions and charge inversion

The Debye-Huckel (DH) approximation within the GCS double-layer framework states that the ionic screening effectively lowers the molecular charge in the electrolyte as observed from a finite distance. This is the net charge looking into the Gaussian sphere around the molecule [37] including its screening counter-ion cloud. In comparison with monovalent ions, multivalent ions are known to form a strongly correlated interface with charged moieties which overcharge the interface [38-43]. This can lead to excess counterion condensation and eventually polarity reversal, which cannot be explained by the conventional mean-field theory [32]. This counter-intuitive phenomenon is termed as charge inversion (CI) [38]. Shklovskii [38] postulated that this effect arose primarily due to strong lateral ion-ion interactions which got stronger as the valency increased, and a much larger negative electrochemical potential is developed within the 2D ionic layer. Ion-Ion correlations give rise to counterion layering against the interface, which can lead to overcharging under suitable field conditions. This is often much easier to achieve with multivalent ions [39] since the interaction energy between an ion and its background charge is directly proportional to $z^{3/2}$. Co-ions are then attracted to the interface to neutralize

this excess counterion charge, which is the main reason for surface potential reversal. This effect can also lead to oscillations in the surface potential [38, 44]. Storey et al. [44] commented that in addition to Steric considerations, such correlation effects can affect the C_{DL}. In this work we do not model the effect of charge inversion but present experimental evidence in support of such a mechanism.

RESULTS AND DISCUSSION

A. Nernstian vs. non-Nernstian surface

Before we describe the electrochemical gating response, we first highlight the difference between a Non-Nernstian and Nernstian surface. A Nernstian response implies that ψ_O vs. pH_B response is linear and has a slope of $\sim 59mV / pH_B$. We find that the surface dissociation constants and net surface site density play dominant roles in determining this slope, and can shift the response from Nernstian to non-Nernstian. The pH_B response of an ISFET is traditionally given [38,39] by

$$\frac{\partial \psi_O}{\partial pH_B} = -2.3\frac{kT}{e}\alpha \qquad (13)$$

where α is defined as;

$$\alpha = \frac{1}{1+\frac{2.3kTC_i}{e\beta_S}} \qquad (14)$$

here $C_i = \frac{C_{DL}\cdot C_{Stern}}{C_{DL}+C_{Stern}}$, and from Eq. (3);

$$\beta_S = \frac{2.3 \cdot eN_S \cdot H_S^+ \cdot (K_b H_S^{+2} + K_a K_b 4H_S^+ + K_a K_b^2)}{(K_a K_b + K_b H_S^+ + H_S^{+2})^2} \quad (15)$$

The H_S^+ at the interface at PZC is given by

$$H_S^+ = \sqrt{K_a \cdot K_b} \quad (16)$$

It is immediately clear that a pH insensitive interface (non-Nernstian) necessarily implies a small β_S. Equation (14) suggests an intricate interplay between ΔpK and pH_B. A low value of ΔpK and high N_S is desired to achieve near Nernstian response [45, 46]. However the individual contributions of K_a and K_b are not immediately clear from Eq. (15). We note that both Bousse et al. [45] and Van den Vlekkert et al. [46] simplified Eq. (6) while deriving the pH sensitivity and showed that the surface potential close to the PZC can be described by the relation;

$$2.3(pH_{PZC} - pH_B) = \frac{e\psi_O}{kT} + \sinh^{-1}(\frac{e\psi_O}{\gamma kT}) \quad (17)$$

Here pH_{PZC} is defined by $\frac{(pK_a + pK_b)}{2}$, and $\gamma = \frac{2e^2 N_S}{C_{Diff} kT} \sqrt{(\frac{K_a}{K_b})}$ is a dimensionless sensitivity parameter. In order to confirm this approximation and show that the pH sensitivity is strongly dependent on N_S and $\sqrt{\frac{K_a}{K_b}}$, without making simplifications, we first solve Eq. (13). We observe that if K_b increases (pK_b is lowered), the surface has more neutral groups and hence pH_{PZC} extends into the acidic branch of the pH_B response. Lowering K_a (pK_a is increased) ensures the same effect, extending the

PZC more towards the base branch. It is important to note that when pH_B is lower than pK_a, the surface will be mostly charge neutral and hence show a flat pH_B response. This is graphically represented in Fig. 2(a). However, when K_a increases, ΔpK decreases and the response becomes more Nernstian. This is in agreement with the simplification by Bousse et al. [45] [see Eq. (17)] and earlier reports on chemical surface modifications [47].

A smaller ΔpK creates more charged groups around the PZC, which improves the pH_B response. Lowering N_S reduces α and the slope of the pH_B response, because a reduction in the number of ionizable groups decreases the net available sites for proton binding [Fig. 2(b)]. The PZC however does not change with varying N_S.

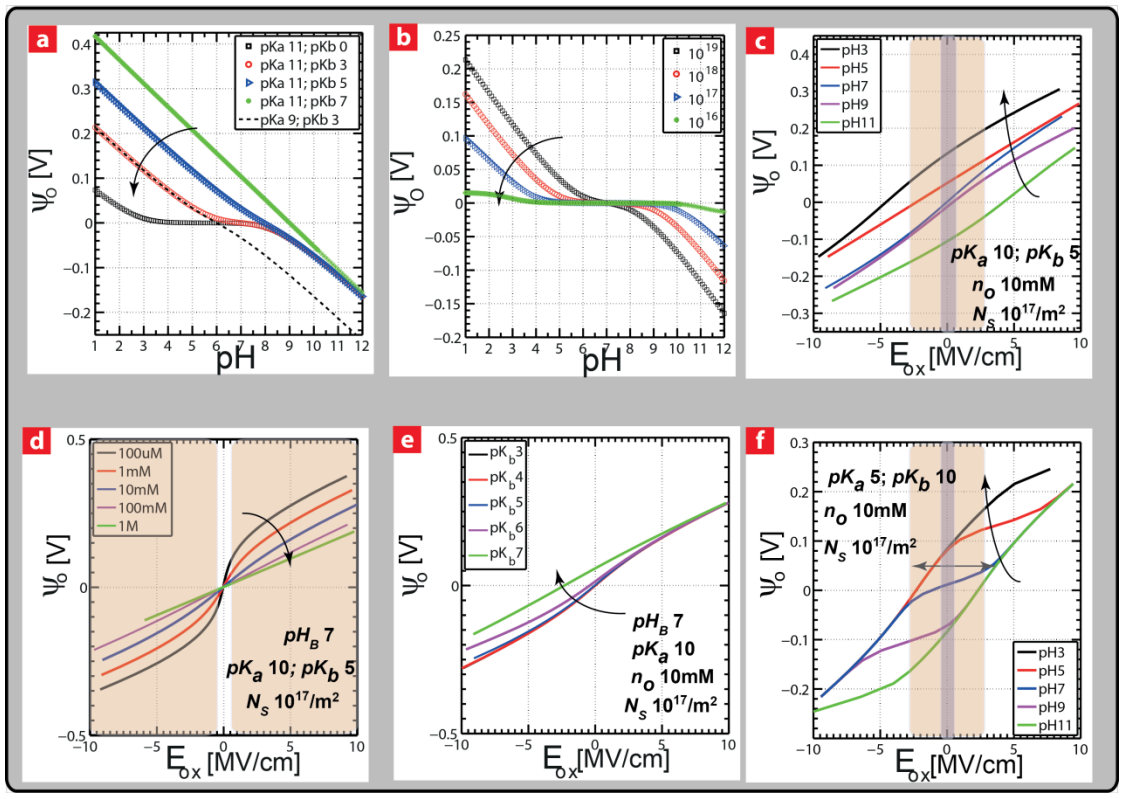

Figure 2: (a) Variation in ψ_O as a function of pH_B for variations in ΔpK . As ΔpK increases (arrow) the slope becomes more non-Nernstian (lower than 60mV/pH). (b) ψ_O vs. pH_B for variations in surface site density in m^{-2}. The relative flattening in the response increases as N_S decreases. Arrow indicates direction of N_S decrease. (c) ψ_O vs. E_{OX} for varying pH_B. Solid arrow represents direction of decreasing pH_B.When pH_B is in the range between the $2\,pK's$, the surface buffering is low with pH_{PZC} ~7. Here $pK_a = 10$ and $pK_b = 5$. The region between the dotted lines represents the E_{OX} range used in this study and the dark shaded region represents the fields applicable during readout. (d) ψ_O vs. E_{OX} for varying salinity n_O. The shaded region (grey) represents field during readout. Solid arrow represents the direction of increasing n_O. The maximum modulation in ψ_O occurs for lower n_O. At the zero E_{OX} condition, the surface sensitivity to varying n_O is negligible. An applied positive or negative E_{OX} can tune ψ_O to be sensitive to changes in n_O. (e) ψ_O vs. E_{OX} for varying pK_b. ψ_O is affected only in the $-E_{OX}$ region. Solid arrow represents the direction of increasing pK_b (f) ψ_O vs. E_{OX} for varying pH_B with pK_a and pK_b flipped. Solid arrow represents the direction of increasing pH_B. Maximal buffering (dotted arrow) is observed in the range between the $2\,pK's$.

B. Electrochemical gating

As previously mentioned, E_{OX} will induce σ_O and σ_{DL} which together set ψ_O. For an interface exhibiting a single ionizable group (the single-pK model), σ_O first responds to E_{OX} until all charges (N_S) have responded [9] . During this process ψ_O does not change and the surface is said to be "buffering". However, in many cases with amphoteric interfaces such as Al_2O_3 and SiO_2, the nature of the buffering strongly depends on ΔpK and N_S. The choice of $pK_a = 10$ and $pK_b = 5$ for the present polysilicon interface under consideration represents a non-Nernstian surface with a pH_{PZC} around $pH_B = 7.5$. This corresponds to low pH sensitivity in the given ΔpK range and hence extremely low buffering. In Fig. 2(c&d), we compare the change in ψ_O for varying E_{OX} at different pH_B and n_O values. A slight skewing is observed [Fig. 2(c)]. Buffering is rather weak for intermediate pH values close to the PZC but gets stronger at extreme pH values. The skewing (slight sigmoid tendency) indicative of buffering is tunable as a function of E_{OX}. In Fig. 2(d), we notice that the maximal change in ψ_O with E_{OX} is strongest for the lowest n_O, in agreement with the results of Jiang and Stein[9]. This is because at low n_O , very little charge is available to screen a given modulation in ψ_O or σ_O, while at high n_O a small shift in σ_O can cause large changes in σ_{DL} and hence a substantial swing in ψ_O is energetically unfavorable.

Under negative E_{OX} conditions we notice that varying pK_b [Fig. 2(e)] modulates the surface potential even at zero E_{OX}. Such changes in surface ionizability can be

achieved by suitable self assembled monolayer (SAM) formations [47]. If we flip the surface constants, i.e. $pK_a = 10$ and $pK_b = 5$, maximal buffering is observed within the ΔpK range indicating a Nernstian pH response [Fig. 2(f)]. As previously mentioned, the effect of the ion size was weak for NaCl salts in these simulations as ψ_O never rose above $\sim 4 - 5\frac{kT}{e}$. The above simulations show that in addition to pH and bulk salinity E_{OX} can be tuned to affect the properties of the interface to a desired region of operation.

C. EOS capacitance-voltage (CV) measurements

Polysilicon-Oxide-Silicon capacitors were fabricated as described earlier. V_{REF} was swept from −10V to +10V. At −10V, the silicon was in accumulation (positive interface charge). As V_{REF} was swept positive, the charge in silicon was depleted, and finally at +10V it was inverted. The effect of the double layer modulation or pH_B on the surface potential is that the DC operating point is affected, which shifts the flat-band voltage (V_{FB}) of the capacitor stack [Fig. 3(a)]. In Fig. 3 we chose to plot only the transition region and not the entire range of the V_{REF} sweep.

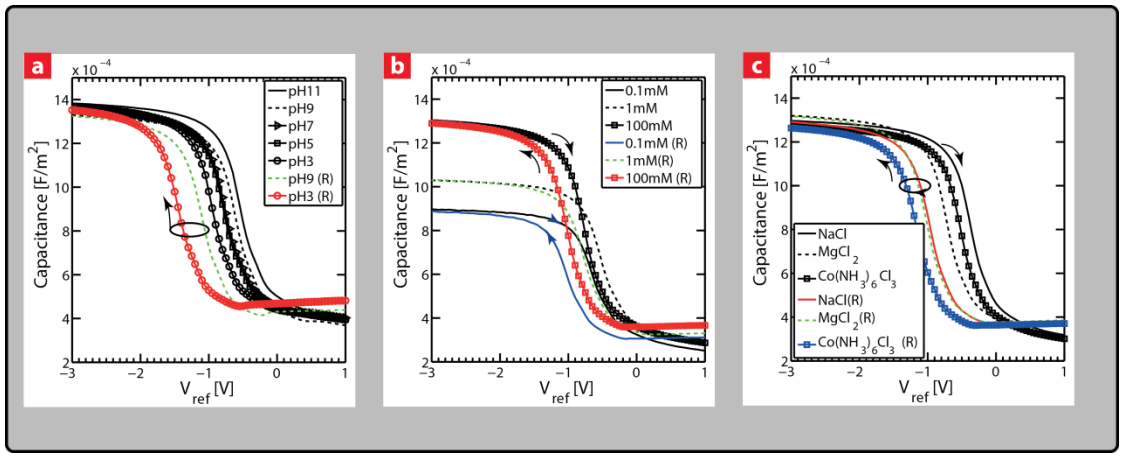

Figure 3 Experimental CV analyses depicting V_{FB} shifts for, (a) varying pH_B. A strong pH_B-dependent hysteresis is observed while performing cyclic sweeps. A lowering in V_{FB} is observed when the reference electrode is swept from positive to negative voltages (indicated by arrow/circle) implying a net positive remnant surface charge (b) varying bulk ion concentration (n_O). The hysteretic window at constant pH_B is insensitive to n_O while the accumulation region capacitance is dependent on n_O and (c) varying cationic valency (z). Varying (z) influences the double layer composition which further influences σ_O. Divalent cations shift the V_{FB} lower while trivalent ions induce a slight increase. C_{DL} is lower for the trivalent cations. Here (R) denotes the reverse sweep in (a-c).

A linear response in V_{FB} with respect to pH_B variation was noticed (~50mV/pH) when sweeping V_{REF} from -10V to +10 V. A strong hysteresis effect was observed when V_{REF} was cycled from -10V to +10V and back to -10V as shown in Fig. 3(a), for $pH_B = 7$ and $pH_B = 9$. This hysteretic effect got slightly larger with decreasing pH_B (not shown) and was found to be strongly dependent on the type of interface. For example, we found that both Al_2O_3 and poly-Si interfaces showed distinct hysteresis [48, 49] while thermal SiO_2 showed a negligible hysteresis upon exposure to pH solutions (not shown). Since E_{OX} can influence σ_O similar to the effect of pH_B, as described earlier (Fig. 2), the varying DC sweep affects the ionization state of the

interface which in turn affects surface recovery. When V_{REF} is swept from -10V to +10V, the field in the oxide in the beginning promotes anion adsorption or interface deprotonation and results in a negative σ_O. This deprotonation effect is strongly dependent on the choice of pK_a and pK_b. As the forward sweep proceeds towards +10V, this negative charge is poorly neutralized due to a small β_S, which renders a higher V_{FB}. On the reverse sweep, the surface is completely protonated or neutralized and hence σ_O is more positive. This $+\sigma_O$ only dissociates over the time course of the sweep, resulting in a lower V_{FB}. The hysteresis is similar to the trap charge effect in electronic devices. In order to confirm that this hysteretic effect is indeed mostly due to protons instead of ions, we performed CV sweeps at different n_O at $pH_B = 7$ and found that the hysteretic window was almost independent of n_O. V_{FB} increased by ~30mV when n_O varied from $100\mu M$ to $1mM$ but then slightly decreased upon further n_O increase [Fig. 3(b)]. This slight dependence of ψ_O on n_O is attributed to β_S. The sensitivity of σ_O to changes in the bulk electrolyte can be estimated by [4]

$$\sigma_O = C_i \cdot \psi_O = -\sigma_{DL} \qquad (18)$$

where C_i is the total capacitance seen by the interface:

$$C_i = \frac{C_{DL} \cdot C_{Stern}}{C_{DL} + C_{Stern}} \qquad (19)$$

Here σ_{DL} is the charge in the double layer, and C_{Stern} is the Stern layer capacitance which is generally considered immobile. A change in n_O directly affects σ_O via σ_{DL}

[Eq. (18)] which inturn affects C_{DL} and ψ_O self-consistently. The Boltzmann relation in Eq. (7) directly implies that a change in ψ_O affects H_S^+. However, the surface buffering capacity β_S will try to maintain H_S^+ constant by ensuring a new surface chemical equilibrium satisfied by Eq. (8). If β_S is small, C_{DL} can strongly regulate ψ_O [4], where the surface is maximally sensitive to ions and least sensitive to pH.

In order to further validate field-dependent ionic activity, we also varied the $\frac{z}{\nu}$ (valency/volume) ratio of the cation. Ionic size and valency play a crucial role in the double layer formation [32, 50]. Hence field-induced double layer modification serves as a suitable control to validate electrochemical response over the electrolyte interface. Size and valency sets a constraint on the width of the double layer which is strongly surface potential dependent (see Appendix A). When V_{REF} was swept from −10V to +10V we observed a reduction in V_{FB} when $MgCl_2$ replaced $NaCl$ in the electrolyte but a slight increase in V_{FB} when $Co(NH_3)_6Cl_3$ replaced $MgCl_2$ [Fig. 3(c)]. For the latter, this effect was accompanied by a corresponding decrease in the accumulation capacitance C_{acc}, while with $MgCl_2$, C_{acc} increased. We attribute the decrease in capacitance with $Co(NH_3)_6Cl_3$ to the Steric effect, which imposes packing constraints on the thickness of the condensed ionic layer and the effective C_{Stern}. It however appears that under the given field conditions and concentrations of $MgCl_2$ used the Steric effect factor is less dominant.

However, the net reversal in ψ_O observed with the trivalent cations cannot be

accounted for solely by the Steric effect. ψ_O reversal is possible with trivalent ions even at extremely low n_O [39] primarily due to electrostatic correlations. This seems to suggest that the predominant factors that determine the onset of potential reversal are the ionic $\frac{z}{\nu}$ ratio and strong ion-ion interaction between multivalent ions. Revealing the interdependence between n_O and the $\frac{z}{\nu}$ ratio is currently work in progress and will be reported in the future.

D. CvMOS – transient responses

Figure 4(a-f) summarizes the transient responses of the CvMOS for varying n_O under different pH_B conditions of 11, 7 and 3. The electrolyte bulk was held constant at 0.8V with respect to the source at ground. The CG pulse train was switched between +15V and –15V while reading intermittently at +10V. The drain bias V_D was held at 1V throughout the experiment. When a +15V CG bias was applied, I_D increased. However, the field in the SG oxide (E_{SG_OX}) during the rising pulse became more positive looking into the electrolyte. This immediately resulted in a net negative charge in solution by a combination of σ_O and σ_{DL}. When the CG was re-biased to +10V, the $-\sigma_O$ induced during the previous +15V application remained at the surface (hysteresis). This caused the I_D between 110 – 170 seconds to be smaller than the

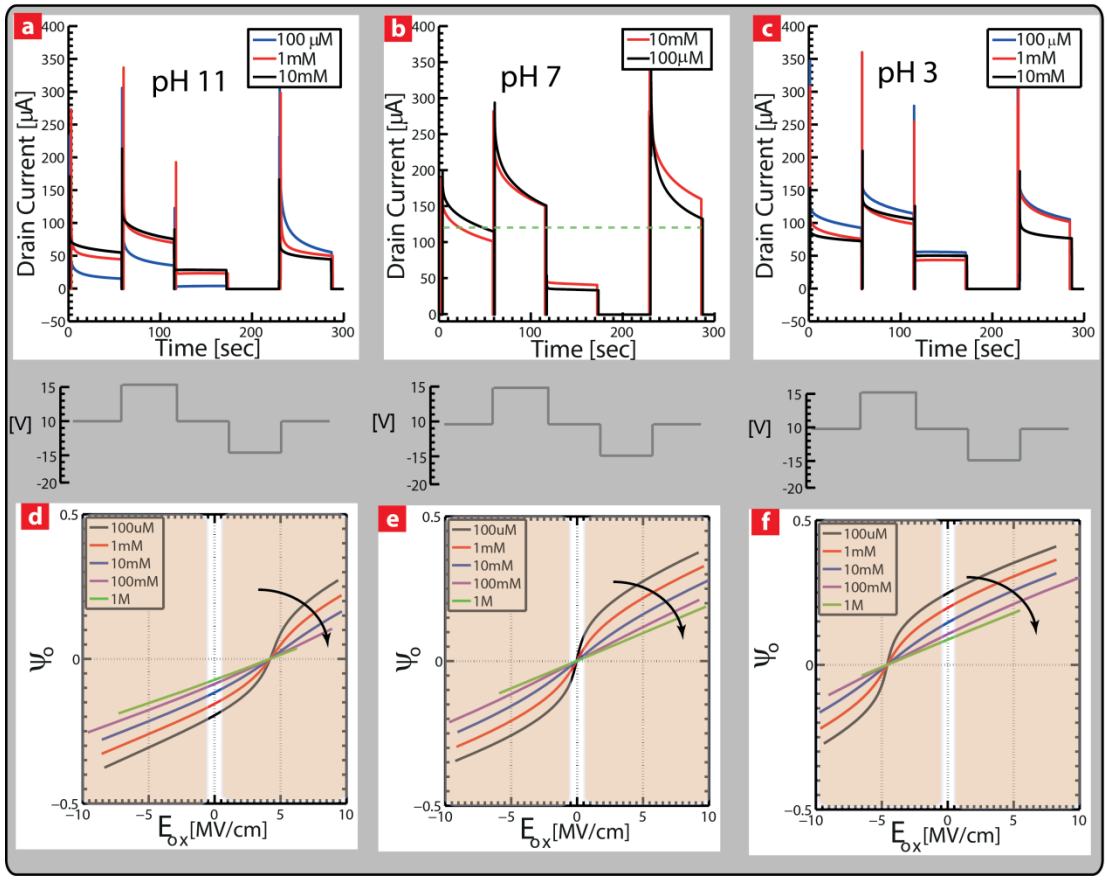

Figure 4. Transient recordings under CG pulse trains. Drain current output as a function of varying n_O at (a) $pH_B = 11$, (b) $pH_B = 7$ and (c) $pH_B = 3$. The pulse train amplitude and duration are shown under each figure. Calculated ψ_O as a function of E_{OX} for varying n_O for (d) $pH_B = 11$, (e) $pH_B = 7$ and (f) $pH_B = 3$, using $pK_a = 10$ and $pK_b = 5$. At $pH_B = 11$, ψ_O is net negative for E_{SG_OX} close to $0 MV/cm$ and becomes more negative with decreasing n_O. This is reflected in the current levels during the transient recordings. At $pH_B = 7$ the current levels flip when E_{SG_OX} is switched from positive to negative since ψ_O is positive at the positive E_{OX} and negative at negative E_{OX}. At $pH_B = 3$, ψ_O is net positive and increases with decreasing n_O. In all three cases, the drain current is higher between 230 – 285 seconds than the initial state between 0 and 60 seconds. This is attributed to net positive charge due to field-induced protonation which remains after the negative gating pulse is relaxed. This is similar to the observed hysteresis in Fig. 3. The regions between the dotted lines in (d-f) represent the fields during readout. Solid arrows in (d-f) represent the direction of increasing n_O.

initial 0 – 55 seconds. On application of a –15V CG bias, E_{SG_OX} became negative

and caused a net positive charge building up at the SG interface which enhanced H^+ adsorption. When the CG was re-biased to +10V between 230 – 285 seconds, I_d was higher than the initial readout state between 0 – 55 seconds [dotted line in Fig. 4(b)]. In order to confirm that protonation was the dominant effect during and after the negative gating period, we performed experiments in the presence and absence of a competing solution buffer (TRIS) [Appendix A, Fig. 35(b)] at pH_B=7. In the presence of TRIS, no increase in current was observed after application of the −15V CG pulse. In the absence of electrolyte and with the SG directly probed to ground [Appendix A, Fig. 35(c)], the transient current recording showed no variation after +10V, +15V and -15V CG bias application. This strengthens the assertion that no charge was either injected or erased into the FG during the CG bias application and the main reason for the observed differences in current levels is surface charge regulation.

For pH_B=11, the surface was already buffering [Fig. 4(d)] within the experimental E_{SG_OX} range (*the un-shaded region*). We observed that ψ_O was negative in the beginning, close to the zero E_{SG_OX} condition. With increasing n_O , ψ_O became more positive, which was reproduced in the transient response [Fig. 4(a)] reflected by a higher I_D for increasing n_O within the initial 0 – 60 seconds. After application of a −15V CG pulse between 170 - 230 seconds, however, we observed a recovery to higher I_D and a longer settling time with decreasing n_O. We attribute this to an increased hysteretic effect possibly due to increased cation adsorption at high pH_B. This coupled with a larger surface potential shift at lower n_O can potentially lead to

different rates of surface re-equilibration. Quantification of cation adsorption under such conditions however is difficult to decouple and is at present a measurement challenge. At pH_B = 7, however the surface potential was closer to zero around the readout condition of $E_{OX} \sim 0.01V/nm$. The model dictated a reversal in ψ_O [Fig. 4(e)] when E_{SG_OX} toggled between positive and negative values. This was experimentally observed in Fig. 4(b) with opposite shifts in I_D after the +15V and −15V CG pulses in comparison with the initial 0 – 60 seconds. This clearly showed that although during readout E_{SG_OX} was close to zero, the carryover net charge and ψ_O from the previous CG pulse remained and thus the gated surface state was observed. At pH_B = 3, ψ_O was highly positive [Fig. 4(f)] to begin with and increased with decreasing n_O. I_D was also found to increase after gating by positive and negative fields [Fig. 4(c)].

E. CvMOS – quasi-static response

Figure 5(a) summarizes the pH response of the CvMOS in terms of the V_{th} shifts observed from CG (V_{th_CG}). ψ_O was calculated via Eq. (1) after extracting the capacitive amplification ratio experimentally [Appendix A, Fig. 36(a)]. The pH_B response showed a non-Nernstian characteristic with a clear plateau around pH_B = 8 (i.e. pH_{PZC}). Increasing n_O lowered ψ_O at low pH_B but enhanced ψ_O slightly at high pH_B. This is consistent with the notion that ion adsorption plays little

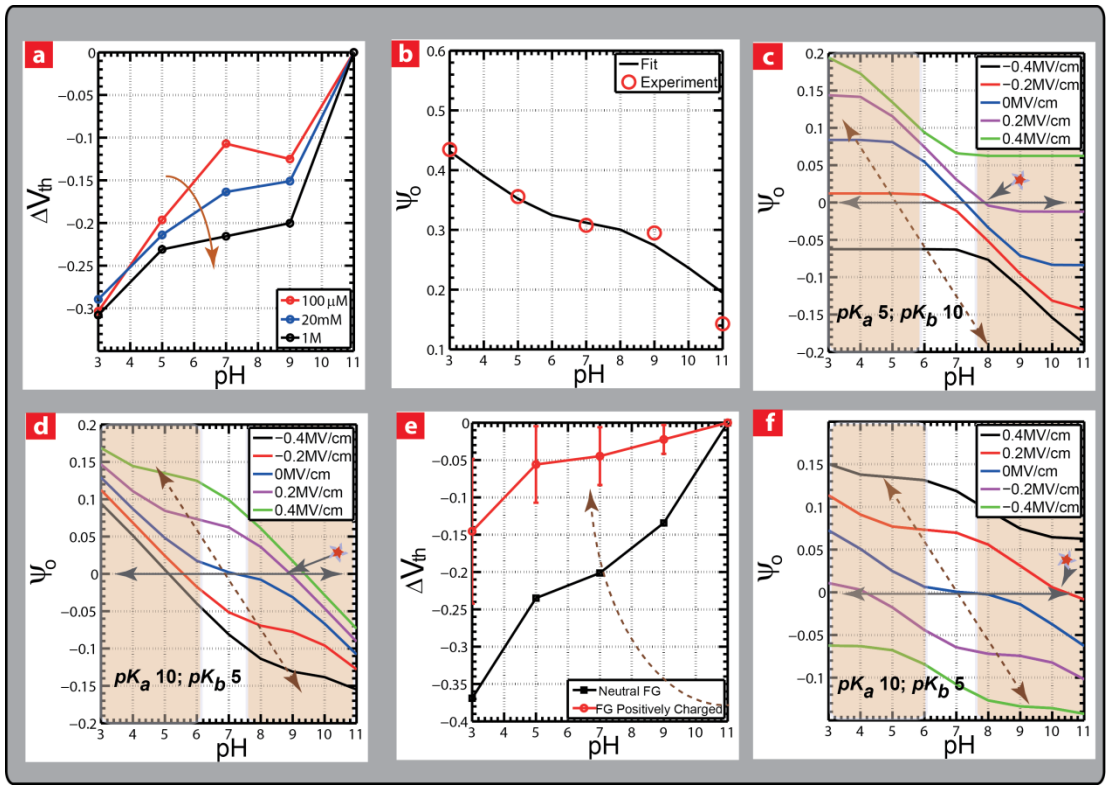

Figure 5. (a) ΔV_{th} (Representative of ψ_O) as a function of pH_B for varying n_O. The slope of the pH_B response reduces in the range between $pK's$ while it increases at extreme pH_B values. Cations are presumed to contribute to the slight increase in ψ_O at high pH_B. Arrow indicates increasing order of n_O (b) Theoretical fit to the experimental pH_B response reveals ΔpK of 5 for a given surface site density of $10^{17} m^{-2}$. ψ_O vs. pH_B for varying E_{OX} with (c) $pK_a < pK_b$ and (d) $pK_a > pK_b$. Both responses indicate a shift in pH_{PZC} (star) towards higher pH_B as E_{OX} is increased while the pH insensitive region shifts towards higher pH_B (c) and lower pH_B (d), with increasing E_{OX} respectively. This is primarily due to the different ionization states of the surface dependent on the choice of pK_a and pK_b. (e) Experimentally extracted pH_B response as a function of positive E_{OX} in the SG oxide, achieved by $+Q_{FG}$. Results show the pH insensitive region shifts towards lower pH_B. Error bar represents average over 3 experimental runs. (f) ψ_O vs. pH_B for varying E_{OX} with $pK_a > pK_b$ and lower N_s ($5\times10^{16} m^{-2}$). The modulation in pH_{PZC} is a lot more exaggerated.

role in shifting ψ_O at physiologically relevant pH_B, because the opposite would have meant an increase in ψ_O due to Cl^- ion binding. Also as n_O increases, the surface

buffering property decreases and hence affects the overall pH_B response. This can be understood from Eq. (13) and specifically by closely examining the sensitivity parameter α. It is immediately clear that a small β_S competes with C_i and determines the overall pH_B response as a function of n_O. At high n_O, C_i is much larger than β_S and hence results in a reduced pH_B response. At high pH_B the slight increase in ψ_O with varying n_O can be attributed to simultaneous H^+ and Na^+ ion binding [48]. This range of pH_B however is too small to establish a meaningful conclusion. It is quite clear that changing n_O does have an influence on β_S and ψ_O primarily from the buffering perspective. We do however point out that n_O would affect ψ_O even for surfaces that are uncharged or exhibit a constant charge condition. This would then primarily occur due to the change in C_i. Figure 5(b) provides a fit to the experimental pH_B response using the $2\,pK$ model presented earlier. A pK_b of 5.0 and pK_a of 10.0 was extracted. Figure 5(c&d) shows the simulated effect of E_{OX} induced gating on the pH_B response for two distinct combinations of pK_a and pK_b. In both cases the pH_{PZC} shifts to higher pH values as E_{OX} increases. However for the non-Nernstian interface where pK_b is lower than pK_a [Fig. 5(d)], the shift in pH_{PZC} is much higher (*horizontal arrow*). The pH insensitive region for this surface moves towards lower pH_B values as E_{OX} increases (*dotted arrow*). This shows that the effect of E_{OX} is similar to varying pH_B as both can tune σ_O. E_{OX} serves as an electrical factor, while pH_B as a chemical factor. We also experimentally observed this electrochemical

gating effect by injecting charges onto the FG. We applied a CG bias of ~40V for approximately 30 seconds while holding V_{REF} at 0V. Due to the larger capacitive coupling from SG, V_{FG} remained closer to V_{REF} and did not rise by more than 4~5V. E_{CG_OX} during this pulse period promoted FN tunneling which resulted in a net positive Q_{FG}. It is important to note that in the present study, with the given geometry constraints, E_{SG_OX} potentially achieved values of $0.02-0.2V/nm$ when $Q_{FG} \sim 8-20pC$. A quick (15 seconds) CG ramp was used to monitor the new surface charge state. We found that with $+Q_{FG}$ present, the pH_B response was dramatically affected and the pH insensitive region moved to lower pH_B, which resulted in an overall reduced pH response [Fig. 5(e)], which is in line with the simulation result shown in Fig. 5(d). The surface model also dictates that by reducing the density of surface hydroxyl groups, the pH_{PZC} shift was more pronounced [Fig. 5(f)]. Taken together the CV, IV and transient responses suggest that surfaces exhibiting a non-Nernstian response with large ΔpK will undergo a hysteresis in a saline environment. Ion adsorption does play a role under certain pH_B conditions [48, 49] but a better treatment of the site binding parameters is needed to account for such subtle effects.

F. CvMOS – programming response and the role of the reference electrode

We recall that V_{FG} is influenced by ψ_O which is pH_B and C_{DL} dependent. Also from the transient measurements it is clear that at small positive CG pulses the net carry-over charge is negative. Hence as V_{CG} is initially increased, V_{FG} perturbs ψ_O inducing

a net $-\sigma_O$ which couples back to influence the transistor current. As V_{CG} is further increased V_{FG} does not rise as high due to the influence of V_{REF}. The E_{CG_OX} increases favoring FN tunneling [28] to create a net positive Q_{FG}, reducing V_{th} measured from the CG [Fig. 6(a)]. V_{FG} is more positive as the tunneling process ensues due to the positive Q_{FG} [Appendix A, Fig. 36(c)]. This would necessarily imply that E_{CG_OX} lowers and E_{SG_OX} increases. The total threshold voltage shift (V_{th_CG}) is attributed to Q_{FG} and its net effect on $\sigma_{DL}+\sigma_O$. We reiterate that during tunneling, there is no charge leakage into the solution as measured in control experiments (not shown). When the reference electrode is floated, however, the capacitive coupling dramatically reduces and the FG is no longer pulled to a defined electrolyte potential. This ensures that V_{FG} rises with V_{CG} with increasing E_{TOX} to promote electron injection ($-Q_{FG}$) into the FG, thereby increasing the V_{th} measured from the CG [Appendix A, Fig. 36(b)]. This operation is particularly significant when attempting to manipulate charged biomolecules such as DNA as reported in part II.

In order to confirm the interplay between σ_{DL} and Q_{FG}, we performed experiments by changing n_O and hence C_{DL}. We found that C_{DL} strongly influenced the tunneling characteristics [Fig. 6(a)]. As C_{DL} lowered so did the V_{REF} coupling to the FG. This caused V_{FG} to rise higher with V_{CG} which lowered electron out-tunneling and favored electron in-tunneling, and hence resulted in a smaller net Q_{FG} after $V_{CG} > 30$V.

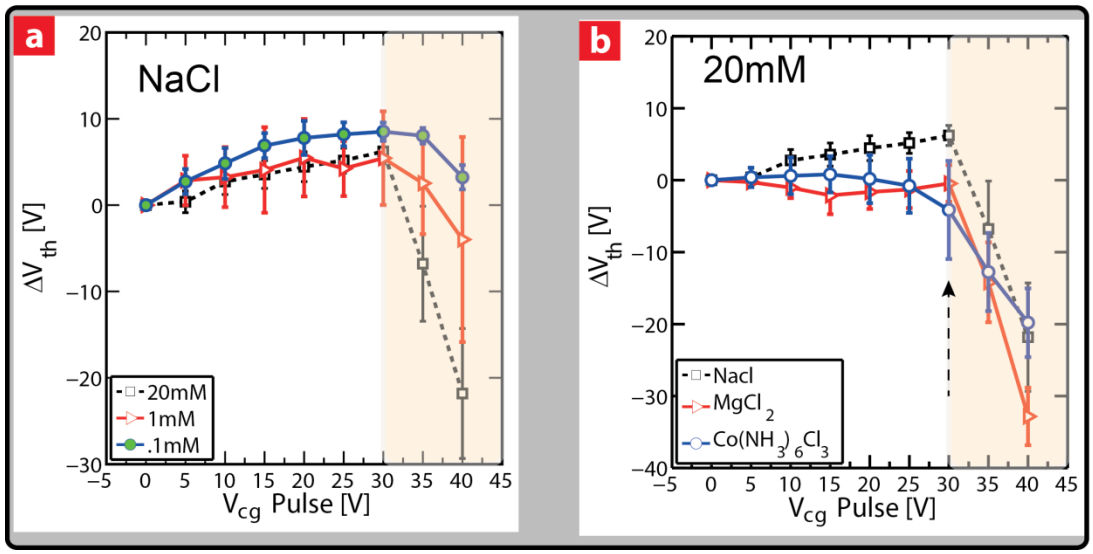

Figure 6. ΔV_{th_CG} as a function of the CG pulse amplitude for variations in (a) n_O for a NaCl electrolyte and (b)cationic valency for CvMOS with an amplification ratio of 20 at a bulk n_O of 20mM. An initial increase in ΔV_{th} at low to moderate CG voltages is attributed to surface deprotonation and a net remnant negative ψ_O. Due to asymmetric CG and SG capacitances, V_{FG} is pulled closer to V_{REF}. This ensures that at sufficiently high V_{CG} the V_{FG} does not rise much which leads to large E_{CG_OX} for FN tunneling. Reduction in n_O and C_{DL} weakens the coupling between the FG and V_{REF}, causing E_{CG_OX} and net Q_{FG} to reduce. Varying cationic valency indicates more pronounced shifts in ΔV_{th_CG} around the knee point (i.e. where tunneling begins) (shown by dotted arrow) especially with trivalent salts in comparison to mono and divalent salts. A decrease in the overall ΔV_{th_CG} with trivalent salts upon tunneling is consistent with the notion that C_{DL} is also decreasing. Error bars represent an average over 3 experimental runs.

The small initial increase in ΔV_{th} at low to moderate CG voltages is attributed to surface deprotonation and a net remnant negative ψ_O when V_{CG} is too low to cause tunneling.

In many experiments involving cell suspensions and biomolecules, the electrolyte composition is never just composed of single monovalent salts. In order to further develop the gating concept and corroborate the CV measurements, we performed

experiments keeping n_O constant at 20mM and varying the cationic $\frac{z}{\nu}$ ratio [Fig. 6(b)]. We observed that in the vicinity of the knee point [denoted by the arrow in Fig. 6(b)] where tunneling had just begun, the reduction in V_{th} was slightly more pronounced for $Co(NH_3)_6Cl_3$ in comparison to $NaCl$ and $MgCl_2$. This result shows that with $Co(NH_3)_6Cl_3$ present, ψ_O increased just after the programming pulse application. That is, it became more positive with $+Q_{FG}$. This finding is in line with the +10V to -10V V_{REF} (reverse) sweep performed during CV analysis [Fig. 3(c)] in which ψ_O was observed to be more positive (lower V_{FB}) with $Co(NH_3)_6Cl_3$. It is important to note that E-fields with similar strength and polarity are developed in the underlying oxide either under $+Q_{FG}$ conditions in the CvMOS or low to moderate $-V_{REF}$ application in the EOS structure. Taken together experimental evidence suggests field induced surface potential reversal due to a combination of both C_{DL} lowering and correlation effects [51] when experimenting with trivalent salts. This effect was not observed with monovalent or divalent salts. In Fig. 6(b), the overall magnitude of ΔV_{th} was also found to be lower for $Co(NH_3)_6Cl_3$. This is again consistent with the notion that C_{DL} affects the net Q_{FG} [Fig. 6(a)], and is in accordance with the CV measurements presented earlier in which C_{DL} was found to reduce for trivalent salts.

CONCLUDING REMARKS

We presented the dynamic surface charge modulation of a solid-electrolyte interface, and the concept of surface pH tuning. By modulating the polarity of stored charge, one can switch between a pH sensitive condition and a non-Nernstian surface. Transistor and EOS capacitor measurements are compared and a 2-pK model with surface charge regulation is presented. We conclude that proton adsorption and desorption is the primary reason for hysteresis at such interfaces, which also provides a method of probing the surface charge state. Quasi-static I-V measurements, CV profiles and high resolution transient recordings are presented to corroborate our findings.

Supplemental Material: Supplementary material accompanies this chapter. Refer Appendix A for details.

REFERENCES

[1] F. Uslu *et al.*, Biosens. Bioelectron. **19**, 1723 (2004).

[2] S. Ingebrandt *et al.*, Biosens. Bioelectron. **22**, 2834 (2007).

[3] N. Zehfroosh, M. Shahmohammadi, and S. Mohajerzadeh, Electron Device Letters, IEEE **31**, 1056 (2010).

[4] R. E. G. van Hal, J. C. T. Eijkel, and P. Bergveld, Sens. Actuators, B **24**, 201 (1995).

[5] S. Chen *et al.*, Nano Lett. **11**, 2334 (2011).

[6] O. Knopfmacher *et al.*, Nano Lett. **10**, 2268 (2010).

[7] P. Bergveld, Sens. Actuators, B **88**, 1 (2003).

[8] I. Y. Wong, M. J. Footer, and N. A. Melosh, Soft Matter **3**, 267 (2007).

[9] Z. Jiang, and D. Stein, Langmuir **26**, 8161 (2010).

[10] R. B. H. Veenhuis *et al.*, Lab on a Chip **9**, 3472 (2009).

[11] K. Ghowsi, and R. J. Gale, J. Chromatogr. A **559**, 95 (1991).

[12] R. B. M. Schasfoort *et al.*, Science **286**, 942 (1999).

[13] R. Karnik, K. Castelino, and A. Majumdar, Appl. Phys. Lett. **88**, 123114 (2006).

[14] R. Fan *et al.*, Phys.Rev.Lett. **95**, 086607 (2005).

[15] W. Guan, R. Fan, and M. A. Reed, Nat Commun **2** (2011).

[16] K. Horiuchi, and P. Dutta, Lab on a Chip **6**, 714 (2006).

[17] H. Daiguji, T. Adachi, and N. Tatsumi, Phys.Rev.E **78**, 026301 (2008).

[18] E. B. Kalman, I. Vlassiouk, and Z. S. Siwy, Adv. Mater. **20**, 293 (2008).

[19] Y. Liu *et al.*, Appl. Phys. Lett. **97**, 143109 (2010).

[20] Y. He *et al.*, ACS Nano **5**, 5509 (2011).

[21] Z. Jiang, and D. Stein, Phys.Rev.E **83**, 031203 (2011).

[22] W. R. McKinnon, D. Landheer, and G. Aers, J. Appl. Phys. **104**, 124701 (2008).

[23] N. Y. M. Shen *et al.*, IEEE Trans. Electron Devices **50**, 2171 (2003).

[24] T. Shibata, and T. Ohmi, IEEE Trans. Electron Devices **39**, 1444 (1992).

[25] J. Go *et al.*, ACS Nano **6**, 5972 (2012).

[26] J. Go, P. R. Nair, and M. A. Alam, J. Appl. Phys. **112**, 034516 (2012).

[27] Rino Micheloni, Luca Crippa, and A. Marelli, *Inside NAND Flash Memories* (Springer New York, 2010).

[28] F. Masuoka *et al.*, Solid-State Circuits, IEEE Journal of **22**, 548 (1987).

[29] C.-Y. Hsiao *et al.*, Biosens. Bioelectron. **24**, 1223 (2009).

[30] G. Wenga *et al.*, Biosens. Bioelectron. **40**, 141 (2013).

[31] R. Tsu, and L. Esaki, Appl. Phys. Lett. **22**, 562 (1973).

[32] M. S. Kilic, M. Z. Bazant, and A. Ajdari, Phys.Rev.E **75**, 021502 (2007).

[33] J. C. van Kerkhof, J. C. T. Eijkel, and P. Bergveld, Sens. Actuators, B **18**, 56 (1994).

[34] D. Ben-Yaakov *et al.*, J. Phys.: Condens. Matter **21**, 424106 (2009).

[35] D. Gillespie *et al.*, J. Colloid Interface Sci. **359**, 520 (2011).

[36] I. Borukhov, D. Andelman, and H. Orland, Phys.Rev.Lett. **79**, 435 (1997).

[37] J. A. Grant, and B. T. Pickup, J. Phys. Chem. **99**, 3503 (1995).

[38] B. I. Shklovskii, Phys.Rev.E **60**, 5802 (1999).

[39] F. H. J. van der Heyden *et al.*, Phys.Rev.Lett. **96**, 224502 (2006).

[40] R. Qiao, and N. R. Aluru, Phys.Rev.Lett. **92**, 198301 (2004).

[41] A. Y. Grosberg, T. T. Nguyen, and B. I. Shklovskii, Rev.Mod.Phys. **74**, 329 (2002).

[42] K. Besteman, M. A. G. Zevenbergen, and S. G. Lemay, Phys.Rev.E **72**, 061501 (2005).

[43] K. Besteman *et al.*, Phys.Rev.Lett. **93**, 170802 (2004).

[44] B. D. Storey, and M. Z. Bazant, Phys.Rev.E **86**, 056303 (2012).

[45] L. Bousse, N. F. de Rooij, and P. Bergveld, IEEE Trans. Electron Devices **30**, 1263 (1983).

[46] H. van den Vlekkert, L. Bousse, and N. de Rooij, J. Colloid Interface Sci. **122**, 336 (1988).

[47] A. van den Berg *et al.*, Sensors and Actuators **8**, 129 (1985).

[48] L. Bousse, N. F. De Rooij, and P. Bergveld, Surf. Sci. **135**, 479 (1983).

[49] A. Tarasov *et al.*, ACS Nano **6**, 9291 (2012).

[50] D. Ben-Yaakov *et al.*, Curr. Opin. Colloid Interface Sci. **16**, 542 (2011).

[51] T. T. Nguyen, and B. I. Shklovskii, Phys.Rev.E **64**, 041407 (2001).

[52] See Appendix A for additional details of the physical principles that describe the device operation, control experiments that support details presented in the main text, simulation of the tunneling operation and Table outlining the equation set describing the working of the *CυMOS* transistor.

CHAPTER 3- PROGRAMMABLE ION SENSITIVE TRANSISTOR INTERFACES: BIOMOLECULAR SENSING AND MANIPULATION

CHAPTER OVERVIEW

The Chemoreceptive Neuron MOS transistor (CvMOS) described in part I is further used to monitor the adsorption and interaction of DNA molecules and subsequently manipulate the adsorbed biomolecules with injected static charge. Adsorption of DNA molecules onto poly-l-lysine coated sensing gates (SG) modulates the floating gate (FG) potential (V_{FG}), which is reflected as a threshold voltage shift measured from the control gate (CG), (V_{th_CG}). The asymmetric capacitive coupling between the CG and SG to the FG results in V_{th_CG} amplification. The electric field in the SG oxide (E_{SG_OX}) is fundamentally different when we drive the current readout with V_{CG} and V_{REF} (i.e. the potential applied to the CG and reference electrode respectively). V_{CG} driven readout induces a larger E_{SG_OX}, leading to a larger V_{th_CG} shift when DNA is present. Simulation studies indicate that the counter ion screening within the DNA membrane is responsible for this effect. The DNA manipulation mechanism is enabled by tunneling electrons (program) or holes (erase) onto FG to produce repulsive/attractive forces. Programming leads to repulsion and eventual desorption of

DNA, while erasing re-establishes adsorption. We further show that injected holes or electrons prior to DNA addition either aids or disrupts the immobilization process, which can be used for addressable sensor interfaces. To further substantiate DNA manipulation, we used impedance spectroscopy with a split ac-dc technique to reveal the net interface impedance before and after charge injection.

INTRODUCTION

Simultaneous detection and manipulation of biomolecules can open up exciting studies of the fundamental properties of proteins/DNA, controlled drug delivery and reversible bio-electronic interfaces. While recent literature describes biomolecular detection by transistors [1-7], it has so far been very difficult to realize the opposite, i.e., using the transistor for molecular actuation. Serving as an affordable, fast and extremely sensitive tool, the transistor platform is easier to integrate and scale than optical techniques and could also facilitate label-free readout [8]. Present non-faradaic sensors rely on the conventional ISFET (ion sensitive field effect transistor) approach [7, 9]. The surface of the open-gate FET is made sensitive to ion and molecule adsorption, which subsequently modulates the transistor current. The threshold voltage in this case is measured with respect to a reference electrode, often by Ag/AgCl in a chlorine-rich buffer. However, recent efforts [5, 8, 10, 11] have been directed towards achieving dual gate control which gives intrinsic amplification of the surface potential shift. Given the small size and high sensitivity of these dual-gate devices, sensing the intrinsic properties and interactions of proteins, DNA and other small bio-molecules

becomes plausible [7, 9].

Traditionally, the gate metal of the FET is removed and sensing is performed on the gate oxide or functional coatings. Alternatively, the gate metal can be left electrically floating and the target adsorption is on the metal surface [12]. A reference electrode such as Ag/AgCl or Pt in the electrolyte biases the transistor at the appropriate operating point. This is commonly known as the ISFET[13]. In comparison, the CvMOS [14] [Fig. 7(a)] makes use of an independently driven control gate, hence alleviating the sole reliance on the reference electrode for biasing, which can nevertheless still be used to set the bulk electrolyte potential and affect the sensor output. The use of V_{REF} can lower the read voltage to avoid read disturb, as high V_{CG} can induce unintended nonvolatile charge injection.

Optical detection schemes of DNA hybridization and protein binding rely on fluorescent labels. Not only can labeling affect the delicate nature of molecular interactions, but integrating optical detection with sub-millisecond monitoring is difficult. CMOS electrochemical sensors on the other hand, enable aggressive miniaturization, label-free operation [15], high spatial and temporal resolution, and high sensitivity based on both capacitance and charge [13, 16]. Moreover, transistor detection of DNA hybridization through surface charge sensing can potentially realize electronic micro-assays [3, 17].

Recent efforts towards dynamic control of biomolecular activity have included electrophoretic and electrochemically driven stimuli [18, 19]. Electric-field manipulation is preferred compared to faradaic schemes as redox reactions often

interfere and disturb the delicate molecular properties. It is also possible to ensure sufficiently high electric field gradients with low-voltage operation [20] which is dependent on the double layer capacitance. Under such conditions, it was proposed that the sensing electrode can still be treated as purely polarizable, as in the conventional Gouy-Chapman (GC) double-layer theory.

Recently, Rant and colleagues[18] provided compelling experimental evidence that the oligonucleotides desorption occurred during an unsteady electrochemical state away from equilibrium, contrary to the notion that desorption was well captured by the GC model where an equilibrium could always be established. Similar studies by Fixe and colleagues [21] demonstrated that DNA desorption occurred after sub-milli-second pulses between a surface electrode and the bulk electrolyte, further indicating that desorption happened well before equilibrated double-layer conditions were reached. This was believed to be primarily due to counterion descreening exposing the DNA backbone which gets electrostatically repelled, reorganizes and then re-adsorbs. More recently Reddy and colleagues [22] demonstrated the effect of self heating in SOI transistors as a method for local desorption with simultaneously sensing capabilities. This is an attractive alternative approach but precise thermal control at such scales is still challenging.

On the other hand controlled nonvolatile charge injection, by either hot electron injection or Fowler-Nordheim (F-N) tunneling causes the FG to hold static charge of either polarity. This charge capacitively couples to the sensing gate which imparts an electrostatic force on ions (see part I) and adsorbed biomolecules.

In this chapter we present electrical monitoring of DNA hybridization and subsequent

manipulation of the adsorbed biomolecules. A battery of experiments was used for calibration, including quasi-static analysis with and without the reference electrode, charge injection effects and impedance spectroscopy through a new split gate approach.

METHODS

A. Materials

The sensor chips were the similar to the ones used in Part I. The sensing gates were coated with poly-l-lysine (Sigma Aldrich), set aside for two hours and then washed with DI water, dried and stored at 4^{o}C before use. DNA strands B1 and B2 (see Table 4, Appendix-B) were procured from IDT DNA and were 99.9% HPLC purified. These 20 base-pair (bp) oligonucleotides (~7nm length) were kept at a stock concentration of 0.5mM in a 10mM saline (TE) buffer (10 mM Tris at pH 8.0, 10 mM NaCl, and 1 mM EDTA). The DNA concentration used during measurements was diluted to ~5μM in order to achieve sufficient surface coverage without suffering from Coulombic repulsion which normally occurs at high probe densities [23]. DNA strands (C1, C2) (24bp) and (D1, D2) (48bp) were additionally used under identical conditions to ascertain the impedance dependence on molecular length before and after hybridization. The bond pads were isolated from the sensing region via an epoxy coating which also served as the fluid reservoir. Fluid was dispensed and removed from the well via pipettes.

B. Electrical Instrumentation

In addition to the equipment used in Part I to perform IV analysis, impedance measurements were performed by monitoring the small-signal transistor gain as a function of frequency [24]. A single-toned sinusoid waveform was applied (Stanford Research Systems DS345, CA, USA) through a solution gate (Ag/AgCl reference electrode) while the DC bias was supplied via the control gate independently (Keithley 2400, USA) (Appendix-B, Fig. 37). The output current of the transistor was fed to a lock-in amplifier (Stanford Research Systems, SR844, CA, USA) through the TIA. Bode responses and current/voltage (I/V) sweeps were measured intermittently to ascertain the operating point stability. The CG was then adaptively biased to maintain a constant operating point during the impedance measurement.

DEVICE OPERATION AND SENSING PRINCIPLES

A. Quasi-static operations

V_{FG} is perturbed by analyte adsorption on the SG. Upon DNA immobilization, the readout current is modulated by a change in the V_{FG} from both the SG capacitance C_{SG} and ψ_O as outlined (see Table 5, Appendix-B). A V_{CG} sweep is then performed to determine V_{th_CG} when the drain current is at a constant $1\mu A$. As highlighted in part I of this chapter, V_{th_CG} driven readout results in an amplified measure of ψ_O and the amplification factor is primarily determined by the ratio between the two input capacitors C_{SG} and C_{CG}.

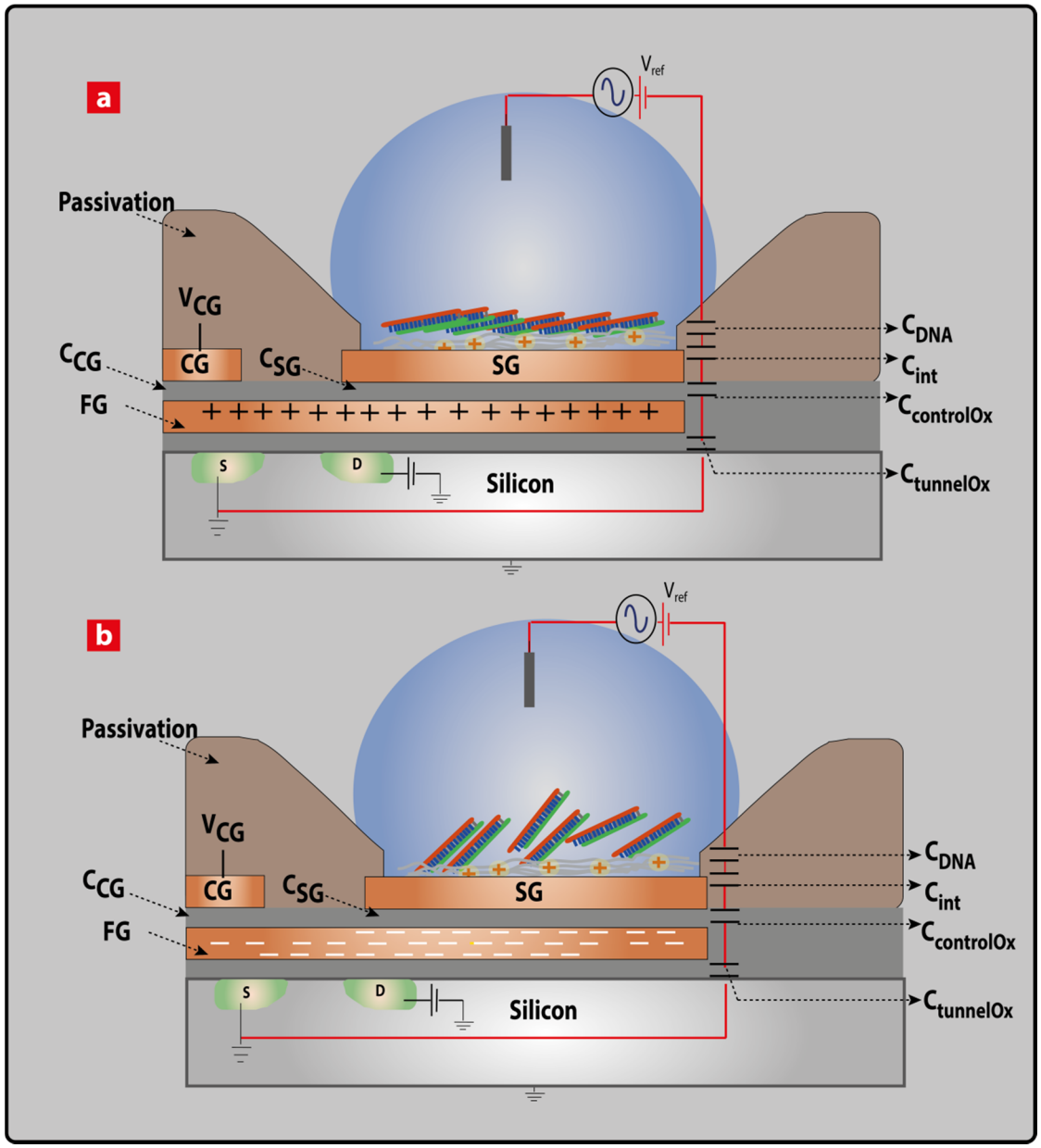

Figure 7 Schematic of the CvMOS transistor with independent control and sense gates. (a) DNA immobilization on the SG with FG charge erased (hole injection), resulting in DNA diffusion towards the poly-l-lysine coated surface and (b) DNA manipulation upon programming (electron injection).

Note that DNA itself is a dielectric and hence will give rise to additional capacitive effects at the interface, which is noticeable but not well understood, as the rotation angle will further affect the capacitive readout [25]. The subthreshold slope is directly

proportional to the total capacitance C_T (see Table 5, Appendix-B) seen from the FG, which makes the I/V sweep a unique method to simultaneously obtain ψ_O and total capacitance. In addition, by monitoring the subthreshold slope the reliability of the device is continuously monitored since degradation in slope can indicate ion migration into silicon for permanent device failure. In comparison, transient current measurements performed at a fixed CG bias reflect the combined effect of time-resolved shifts in ψ_O and net capacitive coupling.

B. DNA transistor interface

Over the last few years many models of the DNA-transistor interaction have been proposed to highlight the nature of charge modulation at the ISFET interface. Landheer and co-workers [26, 27] extended the earlier study by Schasfoort and colleagues [28], and illustrated the effects of the adsorbed biomembrane as ion permeable, resulting in a Donnan potential. Kruise et al. [29] and McKinnon et al. [30] showed that high intrinsic surface charge density negated and even cancelled the Donnan effect. Hence a Nernstian pH response is deleterious to biomolecular sensitivity. Shalev et al. [31] however recently showed that the maximal sensitivity of protein detection coincided with maximal pH sensitivity, in direct contradiction to known theories [29]. They argued this to be due to the interaction of the protein with surface sites. This issue has still not been resolved.

The Donnan theory formulation was later improved by Liu et al. [32] wherein ion permeation into the DNA layer was treated by accounting for the partition energy barrier. They explained that ion diffusion from a high permittivity medium (bulk) to a

low permittivity medium (the DNA membrane) is always associated with an energy penalty, leading to a low ion density within the membrane. DNA orientation on the surface plays an important role as it decides the net partition energy barrier [32]. It is thus reasonable to assume that the field in the underlying oxide plays an important role in determining the overall sensitivity [30] as molecular orientation and the local ionic environment can be field dependent [33]. In this study we incorporate different ion screening profiles within and outside the DNA membrane and show that this leads to a pronounced effect on the measured ψ_O. We then present the model framework to compare different partition energy barriers for distinct configurations.

C. Impedance spectroscopy

Impedance spectroscopy was realized through small-signal analysis using a split-gate approach as CG sets the DC bias and V_{REF} delivers the AC excitation independently. This scheme has an important advantage to independently tune the transistor's DC operating point at the pixel level while maintaining a constant global AC perturbation in the buffer. DNA immobilized on the sensing gate is analogous to an additional dielectric layer with a counterion cloud which can be modeled by an equivalent RC circuit. The main reason that justifies the RC model is that when operating at high DNA concentrations in this case ~1-5μM, the DNA strands orient in such a way to minimize Steric interactions and reduce the overall free energy[23, 34]. This results in a tightly packed film. The adsorbed DNA is also known to form an ion permeable membrane [26] which causes a fixed charge density within the adsorbed DNA film. This allows for a Donnan potential to be set within the membrane which

further affects the surface potential shifts. In the AC impedimetric mode, this introduces a strongly resistive component into the interfacial impedance in addition to the dielectric property of the DNA. The frequency responses are attributed to both resistive and capacitive changes at the interface [4, 24, 29]. The transfer function can be modeled by a Bode (pole-zero) plot. We point out that such impedimetric approaches can be viewed as simple two-electrode systems [6] but integrating with FET's[24, 35-37] allows for simultaneous charge and capacitance estimation at the nanoscale.

The small-signal output can be represented by the simple relation [37] $v_{out} = i_d \times R_D$ where R_D is the feedback resistance and v_{out} is the small-signal output of the transimpedance amplifier. The small signal current i_D can be approximated by $g_m v_{gs}$ where g_m is the transconductance of the amplifier and v_{gs} is the intrinsic small-signal gate-to-source voltage. The transfer function $H(j\omega)$ depicting the relaxation across the DNA monolayer accounts for the effective reduction in v_{gs}, which further relates to the output voltage by $v_{out} = g_m H(j\omega) \times v_{ac} \times R_D$. $H(j\omega)$ can be expanded to;

$$H(j\omega) = \frac{1 + j\omega \times (R_{DNA} \times C_{DNA})}{1 + j\omega \times (R_{eff} \times (C_{OX} + C_{FG-BULK} + C_{DNA}))} \qquad (1)$$

ω and v_{ac} are the frequency and small-signal bias applied while C_{OX} is the gate oxide capacitance. The DNA monolayer is described by a resistance (R_{DNA}) and capacitance (C_{DNA}) in parallel. R_{eff} is the cumulative resistive contributions from both the reference electrode, the electrolyte and the adsorbed DNA film. $C_{FG-BULK}$ is the

parasitic capacitance from the floating gate to bulk.

The frequency response of the interfacial RC network has the pole (P_1) primarily dependent on the gate oxide capacitance, associated parasitics and electrolytic resistance. The first zero (Z_1) is described by the relaxation across the DNA film at the interface. In the absence of DNA, Z_1 does not exist.

$$P_1 \cong R_{eff} \times (C_{OX} + C_{FG-BULK} + C_{DNA}) \qquad (2)$$

and

$$Z_1 \cong R_{DNA} \times C_{DNA} \qquad (3)$$

By performing frequency sweeps, one can monitor the properties of the adsorbed film given that the operating point is held constant. Impedance spectroscopy can also provide a suitable method to benchmark the effects of charge-injection-induced surface manipulation, as reflected in the capacitance and resistance of the interfacial layer.

RESULTS AND DISCUSSION

A. Quasistatic readout

Figure 8(a) shows the variation in ψ_O upon ssDNA immobilization (C1) and subsequent complementary pair addition (C2) under different biasing conditions. The SG surface is coated with PLL which neutralizes the intrinsic hydroxyl charge rendering it suitable for DNA adsorption. We observe that when DNA immobilization and hybridization is measured with respect to V_{REF} with V_{CG} grounded, $\Delta\psi_O$ is

smaller even after compensating for capacitive amplification. This is in contrast to V_{CG} readout with V_{REF} pinned at 0.2V.

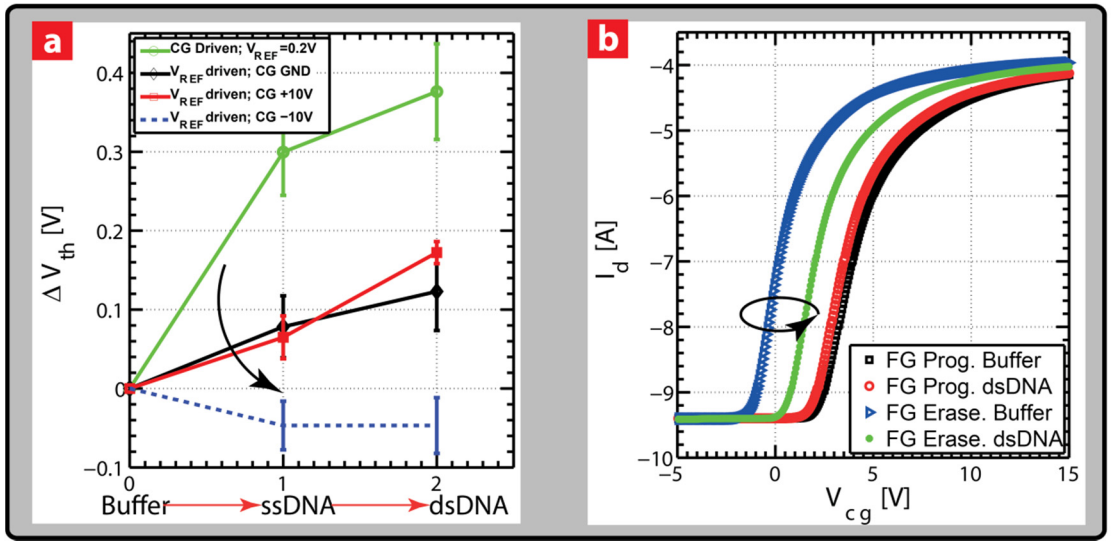

Figure 8. (a) Comparison between reference electrode and CG readouts during DNA immobilization and hybridization. A +10V CG bias during V_{REF} readout renders a $+E_{SG\_OX}$ in the SG oxide while a -10V renders a $-E_{SG\_OX}$. CG driven readout with V_{REF} at 0.2V shows a larger ψ_O shift prior to hybridization mainly due to different E_{SG_OX} conditions. During hybridization however $\Delta\psi_O$ (~60mV) is only marginally different between CG and V_{REF} readout. At $-E_{SG\_OX}$ conditions a slight reversal and diminished ψ_O is observed suggesting that the underlying field affects the net charge at the interface. At such field magnitude (0.05V/nm) DNA desorption does not occur but the ionic screening can be perturbed. (b) The effect of electron and hole injection into the FG prior to dsDNA (24mer) addition. With electrons injected, a very small shift in V_{th_CG} is observed, which for the given capacitive ratio of ~15 implies a ψ_O shift of approximately 10~15mV. With hole storage the shift in ψ_O is ~150mV.

We attribute this variation to differences in E_{SG_OX} during readout. A more positive E_{SG_OX} at 0.05V/nm exists during CG readout in comparison to V_{REF} readout where E_{SG_OX} is about ~0.005V/nm. This difference is balanced by a corresponding change in screening charge around the DNA molecule. The change in fields can also weakly

influence the molecular orientation. We attribute this to the lower screening charge within the membrane which results in a larger ψ_O shift. In order to further validate this effect, we offset V_{CG} during the V_{REF} sweep to create different E_{SG_OX} conditions. Under normal νMOS operation such input offsets should only translate to a parallel shift in the transconductance responses. However, we found that under $+V_{CG}$ offsets of +10V $\Delta\psi_O$ increased slightly upon (C1) and (C2) addition. A positive offset resulted in larger counterion (cation) descreening within the DNA membrane. A -10V, V_{CG} offset caused a negative E_{SG_OX} and resulted in an insensitive response. This is attributed to counterion accumulation which screens out most of the DNA intrinsic charge. It may also affect the DNA orientation rendering it less likely to lie flat on the surface [18, 33]. We observed a much reduced shift upon ssDNA (C1) addition and very little variation upon subsequent hybridization (C2). The given V_{CG} and V_{REF} biases are too low to cause program or erase operations on the FG (see part I). The change in E_{SG_OX} induced by a CG bias hence solely influences the DNA membrane.

In a separate study [Fig. 8(b)], in order to further corroborate field-induced DNA manipulation, we added pre-annealed dsDNA (C1, C2) onto the SG after programming (*electrons stored*) and erasing charges on and off FG. In this particular example we observed ~10pC of stored charge upon programming (*FG negatively charged*) for a capacitive amplification factor of ~15. Nominally 8-20pC of stored

charge can induce a $E_{SG\_OX} \sim \pm 0.02 \sim 0.2 \frac{V}{nm}$ for the choice of capacitance ratios used in this study and also without the need for a continuously applied CG bias (part I). Such fields as described in detail in part I can lead to shifts in ψ_O of ~50-70mV ($pH_B = 8$) during readout.

Once the FG is programmed or erased and DNA is added, the reference electrode and CG are temporarily floated prior to sweeping the CG bias for readout (i.e. a standby state). ψ_O strongly tracks V_{FG} during this period, primarily due to the strong capacitive coupling between SG and FG and weak coupling to the bulk (see part I). We point out that the source and drain connections are not perturbed during and due to the extremely small capacitance coupling to the FG have a negligible influence on V_{FG}. V_{FG} is then predominantly defined by $\frac{Q_{FG}}{C_T}$, which under the given conditions can reach values $\sim \pm 0.2 - 0.3V$ just prior to the readout sweep. Such dramatic changes in surface potential can strongly influence the nature of DNA immobilization and manipulation [20] , as interaction with a PLL-coated surface is mainly electrostatic in nature. It is interesting to note that the ideal condition would demand a low SG/CG and a large CG/FG coupling ratio to ensure maximal field modulation by injected charge. This however will affect the sensitivity to analyte detection [38]. Hence it poses a design tradeoff.

In Fig. 8(b) after electron injection the shift in V_{th_CG} decreased slightly (+10mV), while a significant increase in V_{th_CG} was induced upon hole storage (-

150mV). The above experiments indicate that DNA immobilization on SG is perturbed by attractive and repulsive force via charge-charge interaction and the underlying E_{SG_OX} can directly influence the adsorption and even the surface membrane structure. The ability to control DNA immobilization using programmed charge presents an opportunity to not only create addressable microarrays but also refresh the surface for continuous monitoring. For example, if hole injection promotes DNA adhesion and electron injection desorbs the adhered biomolecule, a buffer exchange after electron injection can refresh only the chosen sensor surface. We performed experiments to corroborate this hypothesis. DNA hybridization and subsequent manipulation were performed on PLL-coated SG. A capacitance amplification ratio of 22 was extracted prior to adding DNA. Here the reference electrode was left floating during readout to ensure maximal field modulation from the injected charge instead of the potential difference between SG and the reference electrode. We will discuss the implications of a floating electrolyte bias in detail later. Unless otherwise mentioned, V_D was held at 1 V during I/V sweeps.

Buffer was first dispensed and the I/V responses were recorded during the programming and erasing cycles. A significant V_{th_CG} shift of ~8V was observed implying ~+8pC of stored charge [Fig. 9(a)]. Single stranded DNA (ssDNA) (C1) was then added under the erased condition (*FG positively charged*). The V_{th_CG} shift was recorded 15 minutes after ssDNA addition and was shown in Fig. 9(b). Repeated sweeps were performed to make sure V_{th_CG} was stable before proceeding. The arrows indicate a net $-\psi_O$ contribution at the interface. Complementary ssDNA (C2)

subsequently created a further V_{th_CG} shift. We observe a $\Delta\psi_O$ on the order of ~100mV upon C1 addition and a further 150mV shift upon hybridization [Fig. 9(b)], consistent with previous studies on floating-gate MOS interfaces [1, 39] but in contrast to the 10-20mV shifts observed on conventional open-gate ISFET's [3, 37, 40].

Once a hybridization signal was recorded after ~40 min, we introduced a pipette filled with fresh buffer and gently sloshed back and forth 3~4 times till we replaced the entire buffer in order to remove loosely bound DNA. We observed no V_{th_CG} shift [Fig. 9(c)], which was likely due to the firmly immobilized DNA. We then programmed (electron injection) at this stage and observed the V_{th_CG} shift. During tunneling the V_{CG} pulse was maintained for a ~30 seconds. If the DNA molecules were to still be immobilized to the SG after programming, we should have observed a further increase in V_{th_CG}. However, we observed that the V_{th_CG} coincided with the curve corresponding to the pure buffer response with injected electrons [Fig. 9(d)]. At this point, we performed another buffer exchange to remove any loosely bound DNA as a consequence of electron injection. After a subsequent erasing operation we found the V_{th_CG} overlapped with the trace corresponding to pure buffer as shown in Fig. 9(d). It is critical to note that throughout the experiment the subthreshold slope did not degrade which is critical from a reliability perspective.

We also compared the effects of programming and erasing FG with and without buffer exchange (Appendix-B, Fig. 38). The measurements indicated that after electrons were injected and subsequently erased and without replacing the buffer,

V_{th_CG} recovered to the same point.

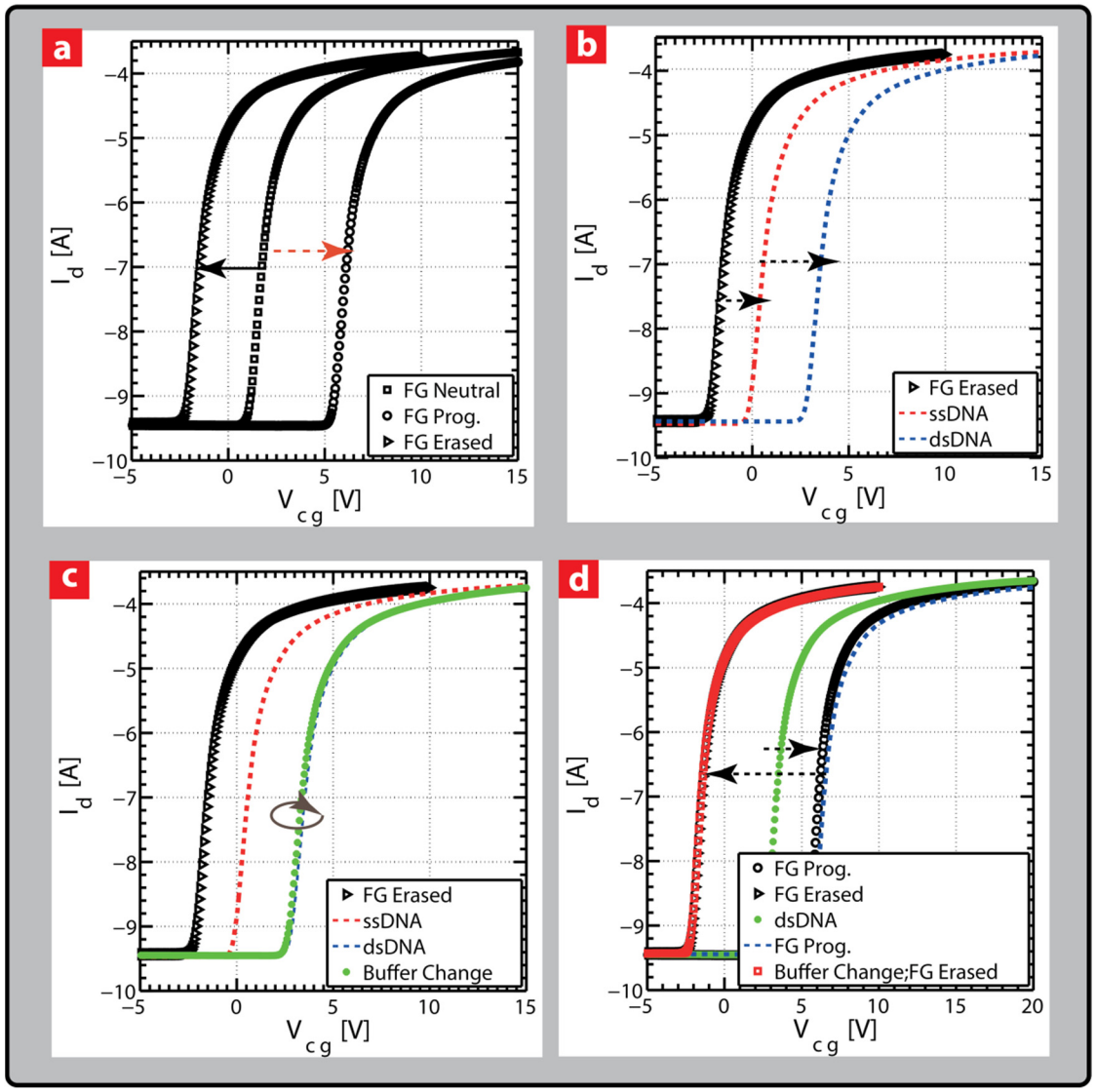

Figure 9. (a) The CvMOS with a poly-l-lysine-coated sensing gate is exposed to buffer and subsequent tunneling operations are performed. Red (dotted) arrow indicates programming while the black (solid) arrow indicates erase. (b) DNA strands C1 and C2 are added to the chip under the erased conditions (electron tunneled out) which results in marked V_{th_CG} shifts (c) buffer exchange after step (b) indicates an unchanged surface state. (d) Programming (electron tunneled in) the device after step (c) indicates the SG surface state is now similar to when pure buffer was present. Subsequent buffer exchange and erasing creates a refreshed interface.

Complete V_{th_CG} recovery was obtained only with electron injection and buffer

exchange. This suggested that injection manipulated and weakened the DNA surface interaction, allowing complete desorption during the buffer replacement. However without buffer exchange, DNA would be re-adsorbed.

During the initial rising CG pulse, V_{FG} increases and after 10ms significant amount of electrons begin to tunnel onto the FG. This electron accumulation in turn reduces V_{FG} (i.e. a negative feedback). When the CG and reference electrode are momentarily open circuited prior to readout, V_{FG} is highly negative and strongly couples to the SG as previously mentioned. DNA is then strongly manipulated, i.e. DNA manipulation possibly occurred even before a steady state condition (readout) was reached. This is in line with results by Rant et al. [18]. Figures 8&9 hence suggest that under $+E_{SG\_OX}$ conditions, DNA is attracted towards the surface but after FG programming the DNA desorbs as it interacts with the stored electrons. The dynamics of manipulation during and just after the tunneling operation is still actively being resolved.

B. The DNA transistor interface model

In order to corroborate the potential shifts and understand the true nature of the observed signals, we simulated the DNA interface stack [Fig. 10(a)] using the following approach. The total charge density within the DNA membrane is given by $\rho_{DNA} + \rho_{ions}$, where ρ_{ions} is a function of ψ. The total screening charge in the DNA membrane is then given by

$$\frac{d^2\psi}{dx^2} = -(\frac{\rho_{DNA} + \rho_{ions}(\psi)}{\varepsilon_{eff}}) \qquad (4)$$

where ρ_{DNA} is a constant background charge , i.e. similar to how dopants in a semiconductor are treated. Ions are mobile and are akin to electrons and holes.

We reformulate (4) into the form

$$\int_{E_O}^{E_{\beta 1}} EdE = -\frac{1}{\varepsilon_{eff}} \rho_{DNA}(\psi_\beta - \psi_O) - \frac{1}{\varepsilon_{eff}} \int_{\psi_O}^{\psi_\beta} \rho_{ions}(\psi) d\psi \qquad (5)$$

Here ε_{eff} is the effective permittivity of the DNA membrane and the subscript β represents the boundary between the DNA and bulk electrolyte presented in Fig. 10(b). E_O represents the field in the DNA membrane at the oxide interface such that it satisfies the condition $\varepsilon_{OX} E_{OX} = \varepsilon_{eff} E_O$. A Stern layer has not been assumed in the present simulation. Similarly the region from the DNA membrane into the bulk shown in Fig. 10(b) is re-formulated as

$$\int_{E_{\beta 2}}^{0} EdE = -\frac{1}{\varepsilon} \int_{\psi_\beta}^{0} \rho_{ions}(\psi) d\psi \qquad (6)$$

where $\varepsilon_{eff} E_{\beta 1} = \varepsilon E_{\beta 2}$ across the DNA electrolyte interface as a discontinuity in the E-field would exist due to the differences in permittivity. Here ε is the dielectric constant of water and $E_{\beta 2}$ represents the field condition in the electrolyte across the DNA membrane. Combing Eq. (5) and Eq. (6), we get

$$\int_{E_O}^{E_{\beta 1}} EdE + \int_{E_{\beta 2}}^{0} EdE = -\frac{1}{\varepsilon_{eff}} \rho_{DNA}(\psi_\beta - \psi) - \frac{1}{\varepsilon_{eff}} \int_{\psi_O}^{\psi_\beta} \rho_{ions}(\psi) d\psi - \frac{1}{\varepsilon} \int_{\psi_\beta}^{0} \rho_{ions}(\psi) d\psi \qquad (7)$$

In order to describe the physical mechanisms of signal generation when DNA adsorbs

to the surface of the transistor we examine two approaches. In the first approach using Eq. (7) the screening models inside and outside the membrane are treated differently while permittivities are the same i.e. $\varepsilon_{eff} = \varepsilon$ throughout. We compare the Debye-Huckel (DH) in Eq. (8) and Poisson-Boltzmann (PB) in Eq. (9) formulations both inside and outside the membrane and solve Eq. (7) self consistently in a background DNA volume charge density of $\sim 5\frac{C}{cm^3}$, as shown in Fig. 10(c). In the second approach we examine the critical role of varying ε_{eff} within the PB framework inside the membrane given the same DNA volume charge density.

$$E\frac{dE}{d\psi} = \frac{2en_O}{\varepsilon_{eff}}\left(\frac{e\psi}{kT}\right) \qquad \text{: Debye-Huckel (DH)} \qquad (8)$$

$$E\frac{dE}{d\psi} = \frac{2en_O}{\varepsilon_{eff}}\sinh\left(\frac{e\psi}{kT}\right) \qquad \text{: Poisson Boltzmann (PB)} \qquad (9)$$

We begin the discussion by first considering the effect of different ion screening profiles in the DNA layer. We find that when the DH approximation is used within the membrane $\Delta\psi_O$ varies a lot more in comparison to the PB model [Fig. 10(c)]. This essentially stems from the strong nonlinear screening property imposed by the PB approximation. In principle, one could reason the use of either approximation by understanding the respective constraints. The PB model treats ions as a continuous quantity and overestimates the screening charge. If close packing of DNA does occur, which is common at μM concentrations, the volume occupied by DNA is roughly estimated to be two-thirds of the total available volume within the layer [34]. The presence of a large ion density within the membrane is thus energetically unfavorable.

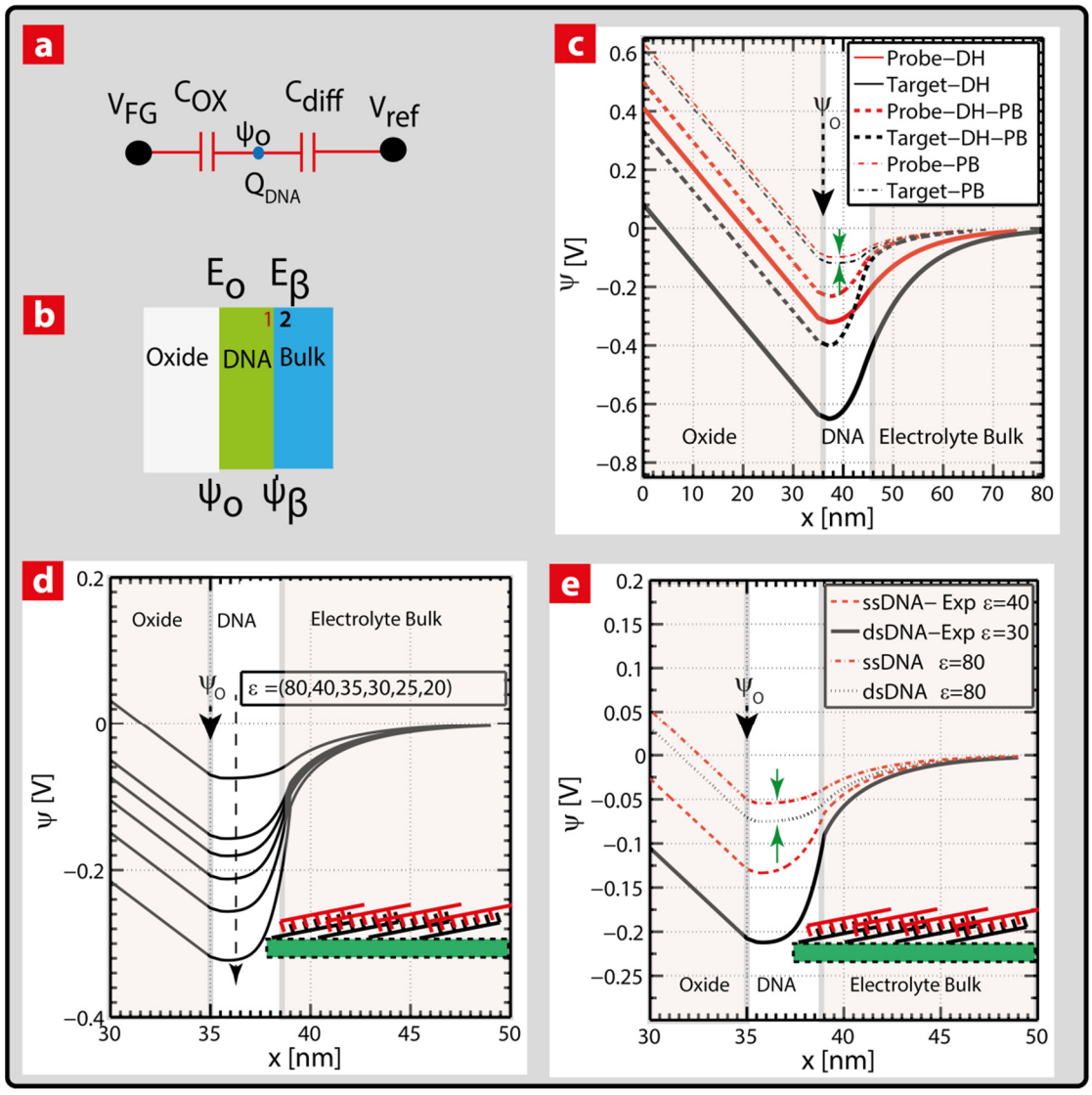

Figure 10. (a) Simplified capacitive model representing the FG-DNA interface (b) DNA-SG model representing the various interfaces, potentials and fields. ψ_O, ψ_β represent the potentials at the SG interface and DNA-electrolyte interface respectively. E_O and E_β are the respective fields across the SG interface and DNA electrolyte interface respectively. The numbers 1and2 represent the discontinuity in E-field across the DNA electrolyte interface due to permittivity differences (c) Potential profile across the capacitive network shown in (a) for various ionic screening models within the DNA membrane. Debye Huckel (DH) screening represents the linearized Poisson Boltzmann (PB) approximation. Notice that when ionic screening within and outside the membrane is both low, the ψ_O shift is maximum. The nonlinear PB approximation results in a much lower shift in ψ_O. (d) Potential profile including the partition energy barrier to account for the ion charge density within the DNA membrane. The self energy of ions (ΔG_m) is lowered in the DNA membrane represented by varying ε_{eff}. This leads to a lower charge density within the DNA membrane and larger change in ψ_O. The

inset depicts the orientation of DNA considered in the simulation. (e) Comparison of ($\Delta\psi_O$) hybridization signals between a PB approximation with $\varepsilon_{eff} = 80$ and an approximate ε_{eff} extracted for CG driven experimental data. Experimental evidence indicates tight packing of DNA at the surface resulting in ion exclusion and a more pronounced ψ_O shift.

This necessarily implies a low ion screening within the DNA membrane which can be mathematically treated via the DH approximation. This line of thinking is similar to inference by Wong et al. [34] where they found the best agreement to experimental hybridization data to occur when counterions were completely excluded from the DNA membrane. We do point out that when DNA molecules are loosely packed and the Donnan potential fully forms, the use of the DH approximation is incorrect and the PB approximation should be employed instead. Using a DH approximation outside the membrane is theoretically incorrect but is shown here only for intuitive purposes. Both Windbacher et al. [41] and Heitzinger et al. [42] recently proposed a linearized PB approach to tackle such screening effects similar to the DH approximation. The combination of DH inside the membrane (weak ionic screening) and PB outside (strong screening) matches closest to experiment. The use of positive electric fields can only amplify this effect [34]. Field induced counterion descreening causes more of the DNA charge to be "exposed" to form a depletion zone (i.e. a region devoid of movable ions with a background DNA charge). The depletion region would increase the built-in voltage , which in this case is the "Donnan potential" [30]. This hypothesis strongly supports both our and previous experiments, where unexpectedly large ψ_O shifts have been observed [1, 40]. Treating the charge inside the membrane using the DH model provides an intuitive understanding of how ψ_O varies when the membrane

is poorly screened, but this is a brute force method to account for ψ_O variations and raises the question as to what physical mechanism causes a lower screening?

Liu and Dutton [32] treated the ionic screening inside the DNA membrane using a partition energy (ΔG_m) formulation with the PB approximation. In Fig. 10(d) the potential profile is plotted for different ε_{eff} values. An energy cost is incurred when ions diffuse from the electrolyte with a higher permittivity into the DNA membrane with a lower permittivity. This partition effect primarily stems from the Born charge-dielectric interaction [32]. For the overall energy to be a minimum, a low counterion charge within the DNA membrane is required. The low ionic charge density directly translates to a lower screening within the DNA membrane. The self energy of the ion transferred from a medium of low dielectric constant to one of high dielectric constant is treated via the following relation [43];

$$\Delta G_m = -\frac{69z^2}{a}\left(\frac{1}{\varepsilon_{eff}} - \frac{1}{\varepsilon_{medium}}\right) * 0.01036eV \qquad (10)$$

Here a is the ion radius and z is the valency. For $a = 1.1\,\text{Å}$, $z = 1$, $\varepsilon_{medium} = 80$ and $\varepsilon_{eff} = 20$, we find $\Delta G_m = -0.243eV$.

Ion hydration and polarization effects at the SG interface have not been considered here, but as recently discussed by Fromherz [44], such effects can further riddle the measured ψ_O. A large negative ΔG_m implies a lower ion charge density within the DNA membrane as it is energetically favorable and hence less screening. Such effects have been considered to be orientation dependent and are stronger with the strands

parallel to the SG interface [32, 45] and/or tightly packed [34]. This leads to a qualitatively similar result to the DH model but is mathematically more robust. From the measurements presented in Fig. 8 and Fig. 9 for CG driven sensing, we extracted a $\varepsilon_{eff} \sim 40$ when ssDNA immobilizes ($\Delta\psi_O \sim 150mV$) and an additional decrement to $\varepsilon_{eff} \sim 30$ when hybridization occurs ($\Delta\psi_O \sim 70mV$) [Fig. 10(e)], assuming the strands lie parallel to the surface [inset Fig. 10(d&e)]. This is a reasonable approximation as the lysine-DNA interaction is purely electrostatic in nature. It is clear from both approaches that the net screening within the membrane severely affects the measured ψ_O. If one does not consider the drop in ε_{eff}, the difference in the hybridization signal drops down to ~20mV as shown in Fig. 10(e). Since a significant fraction of experimental observations in relation to DNA hybridization indicate $\Delta\psi_O$ values in the 40-120mV range and as such can only be justified by either weak screening or ion exclusion from the membrane, we believe that the major factor determining ion exclusion is the partition effect and the Born charge-dielectric interaction is an important source of ΔG_m. Nevertheless, a clear relation between ΔG_m and the E-field is still lacking and is currently work in progress.

C. On dual gate operation and ψ_O amplification

We observed CG driven (Fig. 8 & Fig. 9) ψ_O shifts of $\sim 120-300mV$ upon ssDNA addition and a further $\sim 100mV$ shift upon hybridization. Conventional GCS theory [3] cannot account for such large ψ_O shifts due to strong nonlinear screening. From

measurements presented earlier we extract an average charge density of $\sim 0.04\frac{C}{m^2}$ (immobilized ssDNA) and a subsequent $\sim 0.02\frac{C}{m^2}$ during hybridization. With traditional ISFET's [3, 37, 40] however, DNA adsorption and hybridization normally reveal ψ_O shifts of $\sim 40mV$ and $\sim 5-20mV$, respectively. The plausible reasons for such differences are as follows.

(i) ψ_O, although influenced by the Donnan potential, also depends on the surface pH response, since a pure Nernstian response would effectively screen any membrane charge from the FG [29] . The pH response of the CvMOS is extremely non-Nernstian with and without a PLL coating and pH_{PZC} was found to be closer to pH 9 (not shown). The PLL coating in addition neutralizes most of the surface charge and also makes it slightly positive resulting in a non-monotonic and weak pH response especially around pH_{PZC} (low N_S in Part I). This can enhance the Donnan effect, and thereby lead to larger surface potential [27].

(ii) The Born charge dielectric function can play a significant role in amplifying the ψ_O shift.

(iii) The high surface charge of $0.8\frac{C}{m^2}$ normally used for SiO_2 [3] is orders of magnitude higher than the surface charge density observed in this study $8\frac{mC}{m^2}$ (see part I) for polysilicon with and without PLL. Such high sheet

charge densities can lead to high negative ψ_O potentials, screen out most of the DNA charge and often interfere with DNA immobilization affecting the Donnan equilibrium and orientation.

(iv) Majority of ISFET sensors use a constant readout current when monitoring DNA binding and hybridization. This implies a constant field across the gate oxide between the 2D electron/hole gas in the channel and the reference electrode. In the CvMOS due to the different E_{SG_OX} conditions when driven from the CG, ψ_O can vary by a few $(\sim \frac{KT}{e})$. This can influence DNA immobilization due to Coulombic interactions [46], resulting in counterion descreening and re-orientation on the surface [18, 42]. Interfacial polarization [44] can cause further modulation.

Using the circuit representation shown in Fig. 10(a), we can additionally show that the change in ψ_O differ in the three measurement conditions.

$$\Delta\psi_O = \frac{\Delta Q}{C_{SG} + C_{diff}} \qquad (11)$$

when V_{REF} is grounded and the CG is driven. On the other hand,

$$\Delta\psi_O = \frac{\Delta Q}{C_{diff}} \qquad (12)$$

when V_{REF} is driven and the CG is grounded. In the case when V_{REF} is floating, the change in ψ_O can be written as

$$\Delta\psi_O = \frac{\Delta Q}{C_{SG}} \qquad (13)$$

One readily notices that the readout mechanism can severely affect the measured ψ_O. For example, CG and V_{REF} readouts are dominated by the diffusive capacitance. Equations (11) and (12) seemingly imply that V_{REF} readout would always result in a slightly higher $\Delta\psi_O$. However, $Q_{DNA} + Q_{ions}$ which makes up ΔQ, can be different under different E_{SG_OX}, which can arise when V_{th} is measured from the reference electrode as opposed to CG. Hence, by appropriate sizing of the CG and SG areas, the sensitivity to DNA detection can be maximized by engineering the ΔQ dependence on E-field. Additionally when V_{REF} is floating [Eq. (13)], $\Delta\psi_O$ can swing (~150mV) a lot more [Fig. 10(b)] in comparison to when V_{REF} is pinned (~70mV) [Fig. 8] primarily because the screening capacitance of the ionic diffuse layer is much lower. This suggests that the operation of the reference electrode needs more careful evaluation in order to achieve maximum sensitivity. Since the pH_{PZC} lies in between pH=7 and pH=9, when the FG is charge neutral and given evaporation was negligible during the course of experimentation, we strongly believe the enhancement in $\Delta\psi_O$ represented in Fig. 8 & Fig. 9 stems from the shift in Q_{ions} within the DNA membrane due to differences in E_{SG_OX}.

D. Impedance spectroscopy

In order to further validate DNA desorption upon charge injection, we performed impedance spectroscopy[24, 47], which probes the dielectric properties of the interface and is not dependent on surface potential and pH fluctuations[4]. This

test would help ascertain whether DNA truly desorbs as monitored by the interfacial impedance change.

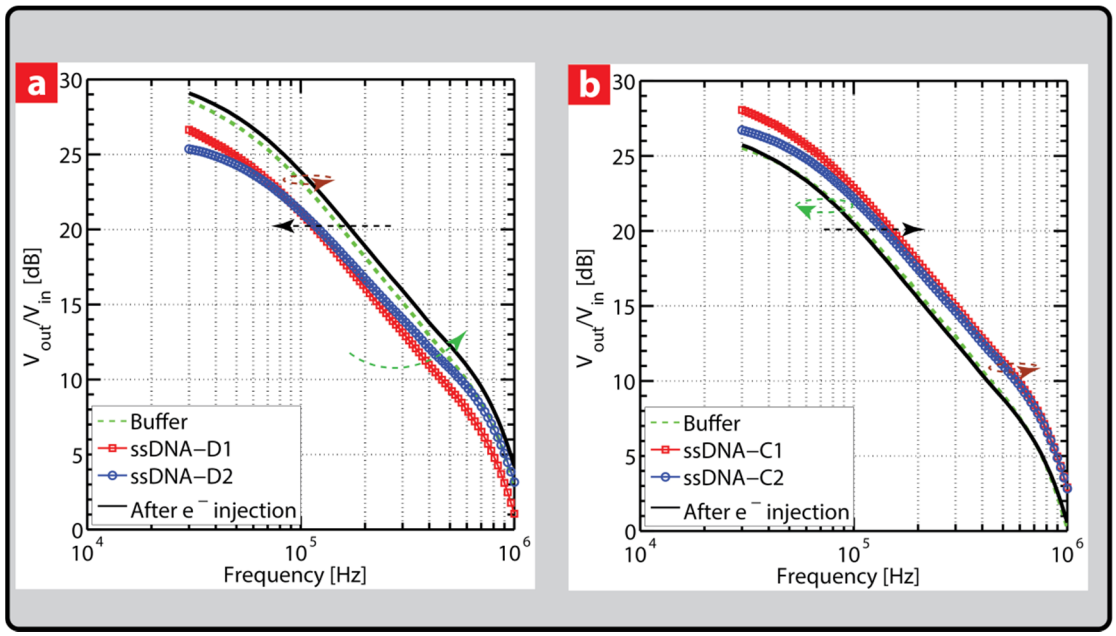

Figure 11. Impedance response before and after charge injection for two different lengths of DNA. (a) DNA strands D1 and D2 are added to the chip in sequence and the frequency response before and after hybridization is monitored. A clear relaxation is observed (Z_1) after hybridization , indicating dispersion mechanisms are possibly tied to the structure and stiffness of the DNA strand. Charge injection is shown to refresh the surface with a recovery of impedance. (b) Step (a) repeated for strands C1 and C2 showing the molecular weight dependence on the formation of Z_1 which is very weak. The initial shift in P_1 is attributed to shift in resistance due to an inefficient relaxation at extremely small molecular length scales.

By using the split-gate approach (*see methods*), the small-signal output is monitored through a lock-in amplifier. An important point is that the bandwidth is determined by the combined effect of the CνMOS gate stack and the parasitic FG to bulk capacitance, leading to a roll-off at approximately 300 KHz, well within the lock-in amplifier and TIA bandwidth. Recently [4, 37] the overall time constant of the Bode response was reported and also shown to be dependent on the contact-lane capacitance (~10nF) and electrolyte resistance, which results in the first pole at fairly low (~KHz)

frequencies. In the present study however the bandwidth of the overall response was limited by the external amplifier. The contact-lane capacitance consists of the source-drain contact line parasitics in parallel to the gate oxide capacitance. SPICE simulations with estimated parameters depict this behavior qualitatively (Appendix-B, Fig. 38). An increase in the interface capacitance would move Z_1 lower and increase the impedance. An increase in interfacial resistance would move P_1 lower with a higher time constant. Impedimetric responses presented in Fig. 11(a&b) were monitored for 2 different DNA lengths (24 and 48bP) (see Table 4, Appendix-B). The Bode response with only buffer was recorded and used as a baseline. Strand D1 immobilization revealed a net increase in the interfacial resistance (parallel shift in P_1). Upon complementary (D2) strand addition, P_1 was seen to move further in with the clear formation of Z_1, indicating relaxation of the adsorbed DNA film illustrated in Fig. 11(a). The reason we term it as relaxation is because the roll off in frequency does not follow the 20dB/decade drop as would be expected of a constant capacitance. This indicates that relaxation is frequency dependent. The DC operating point was adjusted to maintain a constant output current via CG feedback. The bandwidth of the TIA set a limit on the high frequency response which explains the rapid roll off close to 1MHz. Shorter 24bP DNA strands (C1) upon hybridization on the contrary showed an outward movement of P_1 [Fig. 11(b)], possibly indicating a decreased resistance with a very weak formation of Z_1, which is consistent with recent evidence [4]. A plausible explanation is that the counter-ion cloud around the DNA molecule has not yet undergone complete relaxation and can still respond to the applied frequency [48]. This affects the resistance and capacitance of DNA as the counter-ion cloud

effectively shields the signal. An interesting point is that the appreciable shift in Z_1 for the larger D1 and D2 strands occurs only when the oligonucleotides undergo hybridization. This seems to imply that the frequency-dependent nature of the relaxations are affected by the physical structure of the molecule since dsDNA is much more rigid than ssDNA [18, 33] and leads to a different relaxation mechanism.

Upon programming (*electron injection*) the FG, we observed a recovery of P_1 and Z_1 to their respective initial points of pure buffer. This is in agreement with the quasi-static analysis where a recovery of ψ_O was observed. Impedimetric spectroscopy using FET's at a constant operating point is immune to any drift in solution pH and reliably probes the dielectric properties and local molecular structure. The impedance technique could potentially be used to ascertain local interactions between DNA and proteins where charge and capacitance can be concomitantly detected, and serve as a versatile test bench in biophysical applications.

CONCLUDING REMARKS

We present sensing and dynamic manipulation of surface-immobilized DNA using the CvMOS. Quasi-static I-V and impedance spectroscopy measurements were performed. The measured ψ_O during DNA immobilization and hybridization was found to be E-field dependent. A positive E-field enhanced the hybridization and immobilization signal while a negative E-field reduced it. In addition dual-gate control and charge programmed onto the FG affected the sensitivity by inducing different field conditions in the SG oxide. Manipulation of the oligonucleotides was realized via non volatile

charge injection which set a defined repulsive/attractive field between the FG and solution. The ionic cloud and associated de-screening around DNA is believed to be responsible for this effect as it can be perturbed [30, 49] via the field effect. This was further corroborated by modeling the DNA membrane using modified screening and partition energy formulations. The modified permittivity due to the partition energy difference which could arise either due to orientation or ion specific exclusion effects was found to play a key role. Furthermore V_{th_CG} and ψ_O were observed to recover after DNA desorption aided by the non-covalent nature of the binding. Impedimetric detection using a split-gate approach showed a clear shift in the frequency response upon DNA immobilization (pole) and subsequent hybridization (pole and zero). Two different lengths were tested (24bp and 48bp) and the results indicate that the impedance recovers upon charge injection indicating surface recovery. The frequency response was also found to exhibit a molecular weight and structure dependence. Upon programming the FG with electrons, the interface impedance was observed to recover, indicating DNA desorption. This technique of combined detection and manipulation using CMOS compatible charge sensors can potentially help realize electrically addressable sensor arrays, refreshable bio-sensor interfaces and dynamic reconfiguration of protein complexes.

Supplemental Material: Supplementary material accompanies this chapter. Refer Appendix B for details.

REFERENCES

[1] L. Bandiera *et al.*, Biosens. Bioelectron. **22**, 2108 (2007).

[2] M. Barbaro, A. Bonfiglio, and L. Raffo, IEEE Trans. Electron Devices **53**, 158 (2006).

[3] J. Fritz *et al.*, Proc.Natl.Acad.Sci. U.S.A. **99**, 14142 (2002).

[4] R. GhoshMoulick *et al.*, Phys. Status. Solidi A **206**, 417 (2009).

[5] B. C. Jacquot *et al.*, Biosens. Bioelectron. **23**, 1503 (2008).

[6] E. Katz, and I. Willner, Electroanalysis **15**, 913 (2003).

[7] F. Uslu *et al.*, Biosens. Bioelectron. **19**, 1723 (2004).

[8] A. Star *et al.*, Proc.Natl.Acad.Sci. U.S.A. **103**, 921 (2006).

[9] G. Zheng *et al.*, Nat Biotech **23**, 1294 (2005).

[10] K. Jayant *et al.*, in *Proceedings of Solid-State Sensors, Actuators and Microsystems Conference, 2009*, pp. 1814.

[11] O. Knopfmacher *et al.*, Nano Lett. **10**, 2268 (2010).

[12] C. Baozhen, A. Parashar, and S. Pandey, IEEE Sens. J. **11**, 2906 (2011).

[13] P. Bergveld, Sens. Actuators, B **88**, 1 (2003).

[14] N. Y. M. Shen *et al.*, IEEE Trans. Electron Devices **50**, 2171 (2003).

[15] E. Stern *et al.*, Nature **445**, 519 (2007).

[16] A. Gao *et al.*, Nano Lett. **11**, 3974 (2011).

[17] Y. L. Bunimovich *et al.*, J. Am. Chem. Soc. **128**, 16323 (2006).

[18] U. Rant *et al.*, Biophys. J. **85**, 3858 (2003).

[19] M. Erdmann *et al.*, Nat Nano **5**, 154 (2010).

[20] I. Y. Wong, and N. A. Melosh, Nano Lett. **9**, 3521 (2009).

[21] F. Fixe *et al.*, Biosens. Bioelectron. **19**, 1591 (2004).

[22] B. Reddy, Jr. *et al.*, Anal. Chem. **83**, 888 (2011).

[23] A. Vainrub, and B. M. Pettitt, Phys.Rev.E **66**, 041905 (2002).

[24] A. B. Kharitonov *et al.*, J.Phys.Chem.B **105**, 4205 (2001).

[25] A. H. Talasaz *et al.*, Proc.Natl.Acad.Sci. U.S.A. **103**, 14773 (2006).

[26] D. Landheer *et al.*, J. Appl. Phys. **98**, 044701 (2005).

[27] D. Landheer *et al.*, IEEE Sens. J. **7**, 1233 (2007).

[28] R. B. M. Schasfoort *et al.*, Anal. Chim. Acta **238**, 323 (1990).

[29] J. Kruise *et al.*, Sens. Actuators, B **6**, 101 (1992).

[30] W. R. McKinnon, D. Landheer, and G. Aers, J. Appl. Phys. **104**, 124701 (2008).

[31] G. Shalev, Y. Rosenwaks, and I. Levy, Biosens. Bioelectron. **31**, 510 (2012).

[32] Y. Liu, and R. W. Dutton, J. Appl. Phys. **106**, 014701 (2009).

[33] W. Kaiser, and U. Rant, J. Am. Chem. Soc. **132**, 7935 (2010).

[34] I. Y. Wong, and N. A. Melosh, Biophys. J. **98**, 2954 (2010).

[35] A. B. Kharitonov *et al.*, J. Electroanal. Chem. **487**, 133 (2000).

[36] A. B. Kharitonov *et al.*, Sens. Actuators, B **70**, 222 (2000).

[37] S. Ingebrandt *et al.*, Biosens. Bioelectron. **22**, 2834 (2007).

[38] T. M. M. Squires, Robert J;Manalis, Scott R, Nat Biotech **26**, 417 (2008).

[39] X. T. Vu *et al.*, Sens. Actuators, B **144**, 354 (2010).

[40] A. Poghossian *et al.*, Sens. Actuators, B **111–112**, 470 (2005).

[41] T. Windbacher, V. Sverdlov, and S. Selberherr, in *Proceedings of 13th*

International Workshop on Computational Electronics, IWCE 2009, pp. 1.

[42] C. Heitzinger *et al.*, Journal of Computational and Theoretical Nanoscience **7**, 2574 (2010).

[43] J. Israelachvilli, *Intermolecular & Surface Forces* (Academic Press, London, 1992).

[44] P. Fromherz, Phys. Status. Solidi A **209**, 1157 (2012).

[45] M. Denhoff, and D. Landheer, ECS Transactions **35**, 17 (2011).

[46] Z. Jiang, and D. Stein, Langmuir **26**, 8161 (2010).

[47] M. M. G. Antonisse *et al.*, Anal. Chem. **72**, 343 (1999).

[48] S. Takashima, Biopolymers **5**, 899 (1967).

[49] Y. Liu *et al.*, Appl. Phys. Lett. **97**, 143109 (2010).

[50] See Appendix B for additional details of the instrumentation set up, control experiments for DNA hybridization and Simulation of the DNA transistor impedance model. Tables outlining the oligonucleotides used and equation set describing the working of the *CυMOS* transistor are also included.

CHAPTER 4- PROGRAMMABLE ION-SENSITVE TRANSISTOR INTERFACES: DESIGN CONSIDERATIONS, SIGNAL GENERATION AND SENSITIVITY ENHANCEMENT

CHAPTER OVERVIEW

We report on factors that affect DNA hybridization detection using ion-sensitive transistors (ISFET's). Signal generation at the interface between the transistor and immobilized biomolecules is widely ascribed to unscreened molecular charges causing a shift in surface potential which directly affects the transistor output current. Traditionally, the interaction between DNA and the dielectric or metal sensing interface is modeled by treating the molecular layer as a charge sheet and the ionic profile with a Poisson Boltzmann (PB) distribution. The surface potential under this scenario is described by the Graham equation. This approximation however, often fails to explain large hybridization signals on the order of tens of mV's. More realistic descriptions of the DNA-transistor interface which include factors such as ion permeation, exclusion and packing constraints have been proposed with little or no corroboration against experimental findings. In this study, we examine such physical models by their assumptions, range of validity, and limitations. We compare

simulations against experiments performed on electrolyte-oxide-semiconductor capacitors (EOS) and foundry-ready floating-gate ISFET's. We find that with weakly charged interfaces (i.e., low intrinsic interface charge), pertinent to the surfaces used in this study, the best agreement between theory and experiment exists when ions are completely excluded from the DNA layer. The influence of various factors such as bulk pH, background salinity, chemical reactivity of surface groups, target molecule concentration and surface coatings on signal generation is studied. Furthermore, in order to overcome Debye screening limited detection, we suggest two signal enhancement strategies. We first describe frequency domain biosensing, highlighting the ability to sort short DNA strands based on molecular length, and then describe DNA biosensing in multi-electrolytes comprising of trace amounts of higher-valency salt in a background of monovalent saline. Our study provides guidelines for optimized interface design, signal enhancement and the interpretation of FET-based biosensor signals.

INTRODUCTION

Development of label-free electronic detectors for DNA molecules is central to applications ranging from biosensing, sequencing and diagnostics. The use of ion-sensitive field-effect transistors (ISFET's) for electrochemical detection of biomolecules [1-6] provides a fast and sensitive signal transducing scheme applicable across a wide range of target concentrations (fM to μM sensitivity) [7, 8]. Detection is conventionally sought through direct molecular charge transduction [4]. The

commonly accepted notion of signal generation is that intrinsic molecular charges immobilized on the open oxide interface modulate the net surface charge (σ_O) and set a new equilibrium surface potential (ψ_O). In order to theoretically corroborate experimental observations, the updated σ_O and ψ_O conditions are calculated using the Poisson-Boltzmann (PB) approximation described by the Grahame equation [Eq. 1].

$$\sigma_O = \sqrt{8\varepsilon_{liq} kTn_o}\,\sinh\left(\frac{ze\psi_O}{2kT}\right) \qquad (1)$$

Here ε_{liq} is the absolute permittivity, z is the valency, n_o is the electrolyte ion concentration, k is the Boltzmann constant and T is the temperature. The difference in ψ_O before and after DNA addition is then:

$$\Delta\psi_O = \frac{2kT}{ze}\arcsin h\left(\frac{\sigma_O + \sigma_{DNA}}{\sqrt{8\varepsilon_{liq} kTn_o}}\right) - \frac{2kT}{ze}\arcsin h\left(\frac{\sigma_O}{\sqrt{8\varepsilon_{liq} kTn_o}}\right) \qquad (2)$$

This method of signal interpretation assumes that DNA is akin to a sheet charge. The strong non-linear screening imposed by the PB formulation "mathematically" does not allow ψ_O to rise too high, especially under high σ_O conditions. Fritz and colleagues [4] corroborated their experimental observations against the standard Grahame equation and showed that an intrinsic surface charge density of 0.8C/m^2, corresponds to a $\Delta\psi_O$ (i.e., surface potential shifts during hybridization) of 3mV. While the Grahame equation corroborates $\Delta\psi_O$ observed on thermally grown pristine oxides, it fails to account for large $\Delta\psi_O$ shifts often encountered in experiments involving non-traditional surfaces [9]. For example, $\Delta\psi_O$ ranging between 3mV to 800mV-1V [9]

have been reported for a variety of interfaces. It is important to note that DNA is always accompanied by counterions and often forms a layer of finite thickness at the transistor interface. It thus becomes imperative to consider both layer thickness and different screening properties within these molecular layers to validate experimental observations. Recent reports that have considered screening properties within DNA layers, attribute the mechanisms of signal generation to either ion exclusion, formation of a Donnan membrane potential or differences in permittivity [10-17] between the DNA and electrolyte phase. Most of these studies have been theoretical in nature with very little experimental corroboration. It is still unclear as to how properties such as the surface pH response (Nernstian vs. Non-Nernstian), E-field dependent surface ionizability and electrolyte composition affect signal generation and whether such membrane theories corroborate experimental findings. Questions that still remain to be answered are i) What combination of physical effects accurately explain the large deviation from theory? and ii) how can optimal sensitivity be established? We first discuss some of the physical effects below.

The first critical aspect to DNA sensing is the nature of the interface and its net intrinsic charge [4]. Studies have shown very low hybridization signals on surfaces exhibiting high intrinsic surface charge, while metal interfaces [9] or weakly charged poly-silicon [15] surfaces have revealed large signal shifts of ~50-100 mV. A direct comparison under identical conditions would help narrow the differences. Furthermore, the difference is generally attributed to molecular charge screening by surface groups. However, surface groups are ionized as a function of pH and electric

field [18]. So this raises the question, if DNA is charged, should it not shift the surface chemical equilibrium and affect the ionizability of the surface groups?

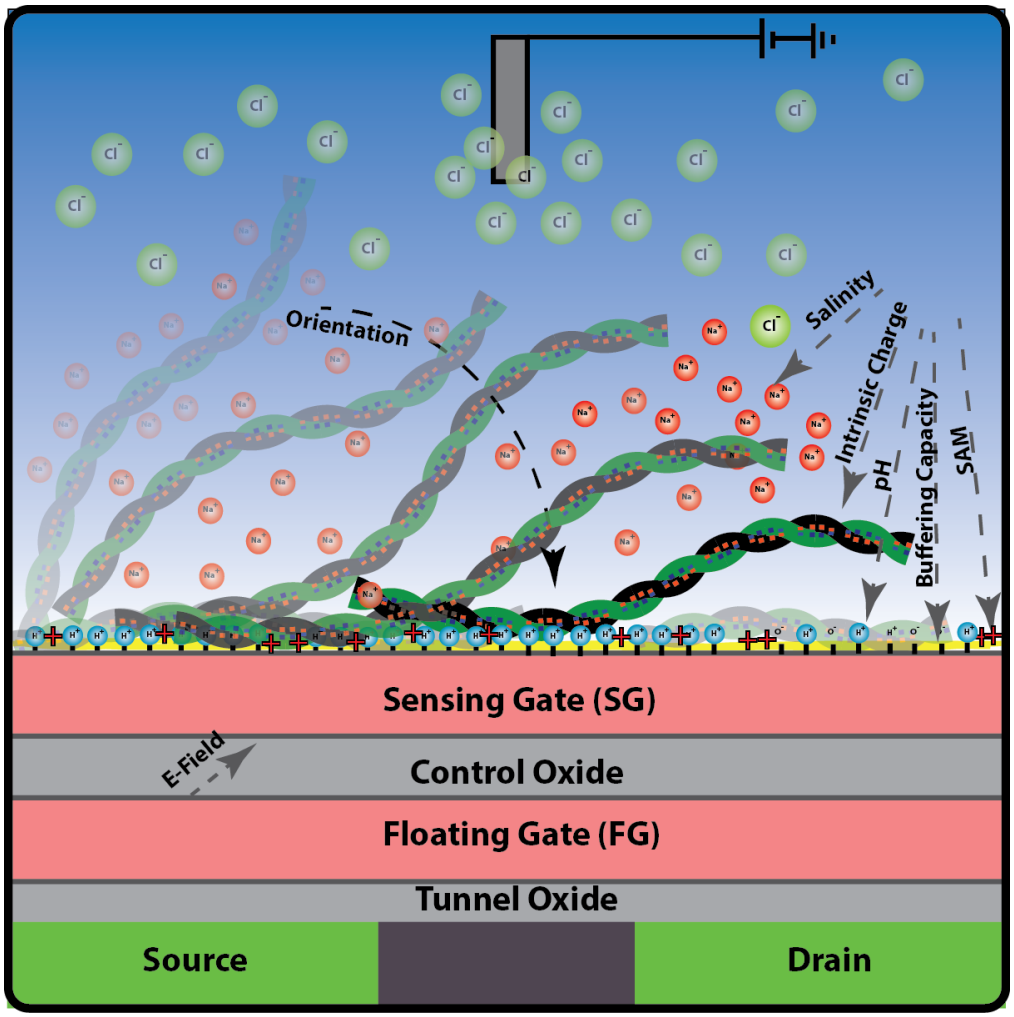

Figure 12: Various factors that affect DNA detection and underlie signal generation at the SG interface. The E-field in the SG oxide is tuned by either modulating the control gate (not shown) bias or FG charge.

An important concern that is often raised with FET-based sensing is Debye screening [Eq. 3]. Ionic screening of molecular charges characterized by the Debye length is dependent only on the overall saline concentrations.

$$\lambda_D = \sqrt{\frac{\varepsilon_{liq} kT}{2e^2 z^2 n_o}} \qquad (3)$$

Debye screening lengths (λ_D) decrease as global saline concentrations increase, thus effectively shielding DNA charges from the transistor surface. In addition to anions and cations, bulk pH (pH_B) can also play an important role with respect to screening [19, 20]. Recently it was shown that as pH_B was lowered the DNA packing and hybridization efficiency increased, thereby increasing the deflection of a nano-mechanical beam [21]. This was an important result as it implied that by lowering pH_B inter-strand repulsion could be lowered which resulted in an increase in hybridization efficiency. Furthermore, pH_B can also tune the net surface charge and hence ψ_O [18]. Such a change in ψ_O can affect DNA binding, surface ion concentration and molecular orientation [15]. Hence elucidating the role of pH_B on DNA interactions at the transistor interface is paramount.

A parameter of interest within the screening framework is the role of permittivity within tightly packed molecular layers. Such effects have often been neglected in corroborating experimental data. Studies however have shown that there exists a gradient in permittivity which extends from the membrane-electrolyte interface into the bulk [22]. Recently, we showed that in order to match large experimentally observed hybridization signals of the ~50-60mV, it was required to account for such permittivity differences [15], since lowering the molecular layer permittivity would result in pronounced ion exclusion and in turn lower screening. While such a

hypothesis agreed more or less with experiment, the validity of such a model across different pH_B conditions was not discussed. In this study we further shed light on this particular aspect.

Addition of a surface monolayer (SAM) such as poly-L-Lysine (PLL) or APTES to chemically functionalize the interface facilitates molecular binding, but can further riddle the observed signal. So far, most studies have focused on molecule orientation and linker chemistries [23]. However, the intrinsic pH response of the SAM interface is often ignored. As previously mentioned the intrinsic charges on DNA could shift the surface chemical equilibrium and appear as an applied E-field. Hence it becomes important to understand how SAM's affect the intrinsic pH sensitivity, and under what condition can such models can be ignored.

The target concentration also plays an important role in deciding hybridization efficiency [24]. A large target concentration can lead to steric hindrance and repulsion between incoming target strands, and thus hinder the diffusion towards the immobilized probe layer. Such blockage prevents efficient hybridization and can lower the readout signal. In this work, we discuss the implications of adding large target concentrations and also present evidence of how surface heterogeneity can affect binding isotherms [3, 11, 25].

As salinity, pH_B, membrane screening, probe/target density, and surface charge all have effects on signal generation and sensitivity, tuning each parameter for optimal signal enhancement becomes daunting. For example, studies have proposed that in order to improve hybridization efficiency one could tune the global saline levels [26],

where hybridization is performed in high saline concentrations and readout under low saline conditions. While changing salinity levels between hybridization and readout seems attractive and can be readily achieved with microfluidic integration, a shift in global saline levels can change the buffering response of surface hydroxyl groups [18, 27], which can further complicate the interpretation of the recorded signal. Another attractive approach adopted by researchers is the combination of DNA amplification and pH or ion sensitivity [28, 29]. Although these techniques are promising, the use of enzymes for amplification makes it hard for long-term storage and handling of reagents. In order to circumvent such difficulties so that ISFET operation is possible under high saline conditions, we present two alternatives to enhance the recorded signal. The first alternative employs frequency-mode operation which probes the dielectric and resistive properties of the molecular layer, and the second deals with performing hybridization operations in the presence of trace levels of multivalent salt. With the former we present length sorting of short dsDNA, and with the latter we discuss the implications of DNA condensation [30] and localized screening modulation as a method to improve DNA biosensing.

METHODS

A. Materials

EOS capacitors and floating-gate ISFET's termed the CvMOS were fabricated as described previously [18]. The capacitors were fabricated on p-type silicon wafers with highly doped polysilicon and SiO_2 interfaces exposed to the electrolyte. A nitride

passivation was added to reduce ion drift. An epoxy reservoir avoids the fluid from reaching the bond pads and provides electrical isolation. The CvMOS transistors [Fig. 12] were fabricated in an $1.5\mu m$ AMI foundry process [18, 31]. Briefly, the tunnel oxide refers to the oxide between the channel and the floating gate (FG), while the control oxides represent the oxide between the control/sensing gates (CG/SG) and FG. The FG is electrically floating. The reference electrode pins the electrolyte bulk to (V_{REF}) while the CG can be used to program, erase or bias the device to a desired region of operation. The tunnel and control oxide thicknesses are 10nm and 35nm, respectively. The control gate area is $25\mu m \times 40\mu m$ while sensing gates vary between $5\mu m \times 400\mu m$ and $200\mu m \times 400\mu m$. The chip was cleaned with DI water, isopropyl-alcohol (IPA) and coated with PLL before each test. The chips were subsequently set aside for two hours washed with DI water, dried and stored at 4ºC before use. A small reservoir made of epoxy was created to isolate the fluid from the bond pads.

Single and complementary strands of DNA of varying lengths (16 (B1,B2), 25 (C1,C2) and 48bp (D1,D2)) (see Table 1) were procured from IDT DNA and 99.9% HPLC purified. DNA was maintained in buffer (10mM TRIS pH 8, 1mM NaCl and 1mM EDTA) at a stock concentration of 100μM and was diluted to desired concentrations when required. Higher saline concentrations (150mM) were used when testing for Debye screening limited responses. Electrolytes containing $NaCl$, $MgCl_2$ and $Co(NH_3)_6Cl_3$ salts (Sigma Aldrich) were made up to the desired dilution using Millipore de-ionized H_2O. When testing the role of multivalent ions during DNA hybridization, DNA was suspended in buffer without EDTA, just so as to avoid

competition with multivalent ions. $Ag/AgCl$ (Warner instruments, USA) pseudo reference electrodes were used. The wire surfaces were cleaned with sand paper and chlorinated in bleach prior to every experiment. Experiments were performed in a light-tight environment.

Table 1: DNA strand sequences and associated lengths used for experimental runs.

Type	DNA sequence
B1 (16bP ssDNA) probe	5'-GCTCAAAGTCTCGCAG-3’
B2 (16bP ssDNA) target	5'- CTGCGAGACTTTGAGC-3’
C1 (25bP ssDNA) probe	5’-GCATCTGGGCTATAAAAGGGCGTCG-3’
C2 (25bP ssDNA) target	5’-CGACGCCCTTTTATAGCCCAGATGC-3’
D1 (48bP ssDNA) probe	5’-GCATCTGGGCTATAAAAGGGCGTCGGTATCCAAGGTTCCGGATACGAG-3’
D2 (48bP ssDNA) target	5’-CTCGTATCCGGAACCTTGGATACCGACGCCCTTTTATAGCCCAGATGC-3’

The different DNA strands were additionally used under identical conditions to ascertain the impedance dependence on molecular length before and after hybridization.

B. Electrical instrumentation

Capacitance-voltage (CV) measurements were performed using a Keithley 4200 semiconductor parameter analyzer. CV profiles were recorded at various small-signal frequencies. The reference electrode was supplied with an AC signal superimposed on a slow DC sweep, while the wafer chuck was used as ground. The transistor transfer characteristics (the drain current I_D vs. the CG bias (V_{CG})) were recorded using a Keithley 236 source measure unit (SMU) for the drain ($V_D = 1V$) and a Keithley 2400 was used to sweep V_{CG}. Prior to adding DNA, the transconductance (g_m) seen from both the CG and SG was recorded in order to calibrate the capacitance ratio [18]. In addition to IV analysis, impedance measurements were performed by monitoring the small-signal transistor gain as a function of frequency as previously described [15, 32]. Briefly, a single-toned sinusoid waveform was applied (Stanford Research Systems DS345, CA, USA) through the Ag/AgCl reference electrode while the DC bias was supplied via the control gate independently (Keithley 2400, USA). The output current of the transistor was fed to a lock-in amplifier (Stanford Research Systems, SR844, CA, USA) through a Transimpedance amplifier (TIA) (SR 570, Stanford Research, USA). Bode responses and current/voltage (I/V) sweeps were measured intermittently to ascertain the operating point stability. The CG was then adaptively biased to maintain a constant operating point during the impedance

measurement. UV spectrophotometry (Shimadzu UV 3600, USA) was used to ascertain the absorbance of non-precipitated DNA during multivalent ion treatment.

C. Device Operation

The CvMOS [Fig. 12] working principle is similar to what was previously outlined [15, 18]. The transistor was operated in both quasi-static and AC impedance mode. Briefly, the floating gate potential (V_{FG}) is perturbed by analyte adsorption on the SG surface. A change in V_{FG} directly affects the readout current [Eq. 4].

$$I_D = \frac{\mu C_{tun} W}{2L}(V_{FG} - V_{th\_FG})^2 \qquad (4)$$

where I_D is the drain current in saturation , μ is the mobility, C_{tun} the tunnel oxide capacitance, W the channel width, L the length, and V_{th_FG} the threshold voltage seen from the FG.

A V_{CG} sweep is then performed to determine V_{th_CG} is the threshold voltage seen from the CG and is defined when the drain current reaches $1\mu A$ which ensures that V_{FG} is constant [Eq. 5].

$$V_{FG} = \frac{Q}{C_T} + \frac{C_{gs}}{C_T}V_S + \frac{C_{gd}}{C_T}V_D + \frac{C_{CG}}{C_T}V_{CG} + \frac{C_{SG}}{C_T}(\psi_O - V_{REF}) \qquad (5)$$

where Q is the charge stored on the FG, C_{gs} is the gate to source capacitance, C_{gd} the gate to drain capacitance, C_{CG} the control gate interpoly oxide capacitance, C_{SG} the sensing gate interpoly oxide capacitance and C_T the total capacitance [Eq. 6] seen by the FG. V_{CG} is the voltage applied at the CG to bias the device while V_{SG} is determined

by ψ_O and V_{REF}.

$$C_T = (\frac{C_{tun} \times C_{dep}}{C_{tun} + C_{dep}}) + C_b + C_{gs} + C_{gd} + C_{CG} + C_{SG} \qquad (6)$$

Here C_{dep} is the depletion layer capacitance and C_b the FG to bulk capacitance. As highlighted previously [18], V_{CG} driven readout results in an amplified measure of ψ_O and the amplification factor A_C is primarily determined by the ratio between the two input capacitors C_{SG} and C_{CG} [Eq. 7].

$$A_C = \frac{\frac{W_{SG} L_{SG} \cdot \varepsilon_{ox}}{t_{ox}} // C_{dl}}{\frac{W_{CG} L_{CG} \cdot \varepsilon_{ox}}{t_{ox}}} \qquad (7)$$

where $W_{CG} \cdot L_{CG}$ and $W_{SG} \cdot L_{SG}$ are the layout areas of the CG and SG, respectively.

$$\Delta V_{th\_CG} = \frac{-Q}{C_T} - \frac{C_{gs}}{C_T} V_S - \frac{C_{gd}}{C_T} V_D - A_C \Delta \psi_O \qquad (8)$$

It is also possible to use the CG to modulate the field in the SG control oxide which can perturb σ_O and ψ_O [18] , thus affecting DNA adhesion [15]. From Eq. (8), once ΔV_{th_CG} is known and with the value of A_C known, $\Delta \psi_O$ can be determined.

With frequency-mode and impedance analyses, V_{CG} or V_{REF} was first tuned to a desired DC value such that the drain current level was maintained in saturation at a predefined value usually set between 10 to 50μA. The drain current output was then fed to the TIA and then to the lock-in amplifier. The drain bias was set to 1V. The output of the TIA was then fed to a lock-in amplifier (LIA, SR830 Stanford research

systems, USA), and the Bode response was recorded. Equation (9) expresses the TIA output [32, 33],

$$v_{out} = i_d R_D \qquad (9)$$

where R_D is the feedback resistance and v_{out} is the small signal output of the TIA. In the saturation region of the transistor, the small signal current i_d can be recast in the form of $g_m v_{gs}$, where v_{gs} is the small-signal gate-to-source voltage and g_m is the small-signal transconductance. The gate voltage can be represented in terms of the transfer function across the electrolyte and the DNA layer given by the relation, $v_{gs} = H(j\omega) \times v_{in}$, where v_{in} is the AC small-signal delivered from the reference electrode. The transfer function across the DNA-transistor interface, neglecting the effect of source/drain parasitics, can be expressed by Eq. (10).

$$H(j\omega) = \frac{1 + sR_{DNA}C_{DNA}}{1 + s(R_{sol}C_{OX} + R_{DNA}(C_{OX} + C_{DNA})) + s^2 R_{DNA}C_{DNA}R_{sol}C_{OX}} \qquad (10)$$

where $C_{OX} = \frac{(C_{tun} + C_{CG}) \times C_{SG}}{(C_{tun} + C_{CG}) + C_{SG}}$ is the effective oxide capacitance. Here R_{sol} defines the solution resistance, $s = j\omega$ from the Laplace transform, and C_{DNA} and R_{DNA} the resistance and capacitance of the DNA membrane. Additional effects of the source/drain parasitic contact-lane capacitances C_{line} are not considered in the analytical derivation for simplicity [32]. To a first-order approximation, the poles and zeros are given by Eq. (11-13).

$$p1 = \frac{1}{R_{sol}C_{OX} + R_{DNA}(C_{OX} + C_{DNA})} \qquad (11)$$

$$p2 = \frac{1}{R_{sol}C_{DNA}} + \frac{1}{R_{sol}C_{OX}} + \frac{1}{R_{DNA}C_{DNA}} \quad (12)$$

$$z1 = \frac{1}{R_{DNA}C_{DNA}} \quad (13)$$

We immediately notice that if R_{sol} is low, which is an acceptable assumption when the background electrolyte salinity is high, $p1$ and $z1$ essentially capture molecular relaxations within the bandwidth of the overall response.

RESULTS AND DISCUSSION

A. Role of Surface Charges

Capacitance-voltage (CV) measurements were performed on electrolyte-oxide-semiconductor capacitors (EOS) as shown in [Fig. 13(a&b)]. Two separate interfaces were studied. The first EOS capacitor had a traditional thermally grown SiO_2 interface while a variant had a highly doped poly-silicon surface on top of thermally grown SiO_2. The thickness of the thermal SiO_2 in both cases ~30nm. The latter was used to corroborate transistor measurements as it mimics the interface of the CvMOS-electrolyte interface. Thermally grown SiO_2 possesses an intrinsically high surface hydroxyl charge density [4] (~10^{18}/m^2) and exhibits a near Nernstian (~48mV/ pH) pH response. LPCVD deposited poly-silicon however has a hydrated native oxide, is slightly porous [34], possesses a moderate to low surface hydroxyl density and exhibits

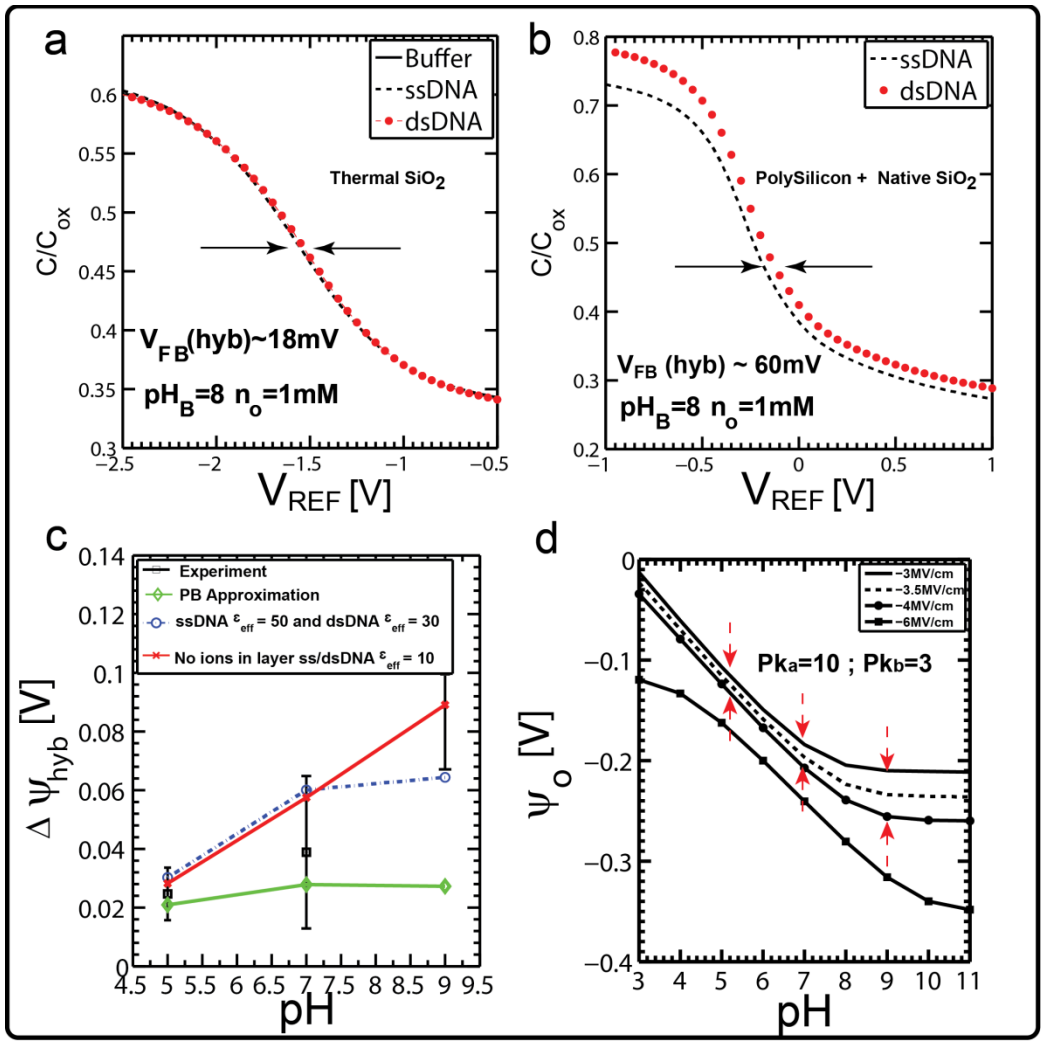

Figure 13: Experimental CV analyses of DNA hybridization performed on PLL coated EOS capacitors, depicting V_{FB} shifts for: (a) SiO_2 interface and (b) poly-silicon interface. V_{FB} shifts of ~18mV and ~60mV are observed respectively indicating the role of surface buffering in signal generation. (c) Effect of varying background pH on the DNA hybridization signal using the CvMOS transistors. As the pH is increased from 5 to 9, the hybridization signal ($\Delta\psi_O$) increased. The best theoretical fit to experiment occurs when a membrane model is assumed, where ions are completely excluded from the membrane and the permittivity within the DNA layer is low (~10). The PB model in comparison fails to provide an explanation of the experimental observation. (d) Simulation when a negative E-field is applied at the SG interface, where the pH insensitive region shifts to higher pH values. Any further change in E-field induces a maximal change in ψ_O within the pH insensitive region (starting at pH 9) which is the region of lowest buffering. As pH reduces towards5, the ψ_O response becomes more linear which is the region of strong buffering. This shows that in addition to membrane permittivity which decides the overall net magnitude, the effect of the DNA charges on the surface chemical equilibrium dictates the maximal hybridization sensitivity

a non-Nernstian pH response [18]. Hybridization measurements were performed on PLL coated EOS capacitors and we found a clear difference in V_{FB} recorded between the two surfaces. While hybridization measurements on SiO_2 surfaces resulted in a V_{FB} shift of ~18mV , measurements on poly-silicon interfaces showed a ΔV_{FB} ~50-60mV. This clearly suggests that intrinsic charge screening due to exposed surface groups reduces the sensitivity. In a previous study we observed that when the bulk salinity changed from 1mM to 150mM, ΔV_{FB} shifted from ~50mV to approximately ~10-20mV, clearly indicating Debye screening limited responses [35]. Collectively the above results suggest that intrinsic surface properties, bulk salinity and the net density of exposed hydroxyl charges play critical roles in signal generation and sensitivity.

Next, in order to ascertain the effect of varying background pH_B on molecular charge sensitivity, we varied pH_B and measured $\Delta\psi_O$ [Fig. 13(c)]. We observed that as pH_B increased from 5 to 9, $\Delta\psi_O$ increased (plotted as $\Delta\psi_{hyb}$) from ~20mV to ~85mV indicating an enhancement in sensitivity. We compared two independent models to experiments: a) the PB approximation in which the DNA layer was assumed to be akin to a charge sheet [Eq. 2] and b) a membrane model in which the electrostatics between the SG and DNA was described using Eq. (14). We included the partition effect, where (ΔG_m) represents the energy barriers that ions encounter due to permittivity differences between the membrane and electrolyte phase [Eq. (15)][11].

$$E\frac{dE}{d\psi} = \frac{2en_o}{\varepsilon_{eff}}\sinh\left(\frac{\Delta G_m + e\psi}{kT}\right) \qquad (14)$$

$$\Delta G_m = -\frac{69z^2}{a}\left(\frac{1}{\varepsilon_{eff}} - \frac{1}{\varepsilon_{medium}}\right) * 0.01036eV \quad (15)$$

where a is the ion radius and z is the valency. Here ε_{eff} represents the permittivity in the DNA layer and ε_{medium} signifies the permittivity in the bulk electrolyte. This energy difference stems from the Born-Charge dielectric interaction [11, 15, 36] in which the self energy of the ion undergoes a penalty when it crosses over from a medium of high permittivity to that of low permittivity. In order for the overall ΔG_m to be negative, ions permeate into a medium of higher permittivity (i.e. in water, $\varepsilon_{medium} = 80$) and incur an energy cost if present in a medium of lower permittivity (i.e. tightly packed DNA layers). This enhanced energy penalty leads to a lower screening charge [16] within the DNA layer which directly influences the overall $\Delta\psi_O$. A detailed analysis of the simulation methodology and theory was presented in Chapter 2 [15].

As shown in Fig. 13(c), we found the best fit across the pH_B range to occur when ions were completely excluded from the DNA layer and ε_{eff} was reduced leading to a large negative ΔG_m. With ions present, the extra screening from ions prevented a clear fit around pH_B=9. The PB approximation on the contrary fails to corroborate experiment across the entire pH_B range except at pH_B=5, clearly indicating the limitation of the model. In a short summary, signal generation during DNA hybridization is affected by surface hydroxyl screening and membrane screening, but the question still remains as to why we observed such a trend in $\Delta\psi_O$ when pH_B was varied.

In order to corroborate this trend we first revisit the results by Zhang et al., [21]. The authors showed that during hybridization ss-DNA was indeed more effectively screened at lower pH_B which then lead to an increase in the hybridization efficiency, revealed by mechanical deflections of a nano-cantilever. If this were true in our case, one would expect to have observed the opposite trend in $\Delta\psi_O$ (i.e. largest magnitude of $\Delta\psi_O$ at pH_B 5). In addition, DNA hybridization performed at two different pH_B conditions did not show a significant difference in interface impedance (see Appendix C, Fig. 40), which indicated that pH_B induced screening of DNA was not a dominant factor in signal generation at the transistor interface and that factors other than proton screening were involved.

Recent work has shown that the ionization properties of the interface can be modulated by the application of an E-field [18, 27]. DNA is negatively charged and when immobilized on the SG surface is akin to applying a net negative field at the interface. We simulated ψ_O vs. pH_B under the influence of a negative E-field [Fig. 13(d)], following the approach outlined in Part I [18]. Briefly, the pKa=10 and pKb=5 represent equilibrium constants for an EOS capacitor with a native polysilicon interface. Equations (18-20) were self consistently solved under varying E-field conditions in the underlying oxide.

$$\sigma_O = e\Gamma_{OH}\left[\frac{H_S^+}{K_b} - \frac{K_a}{H_S^+}\right] \qquad (18)$$

Here H_S^+ is the surface proton concentration, Γ_{OH} represents the neutral site density,

K_a and K_b represents the association and dissociation constant. The surface proton concentration is then related to the bulk proton concentration, H_B^+ through the Boltzmann relationship outlined in Eq. (19).

$$H_S^+ = H_B^+ \times \exp(\frac{-e(\psi_O - V_{REF})}{kT}) \qquad (19)$$

The E-field in the underlying oxide must then balance both the surface and double layer charge through Eq. (20), where σ_{DL}, represents the double layer charge [18] (see Part I for details).

$$E_{OX} = -\frac{(\sigma_O + \sigma_{DL})}{\varepsilon_{OX}} \qquad (20)$$

We found that under the influence of a negative E-field's the pH insensitive region shifted to higher pH_B values while the slope of the pH response exhibited a near Nernstian response at lower to mid pH_B. When we doubled the applied E-field (i.e. akin to doubling the DNA charge) we noticed that the maximal difference in ψ_O (indicated by the arrows and implying surface potential variations during hybridization) occurred at pH_B=9 (where the pH response is flat and least sensitive) and gradually decreased towards pH_B=5 (where the pH response is extremely sensitive). This indicated that through a combination of E-field (i.e. due to DNA charges), choice of surface equilibrium constants and pH_B (i.e. a chemical bias), the interface was pushed into an pH insensitive region (pH_B=9). At this pH condition the surface buffering capacity is weak and screening of molecular charges is low. We

point out that this pH_B region (i.e. the flat region) is not the point of zero charge (PZC). When we simulated the effect of applying an even higher hypothetical negative E-field (i.e. -6MV/cm), which is exactly double the field of ssDNA (-3MV/cm), we noticed that the trend began to reverse (i.e. $\Delta\psi_O$ at pH_B =5 appeared larger). The above results suggest that surface buffering, membrane screening and the E-field dependence of surface ionization together determine the ψ_O response during DNA hybridization.

B. Effect of Surface Modification

Prior to DNA immobilization the chips were coated with PLL in order to guarantee electrostatic interaction between DNA and the surface, and negate some of the native hydroxyl charge. As mentioned earlier, it is important to know the operating point along the pH response curve in order to completely corroborate experimental data. With surface coatings, the slope of the response curve can change [37]. Following the method outlined in [37], we simulated the effect of adding a surface coating with different surface ionization constants and site densities [Fig. 14(a)]. In addition to the native surface properties namely pK_a =11, pK_b =3 and N_S =10^{17}m^{-2}, the surface coating was described by a similar $2-pK$ model by pK_{a2}, pK_{b2} and N_{S2}. The new σ_O condition is given by Eq. (21). The interface E-field dependent ionizability is then simulated in a similar fashion as previously described for a bare surface.

$$\sigma_O = e\left\{\left\{\Gamma_{OH}\left[\frac{H_S^+}{K_b}-\frac{K_a}{H_S^+}\right]+\Gamma_{OH2}\left[\frac{H_S^+}{K_{b2}}-\frac{K_{a2}}{H_S^+}\right]\right\}\right. \qquad (21)$$

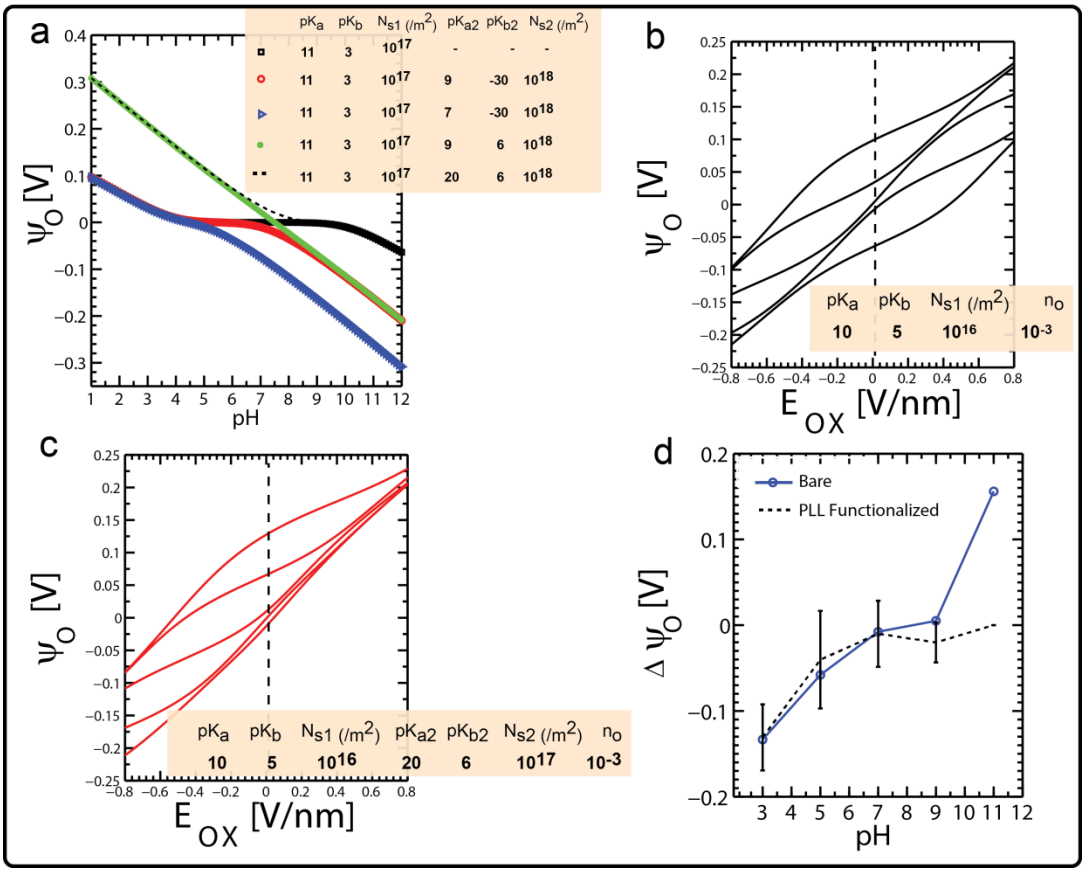

Figure 14: Effect of adding SAM's on the pH and E-field response.

(a) Variation in ψ_O as a function of pH_B for variations in ΔpK_2 , N_{S1} and N_{S2}. Decreasing pK_{b2} from -30 to 6 improves the slope of the pH response at lower pH values while decreasing pK_{a2} from 9 to 7 improves the slope at higher pH values. Increasing pK_{a2} to 20 pushes the pH insensitive region to higher pH_B values. (b) ψ_O vs. E_{OX} for varying pH_B from 11 to 3 (bottom to top). When pH_B is in the range between the $2\,pK's$, the surface buffering is weak with pH_{PZC} ~7. Here $pK_a = 10$ and $pK_b = 5$. The region marked by the dotted lines represents the E_{OX} applicable during readout. (c) ψ_O vs. E_{OX} for varying pH_B from 11 to 3 (bottom to top) with a PLL layer present. Surface ionization parameters are listed in the figure. Notice how the pH response reduces at high pH_B values. The surface buffering effect is also more pronounced (slope is smaller) for a broader range of pH_B values as seen between -0.2 and +0.2 V/nm. Here $pK_{a2} = 20$ and $pK_{b2} = 6$ is an approximation for PLL. The region marked by the dotted lines represents the E_{OX} applicable during readout (d) Experimental observation of ψ_O vs. pH_B for surface with and without PLL coating. Notice the reduction in the pH_B response at higher pH_B values agrees with the simulations shown in (a & c). Error bars represent an average of 3 experimental observations

Major assumptions in this model are that the thickness of the coating was not considered, both the native interface and surface coating share the same plane but are described by different surface constants and have different site densities. We immediately noticed that addition of a surface coating influenced the pH response drastically. Decreasing pK_{a2} improved the pH response at higher pH_B while increasing pK_{b2} did the same for the acidic branch. When we simulated the system with approximate pK_{a2} and pK_{b2} values for PLL (20 and 6 respectively) with a PZC around 12 [38], we found that the pH insensitive region extended into the basic branch. This signified the need to ascertain the role of surface coatings *a priori* since the overall pH sensitivity could shift either way between non-Nernstian and Nernstian responses, which could have a strong effect on hybridization sensitivity. In Fig. 14(b) we studied the effect of modulating the underlying E-field as a function of pH_B on an EOS system and plotted the resulting ψ_O. As the electric field was swept from -0.8V/nm to +0.8V/nm, intrinsic hydroxyl charges began to ionize in response to the applied field. The surface properties described a non-Nernstian pH_B response with the region in-between the 2 $pK's$ exhibiting a poor buffering effect (i.e. lowest ionizable hydroxyl charge and hence lowest pH_B sensitivity). With the application of a PLL coating [Fig. 14(c)] we found that the buffering effect improved across the lower to mid pH_B range since the pH insensitive region shifted to higher pH_B. Experimental observations [Fig. 14(d)] depict the CvMOS pH_B sensitivity before and

after PLL addition. We immediately noticed that the difference in ψ_O reduced drastically at higher pH_B while it maintained a near Nernstian response at lower pH_B . Since the maximal DNA hybridization sensitivity was observed at pH_B =9 and sensitivity is maximal when the pH response is least sensitive, the additional effect imparted by the PLL coating most likely plays a key role in establishing this condition.

C. The Response Curve

It is critical to model the relation between complementary DNA strands in solution (N_C) and the maximal density of surface-bound double stranded DNA (N_{DS}) for hybridization sensing. In Fig. 15 we plotted the effect of varying the target concentration N_C on the net signal sensitivity. We fitted the experimental data points to two separate adsorption isotherms of Langmuir and Langmuir-Freundlich (LF) approximations. The Langmuir isotherm is based on the assumption of a monolayer molecular coverage without biomolecular interaction or surface heterogeneity as shown in Eq. (22) [11, 25].

$$N_{DS} = N_P \frac{N_C K_A}{N_C K_A + 1} \qquad (22)$$

where N_P represents the total surface bound single stranded DNA and K_A is the equilibrium association constant. However since the transistor measures charge, Eq. (22) can be recast into the form [25, 39]

$$\Delta V_{TH} = \frac{q}{C_O}[B]_{mac} \frac{N_C K_A}{N_C K_A + 1} \qquad (23)$$

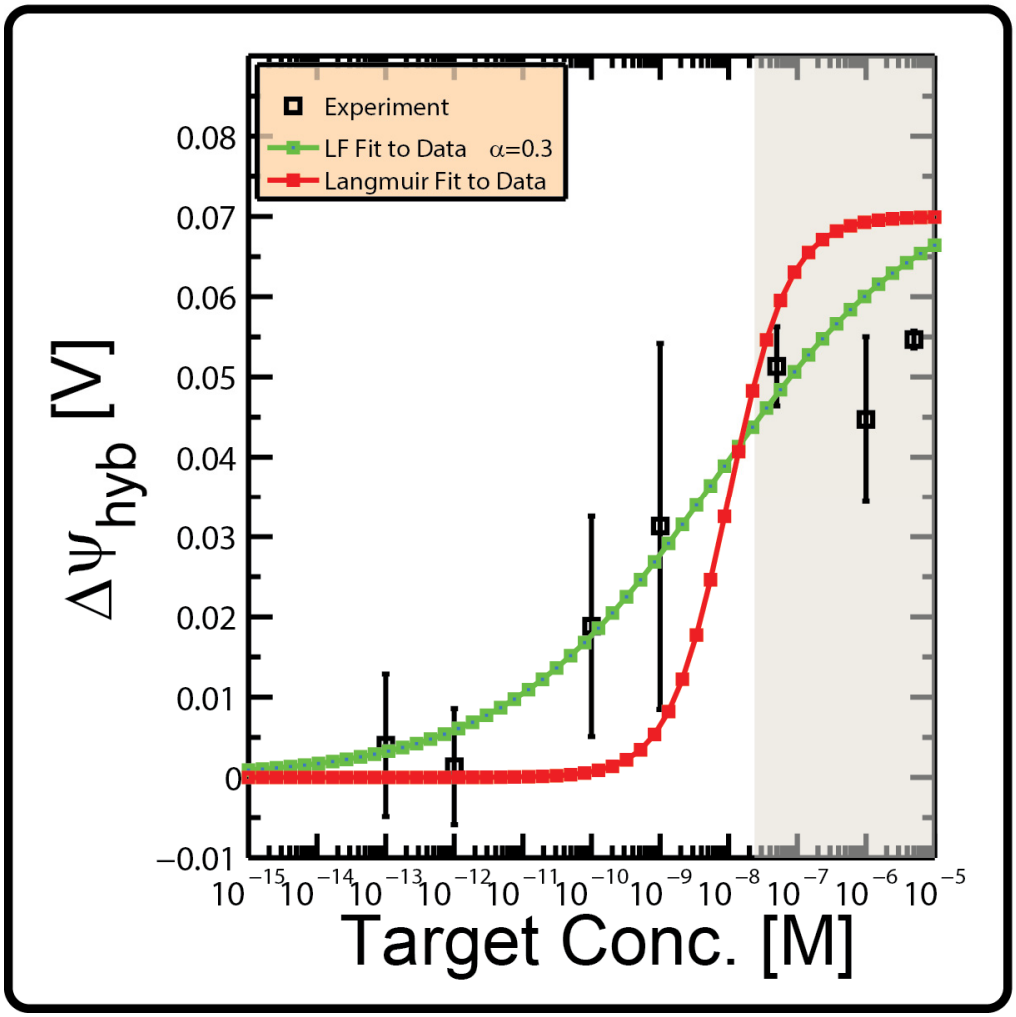

Figure 15: Langmuir and Langmuir-Freundlich (LF) isotherms are used to fit the experimental data: $\alpha = 1$ for the Langmuir isotherm and $\alpha = 0.3$ for the LF isotherm which accounts for surface heterogeneity. At high target concentrations the response first saturates and then decreases slightly indicating Coulomb blockage of DNA hybridization. A limit of detection between ~0.1-1nM and $k_D \sim 20nM$ are extracted.

Here q is the charge contributed by the adsorbed molecules, C_O is the molecule/channel capacitive coupling, and $[B]_{\max}$ is the maximal density of functional binding sites. $\frac{q}{C_O}[B]_{mac}$ and K_A represents the maximal sensors response and affinity

properties [25], which can be extracted from experiments for a series of N_C. Most interfaces, especially CMOS post-processed surfaces, exhibit a large degree of heterogeneity. In addition, given the purely electrostatic DNA-PLL interaction, the uniformity in surface binding energies and the assumption of no intermolecular interaction has limited applicability. In order to account for such effects, various extensions to the Langmuir isotherm have been proposed. One such model is the Langmuir-Freundlich (LF) isotherm outlined in Eqn. (24) [11].

$$\Delta V_{TH} = \frac{q}{C_O}[B]_{mac}\frac{(N_C K_A)^{\alpha}}{(N_C K_A)^{\alpha}+1} \qquad (24)$$

where α is a parameter between 0 and 1 to account for the surface heterogeneity. When α =1, the LF isotherm reduces to the Langmuir isotherm. As shown in Fig. 15, the LF isotherm provided a reasonable fit to the data with α =0.3, while the generic Langmuir isotherm failed to provide a good match. From the LF fit we extracted a limit of detection (LoD) between 0.1nM to 1nM and an association constant K_A of $0.5\times10^{8}(M^{-1})$ (K_D~20nM, i.e.$(K_A = 1/K_D)$). Remarkably this value of K_D is lower than the one reported on lysine-coated nanowires (K_D~200nM) [3] , larger than the values reported on PNA-DNA interaction on nanowire FET's (K_D~5nM) [40], but in line with simulation results presented in [11] (K_D~10nM). We attribute these differences to surface heterogeneity, the choice of α in the LF isotherm, and the low intrinsic surface charge density exhibited by poly-silicon surfaces. We also point out that at high target concentrations, the ψ_O shift saturated and even reduced slightly. We attribute this reduction in sensitivity to Coulomb blockage of DNA hybridization

[24], in which incoming complementary DNA strands feel a repulsion upon entry into the probe layer. These results strongly suggest that surface heterogeneity and probe/target concentrations should be considered in order to fully explain the surface response [41] and should be carefully tailored to maximize sensitivity.

D. Mechanisms of Signal Enhancement

It is well known that in order to achieve efficient hybridization and reduce inter-strand repulsion, the background saline concentrations need to be high [26]. However, as saline concentrations increase, Debye screening limits the net molecular charge detectable at the transistor interface. Such screening limited responses make it hard to detect and sort different lengths of DNA molecules. It is for this very reason that most hybridization sensing experiments are performed under low saline conditions. We used frequency-mode Bode plots (see methods) in which the poles and zeros are sensitive to molecule-electrode interactions to detect DNA hybridization as a function of molecular length [Fig. 16]. In Fig. 16(a&b) we plot the ex-situ transfer function (background buffer subtracted). We observed that as the molecular length increased from 16bP to 48bP, the interfacial impedance increased as evidenced by the attenuation in magnitude [Fig. 16(a)] and the position of the trough. The phase plot depicted a corresponding attenuation typical of an RC relaxation with the trough moving towards lower frequencies as molecular length increased. The RC time constant is sensitive to both the interfacial resistance and a large induced interfacial dipole moment, a consequence of increased molecular weight of the adsorbed DNA. Counterion relaxation are also known to occur in the range between 100Hz and

100KHz and induce a rotational time constant dependent on molecular weight as well [42]. Together these effects give rise to a change in the net interfacial impedance. We also point out that the SG size is large which leads to a large double layer capacitance. As the frequency is swept, the double layer polarization rolls off immediately within a few KHz and thus polarization limitations are avoided at higher frequencies.

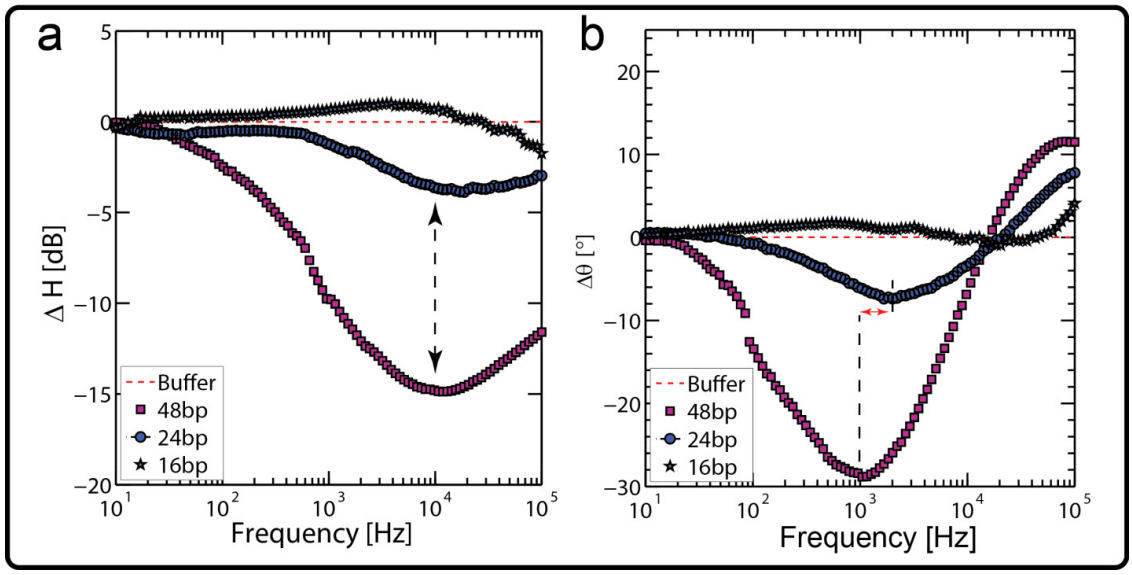

Figure 16: Ex-situ frequency response depicting (a) magnitude and (b) phase for short stranded DNA hybridization as a function of varying nucleic acid length. As the length of DNA strand is increased the interfacial impedance increases (shown by dotted arrow) leading to a larger attenuation in the magnitude plot. A corresponding relaxation is observed in the phase. An increase in the RC time constant is depicted by the red arrow.

While frequency-mode detection avoids limitation due to screening, allows for biosensing under high saline conditions and is pH insensitive (see Appendix C, Fig. 40), direct detection of intrinsic molecular charge is hard. So the question remains as to whether it is possible to improve the hybridization response and at the same time preserve the ability to detect charge. We examined the effect of adding trace amounts of multivalent salt to a low monovalent saline background during the

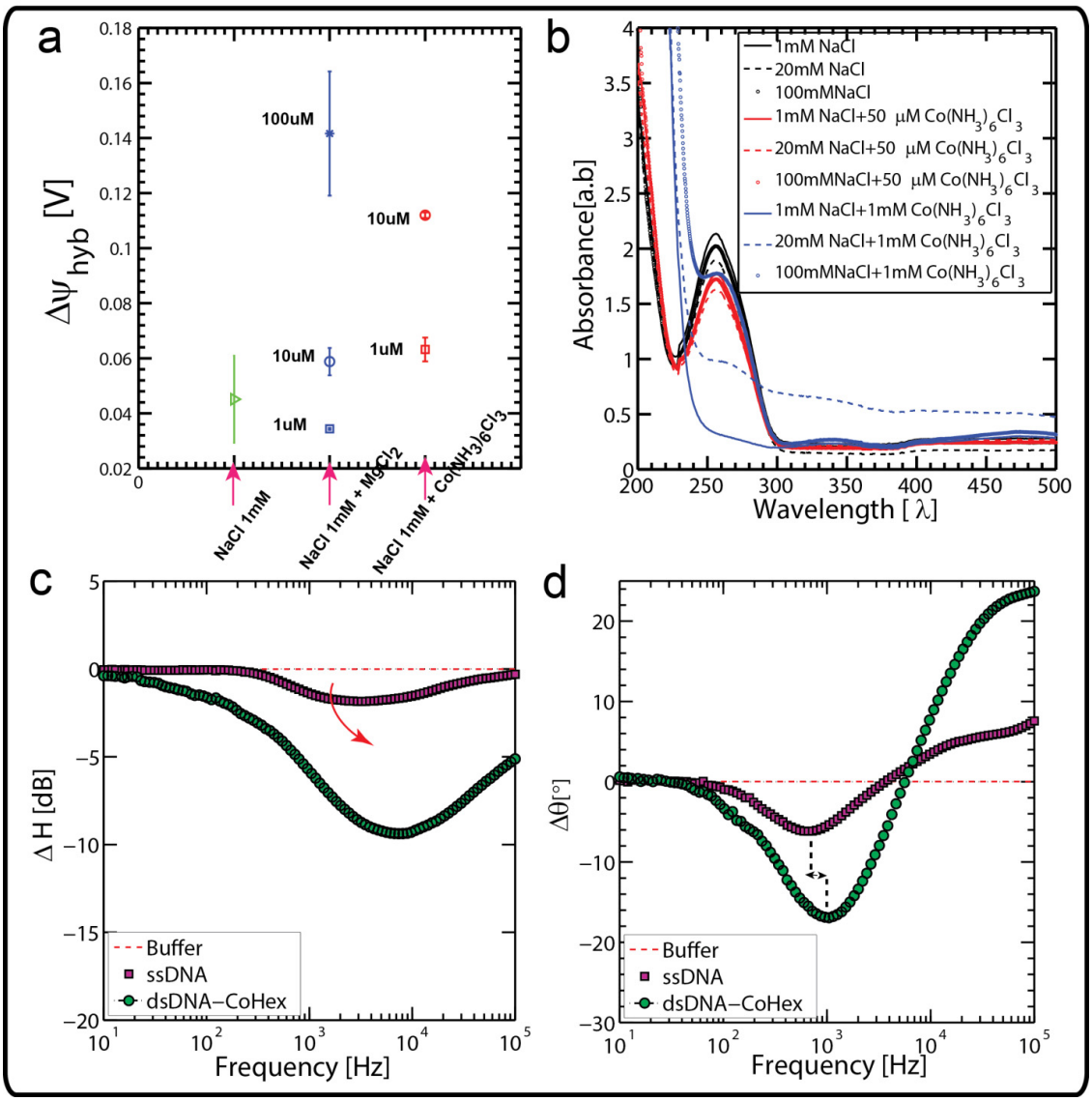

Figure 17: (a) Effect of adding trace amounts of multivalent ions to the complementary strands during hybridization. As the valency is increased, $\Delta\psi_{hyb}$ sensitivity improves. (b) UV spectrophotometry measurements of 25bP DNA treated with multivalent ions indicates no molecular precipitation when 50μM $Co(NH_3)_6Cl_3$ is added but strong precipitation for 1mM $Co(NH_3)_6Cl_3$. Ex-situ impedance response depicting (c) magnitude and (d) phase for a hybridization reaction with trivalent ions added only during complementary strand addition. Notice a clear increase in interfacial resistance indicated by the large attenuation in signal when the complementary strand is introduced. A corresponding relaxation in phase is observed. The RC time constant decreases upon complementary strand addition in comparison to ss-DNA (depicted by the arrow in (d)) indicating a slight reduction in interfacial resistance.

hybridization phase alone and measured ψ_O [Fig. 6]. Immobilization of ss-DNA was

carried out in 1mM NaCl while complementary ss-DNA was added in 1mM NaCl solution with trace $MgCl_2$ and $Co(NH_3)_6Cl_3$ ranging from 1μM to 100μM. It was immediately clear that adding trace amounts of multivalent ions improved the surface sensitivity by nearly ~80-100mV with 100μM of $MgCl_2$ and ~60mV with just 10μM of $Co(NH_3)_6Cl_3$. Any further increase in the $Co(NH_3)_6Cl_3$ concentration lead to a reversal in ψ_O (not shown), indicating overscreening and possible charge inversion at the transistor surface [18]. We explain the increased sensitivity as follows. As multivalent ions are introduced into the sample solution, the counterion cloud around DNA is perturbed [43]. Multivalent ions have a strong tendency to bind to DNA strands, displace monovalent ions[43], condense onto the phosphate backbone [30] and in some cases even reversing the charge on the molecule [44]. These previous studies, suggests that the local screening cloud around the DNA molecule is predominantly comprised of trace multivalent ions, possibly due to enhanced electrostatic effects [44, 45]. For example with a 1μM DNA and 10μM $Co(NH_3)_6Cl_3$ concentration in a sample would imply 10 Co ions for every ss-DNA molecule. Given the DNA length to be ~25bP (i.e 25 electrons for ss-DNA and 50 electrons after duplex formation) would imply that nearly the entire ss-DNA molecule is screened when added to the chip. This in itself will allow for enhanced screening during the hybridization process. If the counterions were still strongly attracted to the DNA molecule, the screening would be higher and we would have observed a diminished $\Delta\psi_O$ response. We however reiterate that once hybridization occurs, ions are excluded from the membrane owing to the low permittivity as previously explained. With

multivalent ions the exclusion effect is stronger [Eq. (15)], since ΔG_m is directly proportional to the square of valency. This causes ion exclusion from within the DNA layer and the multivalent ions form the screening layer just outside the DNA lattice. However, multivalent ions are in trace quantity which implies a larger Debye length [Eq.(3)] and lower screening capacitance [46] which would directly induce an increase in $\Delta\psi_O$. We do point out that when we increased the background monovalent concentration to 100mM, we did not observe any enhancement in signal upon multivalent ion addition, indicating that competition between monovalent and multivalent species is central to signal enhancement. In order to be certain that DNA did not completely precipitate out of solution under the influence of multivalent ions, we performed UV spectrophotometry studies under varying conditions of background trivalent salt [Fig. 6(b)]. We found that when $Co(NH_3)_6Cl_3$ concentrations on the order of ~1mM were added, a lowering in the absorbance was observed. However at 50 μM $Co(NH_3)_6Cl_3$ concentration the amount of DNA precipitating out of solution was negligible, clearly showing that DNA precipitation during experiment was insignificant under the concentrations used.

Taken together Fig. 17(a&b) suggests that multivalent ions condense onto DNA, cause aggregation and induce condensation onto the sensing gate surface, thus improving the hybridization sensitivity and increasing the sensitivity to net molecular charge. In order to further corroborate the increase in interfacial DNA adsorption, we performed frequency-mode detection during the hybridization process [Fig. 17(c&d)] and found a clear increase in interfacial impedance with a RC relaxation occurring ~1

KHz. In comparison, hybridization measurements performed on 25bP DNA in the absence of added multivalent ions showed an RC relaxations ~3KHz [Fig. 16], suggesting that multivalent ions increase DNA aggregation at the interface. Impedance analysis under higher concentrations of $Co(NH_3)_6Cl_3$ revealed an outward movement in the pole-zero response, indicating a reduced interfacial impedance possibly as a result of DNA desorption due to excess ion condensation (not shown). It is interesting to note that in Fig. 17(d) we observed a slight decrease in the RC time constant with respect to the ss-DNA, possibly due to trace Co ions within the DNA layers decreasing the AC resistance at the interface. Together these results suggest that modifying the local screening profile, inducing aggregation and reducing repulsion by the addition of trace multivalent ions can be used as a signal enhancement strategy.

CONCLUDING REMARKS

We presented detection of DNA hybridization using EOS and floating gate ISFET's. We highlighted the roles of bulk pH , surface ionizability, surface coatings, and target concentration on signal generation. Our results suggest that in addition to surface properties, membrane screening and field dependent surface ionization play a key role in deciding signal sensitivity. Models including permittivity differences between the DNA layer and bulk were presented and fitted to experiments. Signal enhancement strategies using frequency-mode sensing and use of multivalent salts to perturb the local screening profile were proposed. DNA length sorting and signal enhancement by ~100mV was demonstrated.

Supplemental Material: Supplementary material accompanies this chapter, refer Appendix-C.

REFERENCES

[1] L. Bandiera *et al.*, Biosens. Bioelectron. **22**, 2108 (2007).

[2] M. Barbaro, A. Bonfiglio, and L. Raffo, IEEE Trans. Electron Devices **53**, 158 (2006).

[3] Y. L. Bunimovich *et al.*, J. Am. Chem. Soc. **128**, 16323 (2006).

[4] J. Fritz *et al.*, Proc.Natl.Acad.Sci. U.S.A. **99**, 14142 (2002).

[5] G. Zheng *et al.*, Nat Biotech **23**, 1294 (2005).

[6] E. Katz, and I. Willner, Electroanalysis **15**, 913 (2003).

[7] E. Stern *et al.*, Nature **445**, 519 (2007).

[8] F. Uslu *et al.*, Biosens. Bioelectron. **19**, 1723 (2004).

[9] A. Poghossian *et al.*, Sens. Actuators, B **111–112**, 470 (2005).

[10] I. Y. Wong, and N. A. Melosh, Biophys. J. **98**, 2954 (2010).

[11] Y. Liu, and R. W. Dutton, J. Appl. Phys. **106** (2009).

[12] D. Landheer *et al.*, J. Appl. Phys. **98**, 044701 (2005).

[13] D. Landheer *et al.*, IEEE Sens. J. **7**, 1233 (2007).

[14] A. G. Cherstvy, Biosens. Bioelectron. **46**, 162 (2013).

[15] K. Jayant *et al.*, Phys.Rev.E **88**, 012802 (2013).

[16] T. Windbacher, V. Sverdlov, and S. Selberherr, 13th International Workshop on Computational Electronics,IWCE 1(2009).

[17] M. W. Shinwari, and M. J. Deen, Sens. Actuators, B **171–172**, 463 (2012).

[18] K. Jayant *et al.*, Phys.Rev.E **88**, 012801 (2013).

[19] R. B. M. Schasfoort *et al.*, Anal. Chim. Acta **238**, 323 (1990).

[20] G. Shalev, Y. Rosenwaks, and I. Levy, Biosens. Bioelectron. **31**, 510 (2012).

[21] J. Zhang *et al.*, Langmuir **28**, 6494 (2012).

[22] D. A. Cherepanov *et al.*, Biophys. J. **85**, 1307 (2003).

[23] B. Dorvel, B. Reddy, and R. Bashir, Anal. Chem. **85**, 9493 (2013).

[24] A. Vainrub, and B. M. Pettitt, Phys.Rev.E **66**, 041905 (2002).

[25] Duan X *et al.*, Nature Nanotechnology **7**, 401 (2012).

[26] C. Gentil, G. Philippin, and U. Bockelmann, Phys.Rev.E **75**, 011926 (2007).

[27] Z. Jiang, and D. Stein, Langmuir **26**, 8161 (2010).

[28] Toumazou C *et al.*, Nature Methods **10**, 641 (2013).

[29] B. Veigas *et al.*, Biosens. Bioelectron. **52**, 50 (2014).

[30] V. A. Bloomfield, Current Opinion in Structural Biology **6**, 334 (1996).

[31] N. Y. M. Shen *et al.*, IEEE Trans. Electron Devices **50**, 2171 (2003).

[32] S. Ingebrandt *et al.*, Biosens. Bioelectron. **22**, 2834 (2007).

[33] M. M. G. Antonisse *et al.*, Anal. Chem. **72**, 343 (1999).

[34] N. Zehfroosh, M. Shahmohammadi, and S. Mohajerzadeh, Electron Device Letters, IEEE **31**, 1056 (2010).

[35] K. Jayant, K. Auluck, and E. C. Kan, in *IEEE Sensors* (2013), pp. 1.

[36] J. Israelachvilli, *Intermolecular & Surface Forces* (Academic Press, London, 1992).

[37] A. van den Berg *et al.*, Sensors and Actuators **8**, 129 (1985).

[38] D. Stein, M. Kruithof, and C. Dekker, Phys. Rev. Lett. **93**, 035901 (2004).

[39] M. Abe *et al.*, JOURNAL OF PHYSICAL CHEMISTRY C **111**, 8667 (2007).

[40] A. De *et al.*, ACS Applied Materials & Interfaces **5**, 4607 (2013).

[41] A. W. Peterson, R. J. Heaton, and R. M. Georgiadis, Nucleic Acids Res. **29**, 5163 (2001).

[42] R. Pethig, and D. B. Kell, Physics in Medicine and Biology **32**, 933 (1987).

[43] K. Andresen *et al.*, Biophys. J. **95**, 287 (2008).

[44] A. Y. Grosberg, T. T. Nguyen, and B. I. Shklovskii, Rev.Mod.Phys. **74**, 329 (2002).

[45] F. H. J. van der Heyden *et al.*, Phys. Rev. Lett. **96**, 224502 (2006).

[46] B. D. Storey, and M. Z. Bazant, Phys.Rev.E **86**, 056303 (2012).

CHAPTER 5: INTEGRATING SIGNAL AMPLIFICATION BY SEQUENCE-SPECIFIC SELF-ASSEMBLY WITH CMOS IMPEDIMETRIC READOUT FOR PATHOGENIC DNA DETECTION

CHAPTER OVERVIEW

High saline conditions are necessary for nucleic acid hybridization but are traditionally incompatible with most common electrochemical approaches. We report on CMOS-based impedimetric detection of pathogenic DNA saline conditions in which the hybridization signal is amplified by DNA self-assembly in solution phase and the transistor transfer function (TF) is used for spectroscopic analysis. Branched Y-shaped DNA structures, termed Y-DNA monomers are tagged with specific short single-stranded DNA (ssDNA) capture probes on the terminal of each arm of the Y-DNA, exhibiting a half match to the target DNA sequence. Upon addition of target, these capture probes hybridize with complementary sequences on the target strand. This reaction occurs rapidly due to the favorable kinetics of solution phase hybridization. Two different types of Y-DNA monomers (containing partially complementary capture sequences i.e. 3' and 5') are thus linked to each other through a single target sequence on each arm. This causes a linkage between multiple Y-DNA monomers

which results in relatively large aggregates with a distinct increase in molecular weight and size. In stark contrast, in the absence of correct target sequences, the Y-DNA fragments remain disassociated in solution and do not form aggregates. Unlike existing assays that use branched DNA motifs, our proposed method is immobilization and enzyme free. As a prototypical pathogen target, we chose a nucleic acid sequence from a conserved region of the HIV genome. Two types of Y-DNA monomers tagged with capture probes were treated with both complementary and mismatched target sequences in a high saline condition (500 mM) in order to ensure maximum hybridization efficiency. For electronic readout, the solution was dispensed onto floating-gate ion-sensitive transistors and the transfer function (TF) probed across a broad frequency range. The first pole (*p1*) was found to be extremely sensitive to the resistive component of the molecule-transistor interface, while the first zero (*z1*) was determined by the DNA aggregate relaxations, reflective of capacitive effect. At low target concentrations (~1 pM), the Y-DNA-ssDNA target interaction resulted in an increase in the interfacial resistance reflected by a clear inward shift in *p1* which is dominated by the un-reacted monomer surface density. Increasing the target concentration further caused *p1* to move out but *z1* to move in. This indicates that as aggregation occurs the resistive component at the interface reduces while capacitive effects begin (ex. counterion polarization) to dominate due to the amplified molecular weight and size with relaxations in the KHz range. Addition of Au nano-particles functionalized with capture probes was found to further increase the sensitivity due to increased polarization, a consequence of increased aggregate size, improving the limit of target detection to ~100 fM. Our study presents significant improvement over

previous efforts in terms of device functionality (impedance vs. charge readout), transistor design (dual-gate control), molecular amplification and recognition, buffer saline conditions (high salt) and limit of detection (LOD) on CMOS (100 fM ~ 1 pM). This enzyme-free, heat-cycle-free and label-free DNA detection scheme is highly specific and sensitive, and hence suitable for point-of-care (PoC) diagnostics.

INTRODUCTION

Diagnostics plays a central role in modern medical practice as it enables informed treatment decisions, helps monitor disease state, and provides effective viral and bacterial screening. Broad data collection also ensures emergency interventions and long-term strategies for public health. In developing countries, access to hospitals and advanced diagnostic centers is often restricted except in urban centers. Diagnosis that requires skilled personnel or complicated equipment is thus difficult in rural areas. Lack of basic infrastructure such as clean water, electricity, and cold storage, further complicates diagnostic procedures in such resource limited settings. Point-of-care (PoC) detection, i.e., testing carried at or near the patient home , is thus an extremely important option for infectious diseases such as HIV, malaria, tuberculosis, and sexually transmitted diseases (STD)[1, 2].

Recently a number of reports have outlined the use of NATs (Nucleic Acid Tests) for the diagnosis and therapeutic monitoring of infections[1-6]. Such methods are sensitive and identify specific fragments of infectious agent genome. In comparison to immunological (antibody-based) biomarkers, NATs exhibit several important practical

advantages, such as straight forward design of specific recognition elements (primers and probes) with predictable molecular behavior including binding affinities, and compatibility with enzymatic target amplification methods. Amplification techniques such as polymerase chain reaction (PCR), as well as isothermal amplification methods such as loop mediated isothermal amplification (LAMP), nucleic acid sequence-based amplification (NASBA) and transcription-mediated amplification (TMA)[2] are widely used for genomic screening of viruses such as hepatitis C (HCV) and HIV. Most of these amplification procedures use enzymes such as polymerases, which are effective for target amplification of nucleic acids but introduce critical challenges for PoC detection. Specifically, enzymes often require refrigeration for transport and storage. PCR also demands careful temperature control, rendering micro and nanoscale integration challenging. Approaches that avoid enzymes and thermal control however are slowly gaining precedence [4, 7-9], and represent one important step towards the development of novel PoC diagnostics[2, 10-13].

Over the last few years, PoC readout has been actively sought through optical, mechanical and electrical means [14-21]. One method of electrochemical readout that is particularly attractive for diagnostics is the use of field effect transistors (FET's) that transduce biochemical and ionic changes to current through surface charge based sensing[22, 23]. However, direct molecular charge transduction is known to be affected by Debye screening effects close to the sensing interface[24, 25]. Strong nonlinear screening of surface charge due to mobile counterions in the electrolyte causes a rapid decay in surface potential emanating from the sensing interface into the bulk electrolyte. The transistor is sensitive to molecular charges only within this

effective length. As the screening effect becomes stronger under moderate to high saline conditions, the Debye length is reduced and the net sensitivity to molecular charge decreases. It is important to note that DNA hybridization and recognition is most effective under high saline conditions (> 500 mM) where inter-strand repulsion is low, but this scenario would entail low sensitivity to molecular charge due to enhanced screening. Nonetheless, such charge based sensing schemes have been shown to be massively scalable and highly sensitive when combined with PCR or isothermal amplification strategies[13, 21, 26]. Sensing in these cases is improved through the surface proton sensitivity, amplified molecular density, and nanowire surface-to-volume effects to be suitable for PoC. However, no successful report[27], to the best of our knowledge, couples enzyme-free and heating-free strategies for signal enhancement with transistor readout. Impedimetric detection can potentially overcome the screening limited response of potentiometric sensors by probing signals at higher frequencies beyond the Debye layer relaxation limit[28]. Most of these studies use standalone metal electrodes[29] with off-chip amplification and sensing[30]. Over the last few years, however, there have been a number of reports that utilize ion-sensitive FET's (ISFET's) operating in frequency mode[25, 31-36] motivated by the need to push transistor-based detection beyond the screening limited regime. Under moderate saline conditions, this would allow for simultaneous charge and impedance sensing. However, two central questions remain: a) Is it possible to detect low concentrations of pathogenic DNA using an enzyme-free and PCR-free approach using frequency-mode transistor readout, and b) What are the essential molecular features that can be captured under such readout operations?

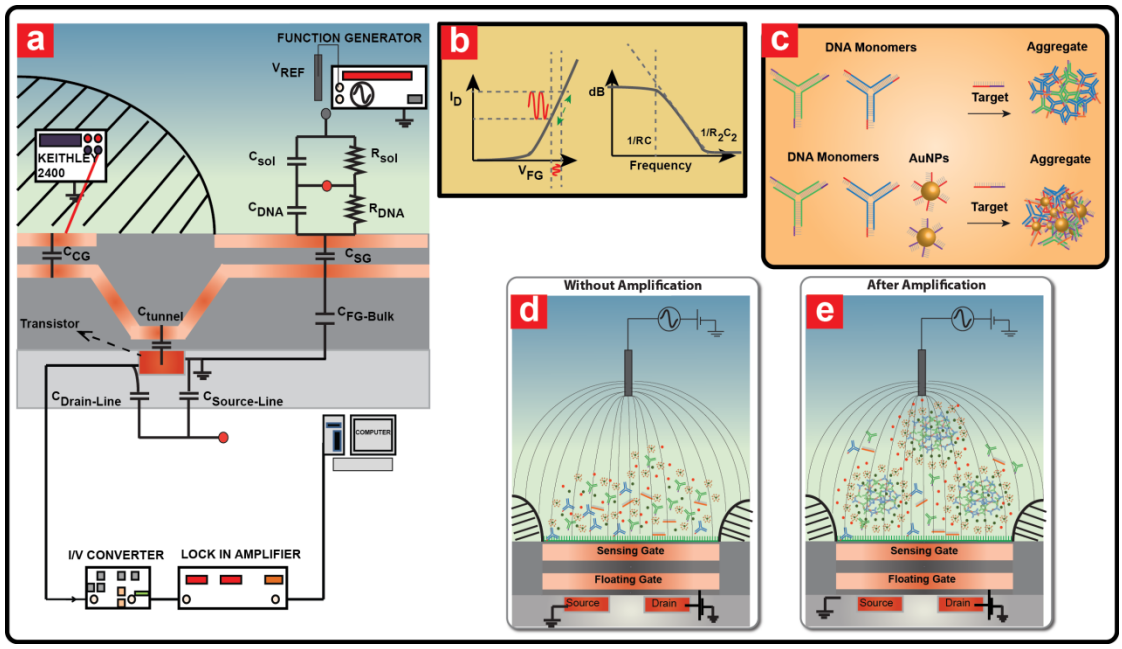

Figure 18: (a) CvMOS cross-section depicting the split-signal impedance spectroscopy setup. The DC bias is supplied via CG while the reference electrode delivers the AC excitation. (b) The schematic I-V curve representing the region of operation (left) and an example of the resulting Bode plot (right). (c) DNA amplification with and without AuNPs. Branched Y-DNA monomers are tagged with specific capture probes. Upon addition of target pathogen, enhanced hybridization results in aggregate formation via self assembly. Addition of capture-probe functionalized AuNPs further increases the aggregate size and polarization. (d) Interface condition without target addition results in large RDNA. (e) Addition of target treated sample results in lower RDNA and higher CDNA.

In this chapter we introduce the use of branched Y-DNA monomers[37] as molecular labels which self assemble into aggregates upon hybridization in the presence of pathogenic targets. This aggregation effect is in essence an amplification in signal and is read out by the frequency-mode operation of a dual-gate ISFET termed the CvMOS (Chemoreceptive neuron MOS)[24, 38]. The frequency response as a Bode plot characterized by poles and zeros are sensitive to the net change in interfacial AC resistance and capacitance[31]. Apart from using Y-DNA monomers, we also examine the effect of adding Au nanoparticle labels functionalized with single-stranded DNA (ssDNA) capture probes as an improved signal amplifying strategy.

MATERIALS AND METHODS

A. Transistors and Operating Principles

CvMOS transistors were fabricated in a 1.5 μm AMI foundry process as described previously[24, 25]. Briefly, the transistors are comprised of independently tunable control (CG) and sensing (SG) gates coupled to a common extended floating gate (FG) [Fig. 18(a)]. The tunnel oxide (the oxide between the channel and FG) is 10nm thick, while the control oxide (the oxide between CG/SG and FG) is 35nm thick. The CG areas measured $25\mu m \times 40\mu m$ while SG areas varied between $5\mu m \times 400\mu m$ and $200\mu m \times 400\mu m$. The reference electrode ($Ag / AgCl$, Warner instruments) pins the electrolyte bulk to a defined electrochemical potential (V_{REF}) and also supplies a global small signal AC perturbation. The CG defines the threshold voltage (V_{TH}) [24, 25] and the quiescent point, and provides additional voltage offset if required. This reduces the burden on the reference electrode to solely provide a global DC bias which is restrictive with large arrays. We do however point out that in the present study the reference electrode was also used to control the DC operating point, particularly when dealing with large SG/CG area ratios, since the application of high CG biases (~10-18V to achieve saturation) can induce tunneling or shift the field in the control oxide. Such changes in electric field have been shown to modulate the ionic charge, surface pH and DNA binding properties[24, 25] which can further make it challenging to maintain a constant operating condition and de-couple different contributions to signal generation.

The transistor transfer characteristics (i.e., the drain current I_D as a function of the CG/SG bias) [Fig. 18(b) (left)] were recorded using a Keithley 236 source measure unit (SMU) (Keithley Instruments, USA) for I_D ($V_D = 1V$) and a Keithley 2400 (Keithley Instruments, USA) was used to sweep V_{CG}. In order to ascertain the impedance response [Fig. 18(b) (right)], V_{CG} or V_{REF} was first tuned to a desired DC value such that the drain current level was maintained in saturation at a predefined value usually set between 10 to 50 μA. The drain current output was then fed to a transimpedance amplifier (TIA, SR570 Stanford research systems, USA) with a suitable gain setting such that the TIA output was not saturated. No filter settings were used. The bias on the TIA was set to 1V. The output of the TIA was subsequently fed to two different lock-in amplifiers (LIA, SR830 and SR844 Stanford research systems, USA) [Fig. 18(a)] depending on the frequency range of interest and the Bode response [Fig. 18(b)] was subsequently recorded. The TIA output relates to the CvMOS readout current as,

$$v_{out} = i_d R_D \qquad (1)$$

where R_D is the feedback resistance and v_{out} is the small signal output of the TIA. In the saturation region of the transistor, the small signal current i_d can be recast in the form of $g_m v_{gs}$, where v_{gs} is the small-signal gate-to-source [Fig. 18(b)] voltage and g_m is the small-signal transconductance. The gate voltage can be represented in terms of the transfer function across the electrolyte and the DNA layer given by the relation, $v_{gs} = H(j\omega) \times v_{in}$, where v_{in} is the AC small-signal delivered from the reference

electrode. The transfer function across the DNA-transistor interface can be expressed by Eq. (2).

$$H(j\omega) = \frac{1 + sR_{DNA}C_{DNA}}{1 + s(R_{sol}C_{OX} + R_{DNA}(C_{OX} + C_{DNA})) + s^2 R_{DNA}C_{DNA}R_{sol}C_{OX}} \qquad (2)$$

where $C_{OX} = \frac{(C_{tun} + C_{CG}) \times C_{SG}}{(C_{tun} + C_{CG}) + C_{SG}}$ is the effective oxide capacitance, R_{sol} the solution resistance, $s = j\omega$ from the Laplace transform, C_{DNA} and R_{DNA} the resistance and capacitance of the DNA membrane, C_{tun} the FG to channel capacitance, C_{SG} the sensing gate interpoly oxide capacitance, and C_{CG} the control gate interpoly oxide capacitance. Additional effects of the source/drain parasitic contact-lane capacitances, C_{line}, are not considered in the analytical derivation for simplicity, but are included in the SPICE simulations to help deliver an intuitive understanding of the dominant poles and zeros [Fig. 2], particularly for the limiting behavior at higher frequencies. The analytical transfer function (TF) without accounting for C_{line} represents two poles and one zero, as defined by Eqs. (3-5). With C_{line} included, the system will instead be comprised of two zeros and three poles (TF not shown).

$$p1 = \frac{1}{R_{sol}C_{OX} + R_{DNA}(C_{OX} + C_{DNA})} \qquad (3)$$

$$p2 = \frac{1}{R_{sol}C_{DNA}} + \frac{1}{R_{sol}C_{OX}} + \frac{1}{R_{DNA}C_{DNA}} \qquad (4)$$

$$z1 = \frac{1}{R_{DNA}C_{DNA}} \qquad (5)$$

The CG or reference electrode is re-biased in order to maintain the constant quiescent

point of I_D and hence V_{FG}. V_{FG} in the original vMOS operation[39] can be expressed as

$$V_{FG} = \frac{C_{CG}V_{CG}}{C_T} + \frac{C_{SG}(\psi_O - V_{REF})}{C_T} + \frac{C_{GS}V_S}{C_T} + \frac{C_{GD}V_D}{C_T} - \frac{Q}{C_T} \qquad (6)$$

where C_{GS} and C_{GD} represent the gate to source/drain parasitics, V_S and V_D the source and drain potentials, ψ_O the SG surface potential, C_T the total capacitance seen from FG, V_{REF} the reference electrode potential and Q the stored charge on FG.

B. Reagents

The chip was cleaned with DI water and isopropyl-alcohol (IPA) before each test. A small reservoir made of epoxy was created to isolate the fluid from the electrical bond pads. In between experiments with DNA, each chip was additionally treated with soap and gently swabbed to remove any residual DNA. The chips were subsequently treated with Poly-L-Lysine (PLL) (SIGMA, USA) in order to ensure attraction of monomer aggregates to the sensing surface. Both target fragments and monomers were maintained in a hybridization buffer (10 mM Tris pH 8, 500 mM NaCl and 1 mM EDTA) which was also used as the blank solution to ascertain the baseline for every experiment. Y-DNA monomers were prepared as follows: three ssDNA molecules were rationally designed with specific sequences such that each was partially complementary to another. These ssDNA molecules (IDT, USA) were mixed in an equimolar ratio, resulting in self-annealed, branched Y-DNA[11, 37]. Each branch of the Y-DNA (Table 1) contained three ssDNA capture sequences partially (i.e. half) specific to the target of interest, which in this case represented a conserved region

from the HIV genome (50 bp, Table 1). For aggregate formation, Y-DNA monomers with a final concentration of 3.3 nM for each of the 3' Y-DNA and 5' Y-DNA were mixed with target DNA (50 bp, Table 1). This resulted in rapid formation of DNA aggregates within ~15-20 minutes of treatment. We then performed experiments on transistors in which the total Y-DNA monomer concentrations (including both 3' Y-DNA and 5' Y-DNA monomers) were maintained at ~6.6 nM while the target concentrations varied in order to test the limit of detection (LOD). Hybridization was performed in solution phase and then dispensed on the CMOS chip. Experiments were then performed in a light-tight environment.

Gold (Au) nanoparticles (AuNP) (10 nM for 3'AuNP and 10 nM for the 5'AuNP) of 15 nm diameter were synthesized in-house using previously published methods[40] and made up to a final concentration of 20 nM. The samples were treated with ssDNA capture sequences specific to the HIV target and subsequently added to the monomer mixture. Each Au nanoparticle had approximately 100 capture probes. Gel electrophoresis (Bio-RAD Laboratories, USA) and dynamic light scattering (DLS) (Zetasizer, Malvern UK) studies were performed to ascertain aggregation for both Y-DNA and AuNP-Y-DNA mixtures under different target and salt conditions.

Table 2: DNA sequences used for Y-DNA-pathogen detection

DNA STRAND	SEQUENCE
Y1 HIV 5'	CTCATTGATGGTCTCTTTTTTTTTGGATCCGCATGACATTCGCCGTAAG
Y2 HIV 5'	CTCATTGATGGTCTCTTTTTTTTCTTACGGCGAATGACCGAATCAGCCT
Y3 HIV5'	CTCATTGATGGTCTCTTTTTTTTAGGCTGATTCGGTTCATGCGGATCCA
Y1 HIV 3'	TGGATCCGCATGACATTCGCCGTAAGTTTTTCAATCTATCCCATTCTGC
Y2 HIV 3'	CTTACGGCGAATGACCGAATCAGCCTTTTTTCAATCTATCCCATTCTGC
Y3 HIV 3'	AGGCTGATTCGGTTCATGCGGATCCATTTTTCAATCTATCCCATTCTGC
HIV target (50 bp)	TGTTAAAAGAGACCATCAATGAGGAAGCTGCAGAATGGGATAGATTGCAT
5' HIV capture probe for AuNP	TTCCTCATTGATGGTCTCTTTTAACA TTTTT /3ThioMC3-D/
3' HIV capture probe for AuNP	/5ThioMC6-D/ TTTTT ATGCAATCTATCCCATTCTGCAGC
InfA (mismatched target)	GACCAATCTTGTCACCTCTGACTAAGGGAATTTTAGGATTTGTGTTCACGCT

For the DLS and gel studies, the Y-DNA and AuNP's were prepared separately to

final concentrations of 13.3 nM and 39.5 nM, respectively. Target concentrations used in gel electrophoresis measurements were ~1 μM. Such target concentrations (~1 μM) were used to ensure a clearly detectable signal.

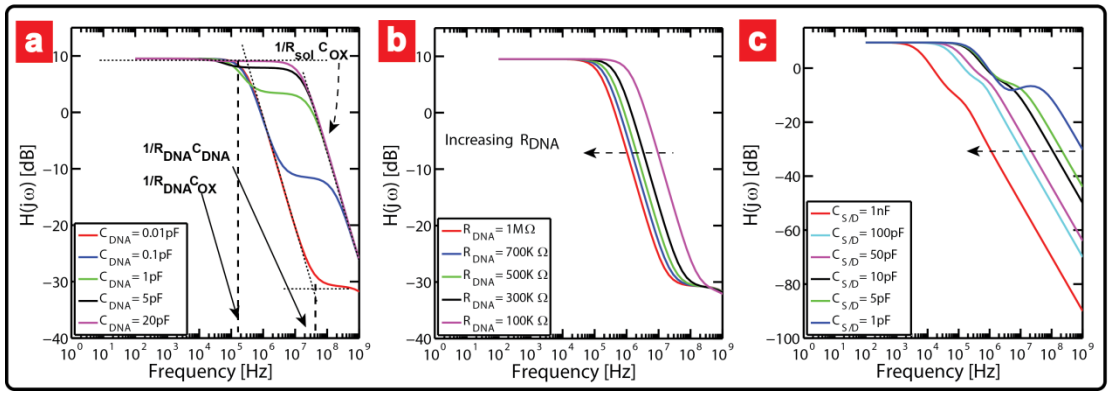

Figure 19: SPICE simulations of CvMOS with DNA immobilized. (a) P1 is less affected by the capacitance of DNA whereas Z1 shifts significantly. (b) Change in interfacial resistance causes a parallel shift in P1. (c) Increasing the S/D line parasitics limits the overall operational bandwidth.

RESULTS AND DISCUSSION

A. Simulating the Frequency Response of the CvMOS

We first simulated the frequency response of the CvMOS in SPICE including physical descriptions for the double layer, the DNA layer and surface hydroxyl ionization[24, 25]. We set $R_{sol} \sim 5K\Omega$ including the additional reference electrode resistance as well. C_{CG} and C_{SG} were chosen as 1pF and 20pF, respectively, for the illustration of the pole-zero responses. From the frequency response, we observed that the first zero (*z1*) is critically dependent on C_{DNA} while the first pole (*p1*) was highly sensitive to R_{DNA} [Fig. 19(a&b)]. We corroborated the effect of bulk resistance by varying the background electrolyte concentration [Appendix D, Fig. 41] and found a clear inward shift of *p1* as resistance increased. We also noticed a clear cut-off in frequency

response as the solution resistance increased, indicating an increased input resistance effect [Appendix D, Fig. 41]. This result agreed well with inferences drawn from previous efforts[31]. The source/drain line capacitances, due to long metal leads and pad capacitances, can also play a role in determining the overall bandwidth and impedance of the circuit[31]. This is because increasing the source/drain parasitics directly affects the frequency response [Fig. 19(c)] by introducing additional poles and zeros. This parasitic can have a severe consequence on the overall bandwidth of the transducer if not considered carefully[33]. Another pertinent aspect is C_{SG} and subsequently area scaling. One might expect that as the SG area is reduced, which becomes relevant when dealing with low concentrations of target analyte especially during potentiometric readout, *p1* would be affected dramatically. However, since the effective oxide capacitance is decided by C_{CG} in parallel with the series combination of $C_{SG} // C_{tun}$, i.e. $C_{OX} = \frac{(C_{tun} + C_{CG}) \times C_{SG}}{(C_{tun} + C_{CG}) + C_{SG}}$, continuous scaling of the SG area will not affect *p1* dramatically. On the contrary *p1* will instead be more sensitive to the parallel branch of C_{CG} (Appendix D, Fig. 42). As depicted in (Appendix D, Fig. 42), scaling C_{CG} did not affect the position of *z1*. The *z1* would however be affected by C_{SG} since the overall R_{DNA} and C_{DNA} will scale accordingly. This aspect of C_{CG} scaling is particularly important. In order to impart control over the channel and ensure low operating voltages, C_{CG} should be larger than C_{tun}, i.e., ensure a high coupling ratio, but this can limit the bandwidth of the impedance response. Hence this presents a design tradeoff between quasi-static and AC operations. We do point out

although these simulations roughly highlight the overall RC behavior of the static molecular layer, they do not capture the frequency dependent nature of molecular relaxations. In order to incorporate relaxation mechanisms, more involved theories including dipole moments and shape-dependent relaxation time constants need to be considered[41]. However, due to the non-homogeneous shape and size of the resulting DNA aggregates, an analytical model will be difficult. This aspect is under further investigation.

B. Y-DNA Aggregation and the Effect of AuNP's

We first performed gel-electrophoresis measurements on the Y-DNA monomers under different conditions to observe the hybridization of Y-DNA monomers and ssDNA pathogen target (HIV). We observed a large smear [Fig. 20(a)] when target pathogen strands were added, indicating a large distribution in aggregate size. In the absence of target, the loaded sample was observed to clearly migrate across the gel without any smear indicative of un-hybridized Y-DNA monomers. Similar effects were observed with mismatched target (Influenza A- InfA) or with the addition of target alone. We further analyzed the size differences and morphological changes of these aggregates during hybridization by DLS. DLS studies showed a clear increase in size with aggregates approaching ~15 nm in diameter within 20-30 minutes of target addition [Fig. 20(b)] to Y-DNA monomer solutions. On the other hand, when 15 nm diameter AuNP's coated with ssDNA capture probes were additionally added to the Y-DNA monomers mixture, the aggregate sizes increased dramatically upon target addition (~800 nm). Gel electrophoresis in the presence of AuNP's showed a clear difference

between target-treated and untreated samples [Fig. 20(c)]. Target-specific samples that formed aggregates were trapped in the well while un-hybridized fragments (no target or non-specific target) that were unable to form an aggregate migrated into the gel. The effect of mismatched target addition and varied background salinity was also investigated. We observed that under mismatched target treatment the AuNP-Y-DNA monomer mixture migrated into the gel. Compared to the hybridization experiments performed in 500 mM NaCl, a reduction in background salinity to 60 mM and 10 mM lowered the aggregation and hence hybridization efficiency, with the sample appearing to smear across the gel and periodic bands beginning to appear under a ~10 mM background saline concentration. These bands are aligned with aggregates having different number of AuNP's. Furthermore DLS measurements were performed on mixtures containing AuNP's and Y-DNA monomers in the presence of pathogen [Fig. 20(d)]. We found a clear increase in aggregate size upon target addition within minutes, with a near 40-fold increase in size (diameter ~ 800 nm) when compared with Y-DNA monomers alone [Fig. 20(b)]. Together the results suggest that AuNP functionalized probes increase the target binding probability due to the increased capture probe surface density.

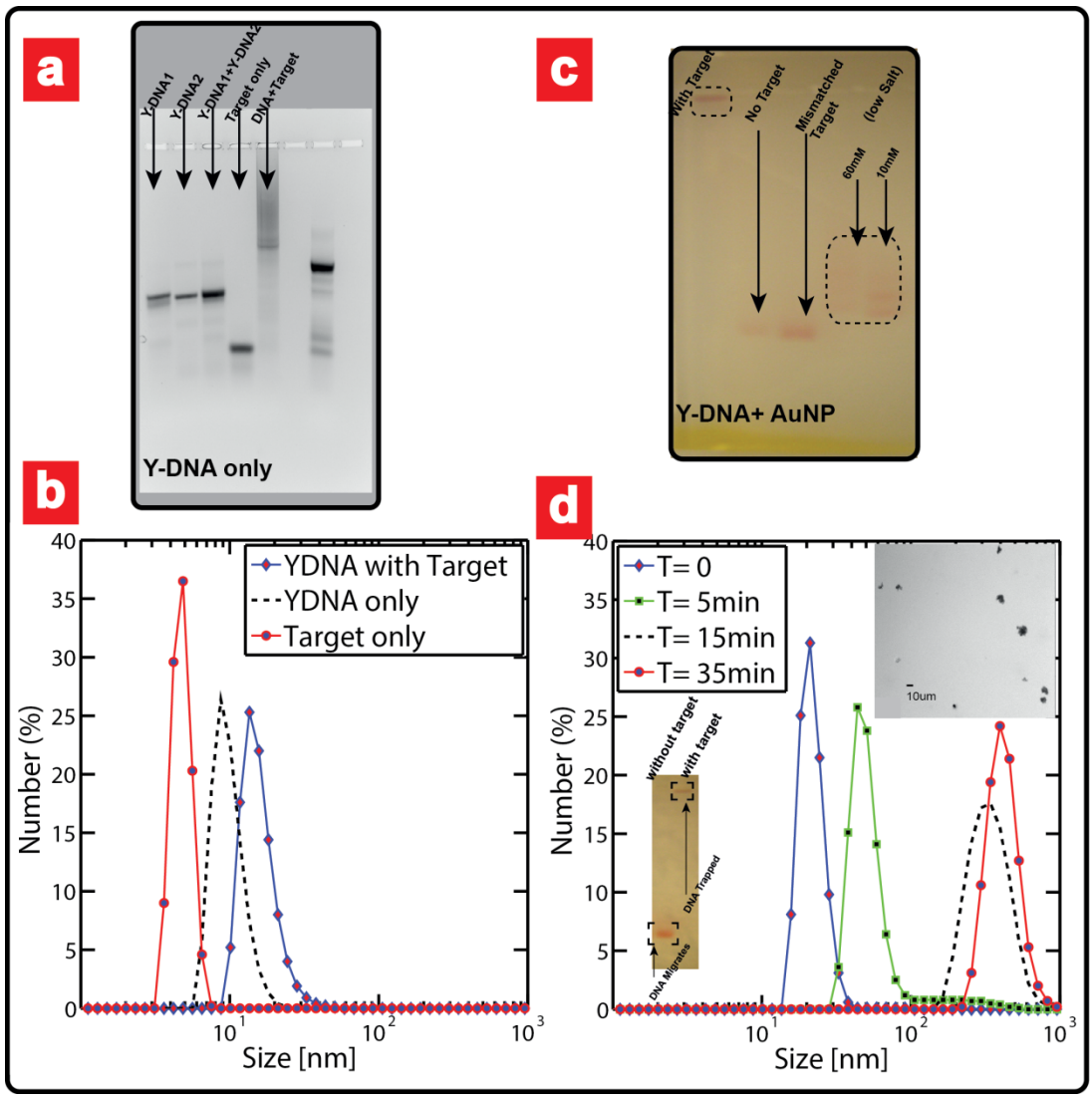

Figure 20: (a) Gel electrophoresis of Y-DNA aggregation show a large smear as pathogen is added, indicating aggregation of DNA fragments. Absence of target results in a clear run across the gel. (b) DLS study of Y-DNA- aggregation shows a time-dependent increase in aggregate size reaching ~15 nm. (c) Gel electrophoresis study of Y-DNA-AuNP aggregation shows fragments stuck with target present confirming increased size. Absence of target or addition of mismatched target shows little aggregation. Lowering in background salinity reduces aggregation. (d) DLS measurement of the Y-DNA-Au-NP mixture after target treatment. Notice the increase in cluster size to ~100 nm-700 nm within minutes of pathogen target addition. Inset, upper right: SEM image shows cluster size, (scale bar 10 μm); Inset, lower left: Gel electrophoresis shows DNA and Au nanoparticle aggregates stuck in well after target treatment.

C. CvMOS Frequency Response to Y-DNA Aggregate Addition

Y-DNA monomers were first exposed to target pathogen in a solution phase and allowed to hybridize. The mixture was subsequently added to PLL-functionalized

CMOS chips. It is important to note that since the SG is large, the double layer polarization is not a dominant factor in the frequency response and rolls off at frequencies ~100-500 Hz. The impedance of the system is then highly sensitive to the

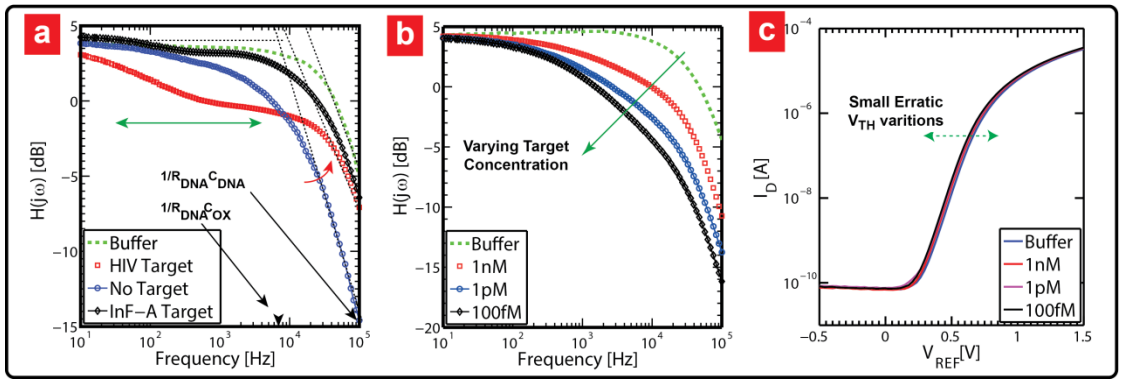

Figure 21: (a) Frequency response of Y-DNA-target hybridization. Buffer represents 500 mM saline without Y-DNA. Addition of Y-DNA without target increases RDNA. Notice a clear relaxation in the presence of target (green horizontal arrow). The red arrow indicates the second pole formation. Addition of a mismatched target (InFA) pushes the pole out in comparison to no target added. This suggests reduced interfacial resistance possibly due to non-specific binding between Y-DNA monomers and the target strand. Time constants depict the dependence on CDNA and RDNA. (b) LoD for Y-DNA mixtures shows an increase in RDNA as target concentration decreases, corresponding to low aggregate count and increased surface coverage by un-reacted monomers. (c) Quasi-static I-V response measured from the reference electrode. Notice the small and erratic shifts in V_{TH} as a function of increasing target concentration, limited by screening under high saline conditions.

bulk properties of the fluid. As shown in [Fig. 21(a)] when pure buffer was introduced, *p2*, which now was the dominant pole in the system, occurred at approximately 20 KHz. This experiment served as a blank test. When Y-DNA monomers samples treated with pathogen were introduced, we immediately observed a relaxation (indicated by green bi-directional arrow) with *p1* and *z1* occurring as early as 50-60 Hz and 500 Hz, respectively, attributed to molecular relaxations. On the contrary *p2* moved out back to ~20 KHz indicating a reduced interfacial resistance. In comparison, Y-DNA monomers samples without target treatment showed no relaxation characteristics indicated by no formation of *z1*. The overall bandwidth decided by *p2*

occurred at ~10 KHz indicating increased solution and interface resistance. The Y-DNA monomer mixture with the addition of mismatched targets expressed a very weak relaxation with *p1* and *z1* occurring around 100Hz and 1 KHz, respectively. Here however *p2* moved in and occurred at ~10 KHz indicating an increase in bulk resistance in comparison to pure buffer. Nonspecific binding due to partial match of the base pairs with the capture probes could have caused a slight increase in aggregate size and hence the minor relaxation with mismatched target addition. With both controls however an increase in interfacial resistance was still observed. This resistive effect was further studied as shown in [Fig. 21(b)]. As the background target concentration was increased, the DNA resistive effect decreased with aggregate formation which depleted free Y-DNA for surface coverage. This resulted in enhanced signal gain at higher frequencies. In contrast, under the same saline conditions (500 mM), the potentiometric (quasi-static) measurement showed a small erratic response in ψ_O to what is normally expected with negatively charged DNA immobilized on the surface, clearly indicating a screening limited response [Fig. 21(c)].

Figure 5 depicts the ex-situ TF in which the baseline (i.e. the buffer) is subtracted from the measured impedance to highlight the molecular relaxation effects. The magnitude under different target conditions (i.e. no target, with correct target and mismatched target (InFA) at ~1 μM to ensure aggregate formation) shows a slight trough [Fig. 22(a)] at around 1 KHz with target present and around 70 KHz with the addition of mismatched target. This clearly indicates that the approach can clearly discern between samples with target present and absent. The trough represents the maximum

difference in signal with respect to the buffer, attributed primarily to polarization induced effects due to resistance.

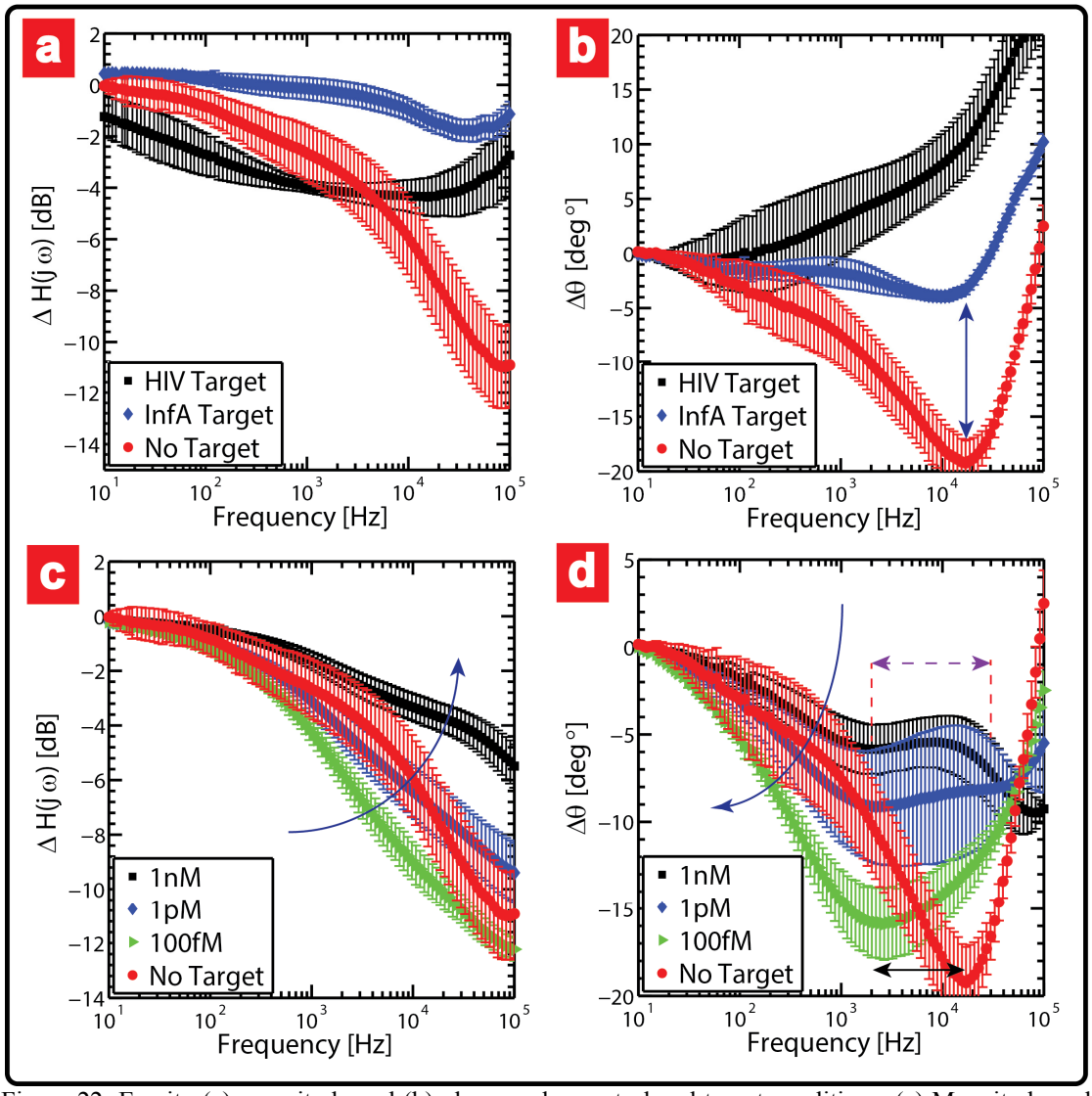

Figure 22: Ex-situ (a) magnitude and (b) phase under control and target conditions. (c) Magnitude and (d) phase under varying target concentration with the total Y-DNA concentration fixed at 6.6nM. At low target concentrations, p1 is determined by the unreacted monomers. As target concentration increases (arrow in (c)), aggregate formation reduces RDNA and p1 moves out. A relaxation is subsequently observed (purple dotted arrow in (d)), indicative of increased polarizability due to aggregates. Large arrow in (d) indicates decreasing order of concentration. The baseline solution response is subtracted to show the difference.

With target absent the trough appeared to occur at frequencies beyond 100 KHz which

was also observed in the phase change as well [Fig. 22(b)]. In the magnitude response attenuation was more pronounced with target absent. We attribute this to the fact that the impedance is dominated by a large density of un-hybridized monomers in the electrolyte resulting in an increased interfacial resistive change.

The observation of a trough or peak in the magnitude further suggests a frequency dependent molecular relaxation. It is important to note that relaxation in this frequency range is mainly attributed to molecular weight and size[42]. It is well known that DNA possesses a quasi-permanent dipole moment[42] due to the counterion cloud in solution. The counterion relaxation can manifest in two ways: a) the loosely bound diffuse ion layer of which forms a quasi-permanent dipole with the DNA molecule can stop responding to the AC frequency in the form of an end-to-end movement[29] which is known to occur in the 10 Hz – 10 KHz range, and b) the tightly bound condensed counterions which form dipoles with the phosphate backbone reveal a dispersion in the 10 KHz to 1 MHz range. These relaxations manifest as a shift in overall permittivity[41, 43] (real and imaginary) which in turn affects the impedance[44]. In the present study this change in permittivity is amplified by aggregation when the target of interest is present. In a separate study (not shown) we ascertained this increased molecular weight effect by linearly varying the length of the DNA chain and found a clear length dependent time constant of relaxation in the impedance spectra.

In Fig. 22 (c & d), we depict the net effects of varying target concentrations from 100 fM to 1 nM on aggregation and relaxation and compare the response to when targets are absent from the mixture. The magnitude and phase revealed molecular relaxations

in the 1 - 10 KHz range. As the target concentration increased, the net resistive effect decreased and capacitive effect (relaxation) began to appear, indicated by slight relaxation in [Fig. 22(c)]. Correspondingly the phase plot also depicted an oscillation, indicated by dotted arrow in [Fig. 22(d)] suggesting that a relaxation did indeed occur. A clear difference in relaxation peaks between a 100 fM target concentration and target-less samples clearly indicates the possibility of detecting very low concentrations of pathogen. The relaxations in the response highlighted by oscillations in the Bode plot suggest that maximal aggregate formation occurs when Y-DNA/target DNA ratios are approximately 1:1. Any further increase in target concentration can potentially lead to an impedance response dominated by the un-hybridized excess target DNA. Given the statistical significance of the data and taking both magnitude and phase into consideration, the limit of detection (LoD) was found to be between 100 fM and 1 pM.

D. CvMOS Frequency Response to AuNP-Y-DNA Aggregate Addition

In order to further increase the LoD, we added ssDNA capture probe functionalized AuNP to the Y-DNA monomers mixture and ascertained its effect on aggregate formation and the impedance response. As shown in Fig. 23(a), upon varying the target concentrations we immediately noticed a clear relaxation with a distinct trough, even for target concentrations as low as 100 fM. Target concentrations below a 100 fM did not reveal such a response (not shown). This is in stark contrast to when target is absent. When targets bind to capture probes, it induces an immediate increase in AuNP and Y-DNA clustering which subsequently sediments down onto the SG

interface and thereby increase the local polarization and resistance. Addition of AuNP's amplifies the molecular size of the aggregates and thereby increases the polarizability by attracting more counterions, and in turn influences the rotational relaxation behavior through a change in the quasi-permanent dipole moment[29, 41, 44] , which results in a distinct relaxation.

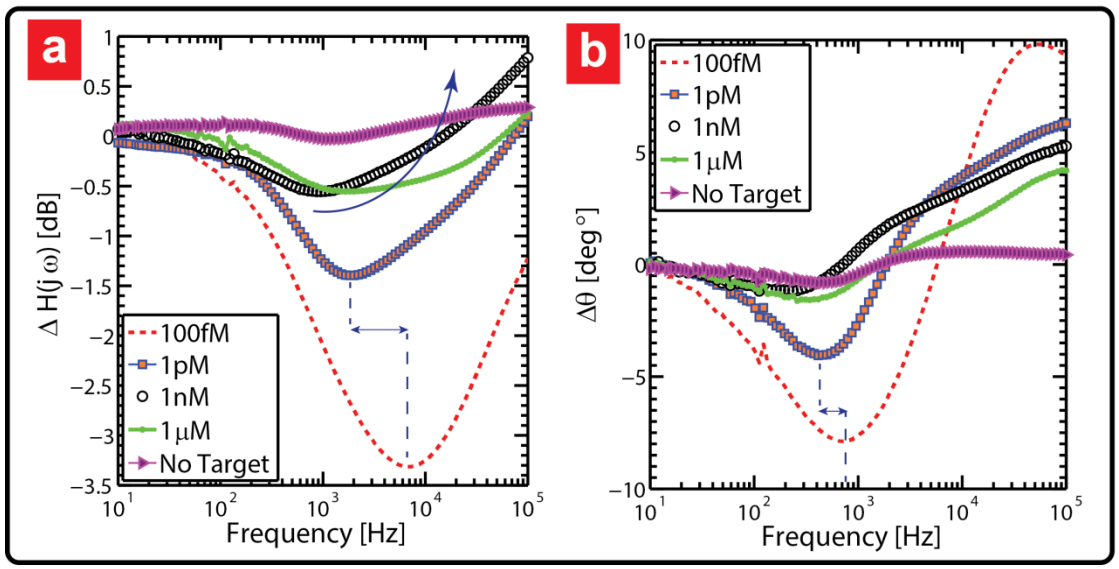

Figure 23: Ex-situ transfer function with added Au-NP probe amplifying agents in addition to Y-DNA. Ex-situ (a) magnitude and (b) phase difference under varying target concentrations for Y-DNA monomers with additional AuNP tags. The p1 – z1 response occurs at lower frequencies, indicative of larger aggregate size and a more pronounced shift in the relaxation time constant. A relaxation is observed even for 100 fM target concentrations (red).

At low target concentrations, small linear fragments of target-monomer formations most probably form instead of large aggregates leading to an increased resistive effect. We reiterate that the impedance response is most sensitive to the interfacial properties primarily because SG is large and the double layer polarization rolls off quickly with frequency. When the target concentrations were further increased, the attenuation in magnitude slowly decreased (suggestive of reduced background resistance) and the trough in magnitude moved to lower frequencies indicative of increasing time

constants possibly due to larger aggregate size and shape of fragments. In Fig. 23(b), the phase once again showed a clear oscillation corresponding with the trough in magnitude [Fig. 23(a)], which strongly suggested that the transistor was picking up molecular relaxations. A secondary peak occurred at frequencies beyond 100 KHz (Appendix D, Fig. 43). We also compared the relaxation characteristics of AuNP's and Y-DNA monomers in the absence of target and presence of mismatched targets (Appendix D, Fig. 44) and found a clearly discernible difference in both magnitude and phase. In the absence of target, there was no peak or trough observable. However, with addition of mismatched target a peak began to appear with relaxation time constant beyond the detectable range. We attribute this behavior to possible non-specific binding between the InfA target and the Y-DNA monomers-AuNP mixture. The effect of background salinity was also studied (Appendix D, Fig. 44). The low frequency trough disappeared as salinity reduced and shifted to higher frequencies, indicating less aggregate formation. Figure 45 (Appendix-D) depicts the magnitude of the overall TF before the baseline saline solution was subtracted, which clearly shows *p1* and *z1* formation when the targets were introduced.

One important point to note is that the Y-DNA scheme without target had a large increase in interfacial resistance with troughs occurring at fairly high KHz frequencies [Fig. 22(a)]. This suggested that the dominant cause of a large interfacial resistance was the free Y-DNA monomers in solution. With AuNP's and Y-DNA mixed together, in the absence of target, we observed a lowering in interfacial resistance across the frequency range swept (10 Hz - 102 KHz). This clearly suggests that the interfacial resistance in this case is dominated by the AuNP and not the Y-DNA,

possibly due to intermolecular repulsion, steric effects, and the AuNP concentration in comparison to that of the free Y-DNA monomers. Such an effect was also observed in a previous study on ISFET's with AuNP amplifying agents[27].

CONCLUDING REMARKS

We successfully carried out transistor-based impedimetric detection of pathogenic DNA with signal amplification achieved by branched Y-DNA self-assembly under high saline conditions, which is a pre-requisite for nucleic acid hybridization but is traditionally not compatible with most common electrochemical approaches. Branched Y-DNA monomers tagged with 3' and 5' capture probes hybridize with ssDNA targets, culminating in rapid aggregation without the need for using specific enzymes or precise thermal control. The reaction proceeds rapidly within minutes of target addition at room temperature due to the kinetics of solution phase hybridization. In addition the aggregates dispensed on the sensing gates of CνMOS transistors show a clear distinction in both the magnitude and phase of the frequency response. A split-signal delivery method using the independent gates of the CνMOS transistor is presented. The AC perturbation is fed via the fluid reference electrode and the DC bias through the CG electrode. A trough/peak in signal amplitude and phase is observed with aggregates present and is explained by interface polarization and molecular relaxations. These relaxations are found to be highly dependent on the extent of molecular size amplification and polarization increase. AuNP tags coated with ssDNA capture probes were additionally used to enhance the LoD to about ~100 fM by

increasing the aggregate size. These combined results suggest a highly sensitive and specific DNA recognition method, which is enzyme-free, thermal-cycle-free, and fluorescent-label-free on a fully CMOS-compatible electronic platform.

Supplemental Information: Supplemental information accompanies this chapter, refer Appendix D.

REFERENCES

[1] P. Yager, G. J. Domingo, and J. Gerdes, Annual Review of Biomedical Engineering **10**, 107 (2008).

[2] M. R. Hartman *et al.*, Nanoscale (2013).

[3] J. P. Allain, Clinical & Laboratory Haematology **22**, 1 (2000).

[4] P. Craw, and W. Balachandran, Lab on a Chip **12**, 2469 (2012).

[5] A. Niemz, T. M. Ferguson, and D. S. Boyle, Trends Biotechnol. **29**, 240 (2011).

[6] S. Yang, and R. E. Rothman, The Lancet Infectious Diseases **4**, 337 (2004).

[7] R. M. Dirks, and N. A. Pierce, Proc.Natl.Acad.Sci. U.S.A. **101**, 15275 (2004).

[8] C. Duarte *et al.*, Biomed. Microdevices **15**, 821 (2013).

[9] X. Zhi *et al.*, Biosens. Bioelectron. (2013).

[10] J.-M. Nam, C. S. Thaxton, and C. A. Mirkin, Science **301**, 1884 (2003).

[11] M. R. Hartman *et al.*, Angew. Chem. Int. Ed. **52**, 8699 (2013).

[12] J. B. Lee *et al.*, Nanoscale **2**, 188 (2010).

[13] Toumazou C *et al.*, Nature methods **10**, 641 (2013).

[14] G. L. Damhorst, N. N. Watkins, and R. Bashir, Biomedical Engineering, IEEE Transactions on **60**, 715 (2013).

[15] E. D. Goluch *et al.*, Lab on a Chip **6**, 1293 (2006).

[16] M. A. Burns *et al.*, Science **282**, 484 (1998).

[17] R. Bashir, Advanced Drug Delivery Reviews **56**, 1565 (2004).

[18] R. S. Gaster, D. A. Hall, and S. X. Wang, Lab on a Chip **11**, 950 (2011).

[19] F. B. Myers, and L. P. Lee, Lab on a Chip **8**, 2015 (2008).

[20] G. Damhorst *et al.*, Biomed. Microdevices **15**, 895 (2013).

[21] C.-S. Johnson Hou *et al.*, Lab on a Chip **7**, 347 (2007).

[22] J. Go *et al.*, ACS Nano **6**, 5972 (2012).

[23] A. Tarasov *et al.*, ACS Nano (2012).

[24] K. Jayant *et al.*, Phys.Rev.E **88**, 012801 (2013).

[25] K. Jayant *et al.*, Phys.Rev.E **88**, 012802 (2013).

[26] B. Veigas *et al.*, Biosens. Bioelectron. **52**, 50 (2014).

[27] Y. Han, in *Institut of Bio- and Nanosystems* (Forschungszentrum Jülich, Forschungszentrum, Zentralbibliothek, 2006), p. 173.

[28] A. Ebrahimi *et al.*, Lab on a Chip **13**, 4248 (2013).

[29] E. Salm *et al.*, Biomed. Microdevices **13**, 973 (2011).

[30] M. Yi, K.-H. Jeong, and L. P. Lee, Biosens. Bioelectron. **20**, 1320 (2005).

[31] S. Ingebrandt *et al.*, Biosens. Bioelectron. **22**, 2834 (2007).

[32] G. S. Kulkarni, and Z. Zhong, Nano Lett. **12**, 719 (2012).

[33] T. C. Nguyen *et al.*, Phys. Status. Solidi A **210**, 870 (2013).

[34] R. GhoshMoulick *et al.*, Phys. Status. Solidi A **206**, 417 (2009).

[35] E. Katz, and I. Willner, Electroanalysis **15**, 913 (2003).

[36] A. B. Kharitonov *et al.*, J.Phys.Chem.B **105**, 4205 (2001).

[37] Y. Li *et al.*, Nature Materials **3**, 38 (2003).

[38] N. Y. M. Shen *et al.*, IEEE Trans. Electron Devices **50**, 2171 (2003).

[39] T. Shibata, and T. Ohmi, IEEE Trans. Electron Devices **39**, 1444 (1992).

[40] W. Cheng, S. Dong, and E. Wang, Langmuir **19**, 9434 (2003).

[41] S. Tomić *et al.*, Phys.Rev.E **75**, 021905 (2007).

[42] R. Pethig, and D. B. Kell, Physics in Medicine and Biology **32**, 933 (1987).

[43] S. Takashima *et al.*, Biophys. J. **46**, 29 (1984).

[44] R. Holzel, Nanobiotechnology, IET **3**, 28 (2009).

CHAPTER-6: NON-FARADAIC ELECTROCHEMICAL DETECTION OF EXOCYTOSIS FROM MAST AND CHROMAFFIN CELLS USING FLOATING-GATE MOS TRANSISTORS

CHAPTER OVERVIEW

We present non-faradaic electrochemical recordings of exocytosis using multi-input floating-gate MOS transistors on a population of mast and chromaffin cells. Termed the chemoreceptive neuron MOS (CνMOS), the transistor features independent control (CG) and sense gates (SG) coupled to a common extended floating gate (FG). In comparison to conventional ion-sensitive field-effect transistors (ISFET), the CνMOS allows the quiescent point to be independently controlled and physically isolates the transistor channel from the electrolyte which is critical for stable long-term recordings. We first measured exocytosis from a population of RBL-2H3 mast cells mediated by IgE and its high-affinity cell surface receptor FcεRI using the antigen DNP-BSA. Quasi-static I-V measurements reflected a slow shift in surface potential (ψ_O) upon stimulation which was found to be strongly dependent on extracellular calcium ($[Ca]_o$) and buffer strength, suggesting that the transistor response was sensitive to protons released during exocytosis. Unsensitized cells showed no response to antigenic

stimulation. Fluorescent imaging of dextran-labeled vesicle release performed separately showed evidence of a similar time course after stimulation, further indicating that the transistor was recording a coupled stimulus-secretion effect. High-resolution transient recordings revealed ψ_O fluctuations with a rapid rise and slow decay indicative of weak surface re-equilibration. Extending the study to bovine chromaffin cells, we observed a gradual change in ψ_O as well as rapid ψ_O current fluctuations in the transient response to KCl stimulation, suggesting the presence of both action potentials (AP) and surface charging due to vesicle release. The extracellular AP response comprised of both biphasic and inverted capacitive waveforms indicative of varying ion channel distributions across the cell membrane and the cell-transistor junction. Our approach presents a facile route to realize non-redox based biosensors in commercial CMOS, capable of detecting chemically active or inactive hormones, neurotransmitters and ion channel currents with minimal invasiveness and localized sensitivity control.

INTRODUCTION

Synaptic transmission and cell to cell communication in the human body are frequently characterized by the release of charged hormones and transmitters from secretory vesicles or granules which impinge on specific receptor molecules expressed on the target cell [1-3]. Depending on the excitable nature, cells respond to these chemical inputs through release of granules containing specific compounds or inducing an electrical wave such as an action potential (AP). The mechanism of

vesicle fusion with the cell plasma membrane upon stimulation and subsequent release of the granular contents (i.e. in the form of quanta) into the extracellular environment is termed exocytosis[4]. When measured electrochemically such release events reveal a distinctive temporal response [5]. Exocytosis recordings are also often employed to characterize the mechanism of drug action on cells. For example, amperometric recordings have shown that the Parkinson's drug L-Dopa increases the quantal size [6], i.e. the total released charge increases, a consequence of increase vesicle size. There is thus a need to develop high throughput, scalable and multi-functional electronic instrumentation in order to characterize the action of various pharmacological inhibitors, toxins and stimulants on vesicle release. Transmitter and granular release can be specifically stimulated or inhibited depending on the cell type under study. In neurons, electrical excitations in the form of action potentials (AP) propagate along the axon and stimulate neurotransmitter release in the region between the axon terminus of the pre-synaptic neuron and the dendritic spine of the post-synaptic neuron [Fig. 24(a)] called the synapse. The released transmitters impinge on specific receptors on the post-synaptic neuron exciting or inhibiting action potential generation. In immune cells such as mast cells on the contrary, exocytosis can be induced through a receptor effector function where a specific antigen receptor interaction causes a signal cascade within the cell, culminating in the release of mediators and hormones which causes an allergic response. The released compounds from mast cells impinge on cells expressing specific receptors (such as the histamine receptor on smooth muscle cells) [Fig. 24(c)] and elicit a downstream response. In this study we seek to create a CMOS sensor capable of detecting granule release from mast

cells. We then extend the approach to measuring depolarization induced activity from chromaffin cells where it can function as an electronic post-synaptic sensor [Fig. 24(d)]. Thus the transmitter-receptor stimulated signaling or electrical excitation is replaced by an electronic biosensor. Such a system not only provides a test bench for fundamental studies of exocytosis by monitoring release from vesicles and action potential's with high temporal resolution. This is paramount in understanding cellular kinetics and establishing rapid screening procedures. It also sets a promising route towards future artificial synapse systems and ionic-electronic interfacing circuitry.

Current methods of monitoring exocytosis include fluorescent techniques [1, 4, 7], and carbon-fiber amperometry [5, 8, 9]. Fluorescence techniques often require labels and sophisticated optics, which increases the complexity of the experiment. On the other hand, amperometry may be prone to noise due to low current levels involved, relies on faradaic chemistry for detection, and is challenging to miniaturize in terms of pixel density, although recent efforts have resulted in significant improvements [10-13]. Non-faradaic transistor-based measurements on the contrary extend the detection capability to chemically inactive molecules, are extremely sensitive to surface adsorption, record cellular signals with a high degree of temporal sensitivity, present a naturally occurring high impedance node due to the gate oxide and can render sub-cellular spatial resolution [14-17] with very low input referred noise characteristics [18]. Previous work on transistor-based cellular sensing has primarily focused on recording electrical activity from excitable cells such cardiac myocytes [19, 20] and nerve cells [18, 21]. Recently Stern and co-workers [22] extended transistor based sensing to detect antigen-stimulated T-cell activation detection by CMOS-compatible

semiconducting nanowire sensors.

The cell-ISFET interface has been widely investigated in the past [17, 23-26]. Typically the cell forms a high impedance seal at the transistor interface and the voltage within the cleft acts as a secondary gate input to the transistor. Changes in ionic activity sets up a potential within the cleft which capacitively influences the transistor output [16], while chemical changes at the transistor surface such as pH or molecular binding directly influence the net surface charge [27]. Limitations of this approach include the lack of independent control over the transistor's operating point. Controlling the ISFET operating point is traditionally achieved by either re-biasing the reference electrode or through source barrier modulation [28], but applying a large voltage in solution across the cell-transistor interface from a reference electrode may potentially influence or even destroy the cell by electroporation. Also with cells directly immobilized on gate oxide, long-term drift associated with ion penetration into the active region is a serious issue which can potentially lead to current instabilities during measurement. Recent strides in CMOS technology, however allow the use of metal layers and vias to isolate the transistor channel from the sensing region which has shown promising results with very low drift [29]. One drawback, however, is that, top metal interfaces lack chemical specificity to ionic and molecular adsorption, unless specific functionalized coatings are used.

Another class of sensors uses nanowire/nanotube [17, 30] channels, as opposed to the ISFET's buried channel, which improves sensitivity due to enhanced electrostatic coupling. The transistor operating point, however, is still modulated by either the reference electrode or a global back gate, which sets a limitation on

sensitivity tuning for each individual transistor. This ISFET scheme further imposes restrictions on control circuitry integration. While there have been recent efforts towards creating independent local gate control [31] to achieve tunability during operation, a highly sensitive, stable, scalable and addressable transducing scheme is still to be demonstrated. In this work we demonstrate a fully CMOS compatible, extended floating gate transistor which serves as an electronic analogue of the downstream communication, i.e., the receptor induced signal cascade. The device permits independent bias control, decouples the sensing region from the active region to allow for independent scaling, and introduces simultaneous charge and impedance readout to record cellular activity.

Recently [32-35] we proposed a MOS sensor termed the chemoreceptive neuron MOS transistor (CνMOS). Inspired by the conventional neuron MOS structure [36] , CνMOS has two input gates: control gate (CG) and sensing gate (SG), coupled to a common floating gate (FG) through a 35nm interpoly oxide. FG is in turn capacitively coupled to the channel by a 10nm tunnel oxide [Fig. 24(e)]. The operating principle is based on weighted sum and threshold operations and the device is widely used in neuromorphic computation[37, 38]. The capacitive weighting of CG and SG determines the FG potential for the firing signal, i.e., the output drain current. The threshold voltage variability calibrated from the CG is thus a measure of the cell/SG interface condition. In comparison to conventional ISFET's, each CνMOS can be independently tuned to a desired region of operation and sensitivity using CG. This improves the reliability of recordings, offers new circuit optimization strategies and presents a more flexible biasing scheme in comparison to applying a significant

voltage across cells using the reference electrode. The asymmetric capacitive coupling of the CG and SG to the FG further leads to an inherent amplification scheme with high sensitivity to charge and capacitance variations at the SG interface, which can be simultaneously recorded. In addition to the transient current output under a constant bias condition with high temporal resolution, we also demonstrate the unique feature of monitoring the subthreshold region as an extremely sensitive parameter. Furthermore, the FG can be programmed with either holes (positive) or electrons (negative), which can further interact with the fluid to achieve ionic actuation and detection [34, 35], setting the stage for future all-CMOS artificial synapses. Charge injection can also be used for auto-zeroing and translinear operations [39, 40], which reduces the burden and complexity of the supporting signal conditioning circuitry required for large-scale integration. To demonstrate the efficacy of the CvMOS transistor as a non-invasive synaptic input, we chose to monitor exocytosis upon stimulation from non-excitable RBL mast cells and excitable chromaffin cells of the bovine adrenal medulla.

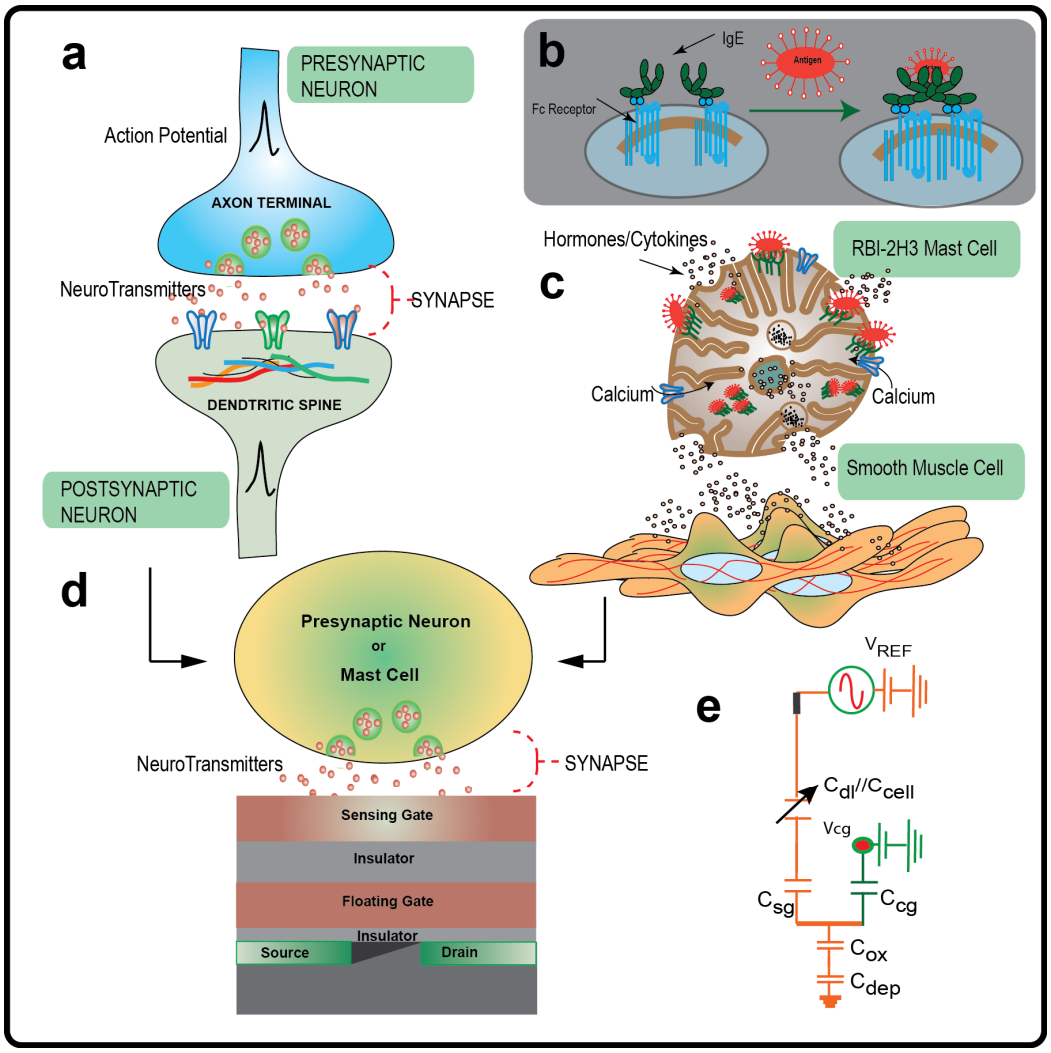

Figure 24: (a) Schematic of a neural synapse showing the post-synaptic and pre-synaptic nerve endings. An action potential in the pre-synaptic cell terminates with the fusion of vesicles and release of neurotransmitters (exocytosis) which impinge on the post-synaptic cell receptors. When the intracellular potential of the postsynaptic cell crosses a certain threshold the neuron fires inducing further electrical activity; (b) Cross-linking of the IgE upon antigenic stimulation, receptor clustering accelerates degranulation (c) Schematic of IgE sensitized mast cell degranulation by DNP BSA resulting in clear morphological change and hormonal release which subsequently stimulates smooth muscle cells through a receptor effector function (d) Replacing the post-synaptic neuron and smooth muscle cell with the CvMOS effectively creates a cell-transistor biosensor in which the SG effectively serves as an electronic analogue of a synapse and receptor respectively (e) Circuit schematic of the CvMOS transistor with capacitively coupled control (CG) and sensing gates (SG) to a common floating gate (FG). The CG and SG serves as threshold weights and after a certain threshold (V_{TH}) is reached the transistor turns on.

The rat basophilic leukemia cell (RBL-2H3) is a tumor cell line used frequently as an

experimental model for mucosal mast cells [7]. The release of inflammatory mediators from mast cells is the primary event in an allergic response [41]. These cells serve as a robust model for understanding the underlying biophysical and biochemical mechanism which couples signals originating at the membrane receptor with a biological effector function. Immunoglobulins of the IgE class serve as antigenic receptors which are anchored to cells via the membrane protein complex FcεRI. Upon stimulation with multivalent antigen, the receptors crosslink causing a signal cascade within the cell, which eventually culminates in the secretion of preformed mediators stored in the cellular granules. Mast cells form a specialized niche of the immune system, because the triggered cellular activity is immediate. Depending on the particular type of mast cells or basophil's, secretion occurs within seconds to minutes following the IgE cross linking step. Mast cells also provide a meaningful model for cell activation by an immunological stimulus, i.e., by an antibody-antigen reaction.

We further demonstrate the device detection capability using chromaffin cells as an excitable cell type to detect neurotransmitter release and related synaptic activity. The chromaffin cell allows us to study stimulus secretion coupling as mediated by both calcium entry and voltage gated channels, i.e., exocytosis induced by depolarization. Transistor recording of vesicle release from chromaffin cells [27] was demonstrated recently using open-gate ISFET's. The recorded signal was attributed solely to the change in the local pH across the double-layer interface which leads to protonation of the surface and hence a change in surface potential. In this work in addition to pH dependent signal generation mechanisms, we provide preliminary evidence suggesting direct molecular binding to the sensor surface as a signal generating mechanism.

MATERIAL AND METHODS

A. Cell Culture and Buffer Conditions

RBL-2H3 cells were maintained in a monolayer culture in Minimum Essential Medium, supplemented with 10% fetal bovine serum (Atlanta Biologicals, Norcross, GA), 1 ml/liter mito+ serum extender (Collaborative Biomedical Products, Bedford, MA), and 10 ~mg/ml gentamicin. Typically, cells were used in 3-5 days after passage. The cells were treated with IgE (2 μg/ml) for 1 hour at 37 ^{o}C and then re-suspended in tyrodes before dispensing them over native SG surfaces. Experiments were performed at 37 ^{o}C using variable pH buffer (HEPES) concentrations ranging between 5mM and 40mM in tyrodes solution. The cells were stimulated by multivalent antigen (DNP BSA (2,4 Dinitrophenyl Bovine Serum Albumin), Sigma) (1 μg/ml). The temperature was maintained through a carefully calibrated air blower. 1 μg/ml monovalent hapten was used to inhibit the degranulation, serving as a negative control.

Bovine adrenal glands were obtained from a local slaughterhouse and prepared as described elsewhere[42]. Prior to cell immobilization the chips were coated with 0.02% poly-l-lysine (Sigma) and used only within the first two days of cell preparation. Cells were suspended in ringer's solution containing 150 mM NaCl, 10 mM Hepes, 5 mM$CaCl_2$, 5 mM KCl, and 2 mM $MgCl_2$ (pH 7.25) (318 mOsm) and subsequently dispensed onto transistors . Ringer's solution (318 mOsm) with reduced sodium chloride (10%) and n-methyl-glucamine (NMG) (90%) were used to inhibit the occurrence of AP's. Cells were stimulated by adding high KCl (200mM) globally to the bath such that final KCl concentration was about 80~100mM. Experiments on

the chromaffin cells were performed at room temperature.

B. Fluorescent imaging of vesicle release

RBL-2H3 mast cells were loaded with 2 mg/ml FITC-dextran overnight, 200μM serotonin and sensitized with 1μg/ml IgE. On the following day, the cells were washed repeatedly with tyrodes-BSA before antigenic stimulation. A confocal microscope (Zeiss, Germany) with an immersion lens (60X, oil lens) was used for imaging. The temperature was maintained at 37ºC throughout the experiment using a combination of an objective heater and heated chamber.

C. Transistors , instrumentation and measurement setup

The chips were fabricated in a 1.5μm foundry CMOS (AMS) double-poly process with SG exposed and the rest of the chip covered with a 2μm polymer insulation. The first polysilicon layer forms the FG while the second polysilicon layer forms the CG and SG. The SG interface is exposed to bio-media while the CG is buried below insulation. The control oxide thickness (i.e. interpoly oxide) is 35nm, the tunnel oxide (i.e. between the FG and channel) is 10nm, and the capacitance ratio between SG and CG ($\frac{C_{SG}}{C_{CG}}$) ranges between 2 and 25 for various designs. SG areas on the chip ranges between $\sim 400\mu m \times 200\mu m$ to $\sim 400\mu m \times 5\mu m$ while the CG areas are $\sim 40\mu m \times 25\mu m$. The devices have an active channel area of $3\mu m \times 2\mu m$.

Three distinct measurement procedures were performed, quasi-static I/V sweeps for monitoring gradual changes in surface potential (ψ_O), high-resolution transient recordings of extracellular secretory activity, and impedimetric detection of the SG

interface. For I/V measurements, we used a semiconductor parameter analyzer (HP 4145 B) with the drain voltage (V_D) kept constant at 1V across all measurements. The transient measurements at a fixed CG bias was recorded by interfacing the transistor to a trans-impedance amplifier (TIA, Stanford Research Systems SR570, CA, USA) with a sensitivity ranging between $10\frac{\mu A}{V} \sim 100\frac{\mu A}{V}$, depending on the relative current magnitude, drift over time and the resolution of the data acquisition system (NI BNC 2110 and NI USB 6259). During transient analysis the signals were high-pass filtered at 1Hz unless specified and low-pass filtered at 3 KHz before sampling to reduce the aliasing effects. Further analysis and filtering was done through custom software. Before every measurement, the transconductance g_m observed from both the CG and SG was recorded in order to calibrate the sensitivity and accurately estimate ψ_O. For the devices used, g_m observed from the SG was found to range between ~0.01 – 0.3mA/V, limited by parasitics and interface characteristics after repeated cleaning and lysine addition. Impedance measurements monitored the small-signal transistor gain as a function of frequency. The AC sinusoid was supplied by a function generator (Stanford Research Systems DS345, CA, USA) through the Ag/AgCl reference electrode (Warner instruments, USA), while the DC bias (quiescent point) was set by the CG independently (Keithley 2400, USA). The transistor output was fed to a lock-in amplifier (LIA, Stanford Research Systems SR844, CA USA) through the TIA,

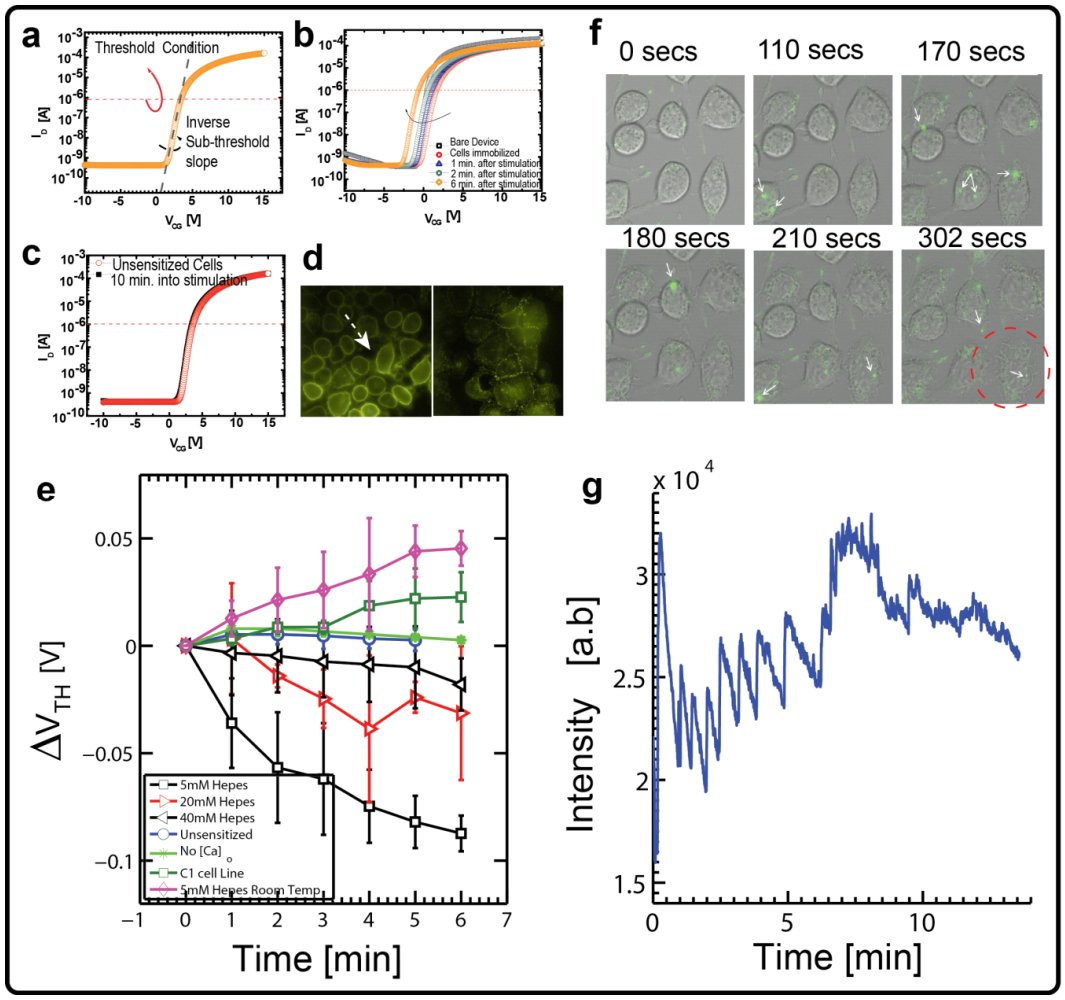

Figure 25: (a) Quasi-static IV response of the CvMOS operated from the CG. The V_{TH} is calibrated at constant current of 1μA, while the subthreshold slope is indicative of capacitance loading at the SG. (b) IV response to IgE sensitized mast cell degranulation upon antigenic addition. Notice a clear reduction in V_{TH} as degranulation proceeds with a more positive surface potential evolution. (c) Unsensitized cells show no shift in V_{TH} upon stimulation. (d) Fluorescent images of IgE sensitized mast cells (arrow) before (left) and after (right) stimulation. Clustering of IgE receptors is clearly observed along with morphological change. (e) Surface potential shifts as function of time after mast cell stimulation with DNP BSA under various conditions. Notice the effects of buffer, temperature and $[Ca]_o$. (f) Time lapse confocal imaging of FITC-dextran labeled mast cells after stimulation with DNP-BSA. FITC-dextran uptake occurs overnight. Fluorescence is quenched due to the low pH inside the vesicle. Upon release into the extracellular space the fluorescence recovers (green flash). The time stamps reveal a heightened detection of release events (white arrows) a few minutes after antigen addition. (g) Energy density indicative of fluorescent intensity for each subsequent time stamp indicates similar kinetics to (e).

hence monitoring the root-mean-square voltage V_{RMS} as a function of frequency. The sensitivity of the TIA was adjusted so as to avoid saturating the LIA input and was

operated under the high bandwidth mode.

CNMOS DETECTION PRINCIPLES

In CνMOS, the FG voltage (V_{FG}) is set by the weighted sum of the potentials across all its coupled capacitors (Eq. 1) [Fig. 24(e)]. The input gates have different overlap areas to the FG, which leads to capacitive amplification of the recorded signal. C_{gs}, C_{gd} and C_T are the FG-to-source capacitance, FG-to-drain capacitance and total capacitance on FG, respectively. Here Qrepresents the static charge stored on the FG. V_{SG} is additionally described as $(\psi_O - V_{REF})$ and reflects the change in surface charge through ψ_O.

$$V_{FG} = V_{CG} \times \frac{C_{CG}}{C_T} + V_{SG} \times \frac{C_{SG}}{C_T} + \frac{Q}{C_T} + \frac{C_{gs}}{C_T} \times V_S + \frac{C_{gd}}{C_T} \times V_D \qquad (1)$$

A small change in ψ_O causes the threshold voltage measured from the CG (V_{TH_CG}) to be scaled by the amplification factor $(\frac{C_{SG}}{C_{CG}})$. This parameter can be independently tuned with respect to the channel active area which sets the transconductance and frequency response. The nMOS transistor threshold voltage V_{TH} is usually at ~0.8V as measured from the FG, which is normally fixed in foundry. Independent CG control could help alleviate the need to set such large biases on the reference electrode but still maintain the transistor above V_{TH} and ensure high g_m . Furthermore, it can be used to overcome sensor mismatch by pixel level re-biasing or tunneling static charge on and

off the FG [34], reducing the need for complex global calibration circuitry [28].

Prior to every experiment, the reference electrode was used to calibrate the transconductance observed from the SG interface to extract the capacitive ratio. During the quasi-static and transient measurements the immobilized cells act as independent current sources i.e., they either secrete charge or give rise to ionic currents upon stimulation. Protons and molecules released during this secretory process can bind to the exposed hydroxyl groups on the SG surface and shift ψ_O. Ionic currents, however, in conjunction with the cell-transistor cleft resistance give rise to a transient voltage in the vicinity of the SG surface (V_J). A change in V_J modulates ψ_O which modulates V_{FG} and hence the output current. It is important to note that with non-faradaic detection the ionic charges of the secreted molecules are not consumed as opposed to the oxidation charge in amperometric detection but can transiently bind to the SG surface or remain within the cell-transistor cleft until they slowly diffuse out. Impedance spectroscopy monitors a shift in the cell's passive properties via the transfer function (see Appendix-E). Maintaining constant DC readout current through CG feedback enables pure capacitive detection, as V_{FG} is held constant.

RESULTS & DISCUSSION

A. Quasi-static measurements

Antigen-mediated cross-linking of FcεRI triggers degranulation in mast cells [43], which eventually results in vesicle release. Cyclic CG voltage sweeps were performed

to ascertain the shift in ψ_O upon antigen addition, as shown in [Fig. 25]. V_{TH} is defined for a constant current level of ($1\mu A$) [Fig. 25(a)]. The readout current and hence V_{FG} is re-calibrated to this defined level by modulating the CG bias. Any shift in ψ_O is then reflected by the change in CG bias required to achieve this constant current condition. For example with negative charge released, ψ_O reduces (i.e. surface becomes more negatively charged) which causes ΔV_{TH} to increase. The IV sweeps (*15 seconds duration*) indicate larger reductions in ΔV_{TH} for sensitized cells stimulated with DNP BSA compared to that of the unsensitized cells [Fig. 25(b&c)]. Under quasistatic conditions, the double-layer capacitance is large and $\Delta\psi_O$ drops mostly across the tunnel oxide as the FG-channel capacitance is the smallest [Fig. 24(e)]. Upon media and cell addition on SG, the subthreshold slope changes immediately in comparison to the bare surface [Fig. 25(b)]. This is due to the additional capacitance C_{cell} in series with C_{dl} between the SG and the reference electrode. However, static capacitive loading due to cell immobilization [Fig. 25(d)] or further movement upon stimulation shows no observable effects, reflected in the nearly unchanged subthreshold slope during the time course of secretion, which not only verifies device reliability but also indicates minute change in C_{cell} after immobilization and stimulation. Figure 25(e) summarizes ΔV_{TH} under various experimental conditions. We first stimulated sensitized mast cells under varying extracellular Hepes concentration in tyrodes buffer, by varying it from 5 to 40mM. We observed that after stimulation, ΔV_{TH} decreased (i.e. ψ_O becomes more positive) with time and showed a

clear buffer dependence. We explain this dependence as follows. Since the surface of the SG comprises of ionizable hydroxyl groups, the interface behaves like a buffer attracting hydrogen ions which bind to the exposed hydroxyl charge. The strength of the surface to accept hydrogen ions gives rise to the concept of "buffering capacity" and is strongly dependent on surface equilibrium constants, background salinity and surface site density[34]. Introducing a secondary buffer in solution, in this case HEPES, creates a competition with the surface buffering capacity to negate the surface sensitivity to hydrogen ions. From Fig. 25(e) this would suggest that the acidic environment of the vesicle contributes to variations in ψ_O. However, the reported signal cannot be totally attributed to pH fluctuations alone. This is because a positive ψ_O shift of approximately 50-60mV would imply a change of almost one pH unit in the electrolyte background [34]. Thus non-specific binding of preformed mediators and small molecules that are positively charged are believed to additionally contribute to the ψ_O shift. The signal generation mechanism in this case would be similar to when biomolecules bind to a transistor surface causing a shift in ψ_O of the order of 10's of milli volts[44]. Nevertheless since ψ_O became more positive with time after stimulation and was found to be dependent on the buffer concentration, the physical principle underlying signal generation suggests protonation of the SG interface as one important mechanism contributing to the response.

The absence of $[Ca]_o$ was found to suppress any shift in ψ_O even when cells were sensitized, which strongly suggested that calcium entry was an important

precondition to elicit a stimulation response. It is also well known that intracellular calcium oscillations are a pre-requisite for exocytosis to occur [45, 46] which will be diminished in the absence of $[Ca]_o$. Furthermore unsensitized cells showed no response upon stimulation, while B4A6C1 mutant cells which are known to weakly degranulate did not yield any appreciable change in ψ_O either. These observations together strongly asserted that the observed FET signals were indeed a consequence of granule exocytosis. An important condition imposed during the above study was the temperature of the experimental set up was regulated to be close to 37ºC. When we stimulated IgE sensitized cells at room temperature under low buffer conditions, the overall $\Delta\psi_O$ increased slightly with time rather than decrease [Fig. 25(e)], indicative of lower amounts of released "positive charge" and weak degranulation. While this result is promising as physiologically relevant temperatures are important for mast-cell exocytosis, the exact reason has not yet been established and requires further investigation. We hypothesize that slow extracellular calcium uptake in the cell transistor cleft is a possible contributing factor. We reason that depletion of cationic charges decreases C_{dl} in the cell-transistor cleft which leads to reduced screening of SG surface (i.e., "less screened" intrinsic hydroxyl charges on SG)which causes ψ_O to become more negative .

Confocal microscopy studies of FITC-dextran-loaded mast cells stimulated under identical conditions was performed to confirm the kinetic time scales of the transistor recordings. FITC-dextran, once taken up by the cell, is stored in its secretory vesicles. Due to the low pH within these vesicles, the FITC fluorescence is quenched. The

fluorescence intensity increases when exocytosis occurs as the pH of the secreted

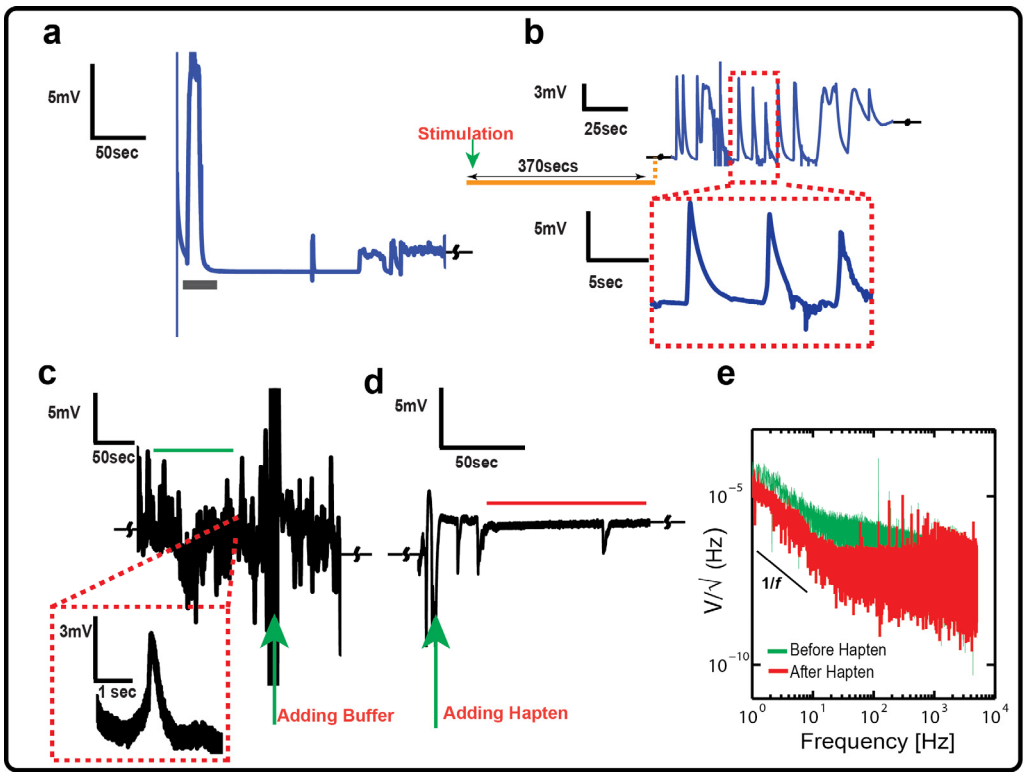

Figure 26: Mast cell transient responses: (a) Immobilized mast cells response to antigenic stimulation by DNP BSA in tyrodes solution. Antigen addition (represented by the grey bar) is followed by a period of inactivity for approximately 2~3 minutes after which activity begins to ensue. (b) Typical transient surface potential fluctuations approximately 5 minutes after stimulation depicts sharp rise and gradual recovery in surface potential over the time course of seconds. (c) Adding tyrodes solution to stimulated mast cells (green arrow) results in persistent activity. The cells are not displaced during addition of various stimulants. Notice (inset) typical rise and fall patterns in surface potential. (d) Monovalent hapten added subsequently (green arrow) to the recording shown in (c). A reduction in activity and collapses of the signal to basal noise level is immediately observed. This indicates that a dominant contribution to surface charging is IgE aggregation induced signalling. (e) PSD analysis of a 100 second portion of (c) and (d) clearly shows a reduction in the Nyquist-Johnson noise upon hapten addition. A slight reduction in 1/f noise and a more significant decrease in thermal noise indicate that the cell activity which introduces a resistive "cell adhesion" component of noise due to uptake and release of ions and mediators at the interface has reduced.

vesicular content re-equilibrates with the surrounding [46]. Figure 25(f) (white arrows) shows snapshots of vesicular release with green fluorescence transients as a function of time. Figure 25(g) shows the plot of fluorescent intensity as a function of time. Granular release (green), indicated by rapid fluctuations in fluorescence intensity [Fig.

25(g)], is shown to progressively increase with time with a plateau observed after ~4-6 minutes, which is in line with the degranulation kinetics measured by the transistor [black squares in Fig. 25(e)].

B. Transient responses at high temporal resolution

In the previous section, we described the use of quasi-static surface potential measurements to monitor exocytosis and found that ψ_O gradually shifts on the time scales of minutes after stimulation. While such recordings prove useful to ascertain antigen/receptor interactions, one cannot monitor events occurring on the order of milli-seconds. Quantal release events with such temporal scales are common during exocytosis [10], which can potentially be captured with transient recordings under constant CG bias. The release of neurotransmitters and hormones is accompanied by a low pH cloud and results in rapidly varying electrochemical potentials in the cell-transistor cleft [27]. The proximity of the cell to the sensing surface strengthens the capacitive coupling and increases the cleft resistance, inducing a strong modulation in the drain current during secretion. Due to the pH-sensitive nature of the SG interface, surface protonation contributes significantly to the amplitude of milli second current fluctuations as corroborated in previous studies [27]. This notion however does not rule out the hypothesis that other chemically active and inactive molecules can non-specifically bind to the sensing interface and shift ψ_O further. We are in the process of further characterizing this effect. During exocytosis, molecules are released within the cell-transistor cleft and diffuse towards the SG surface causing a shift in ψ_O . This is similar to a voltammetric signal; however the charge is not consumed in this

process. Transient recordings of RBL mast cell stimulation revealed a sharp rise and decay within minutes of stimulation (stimulation indicated by grey bar) with DNP BSA [Fig. 26(a)]. It is important to point out that mast cell exocytosis ensues only with sustained intracellular calcium oscillations [45-47]. These oscillations take a finite time to initiate and could possibly contribute to the initial delay observed between stimulation (grey bar) and the onset of vesicle release. However, once these oscillations set in, exocytosis should ensue with a distinct temporal behavior. In [Fig. 26(b)] we depict such a trace of activity from a different batch of cells approximately 6min after stimulation where rhythmic patterns of surface charging are observed. This rhythmic rise and fall in ψ_O rides on the DC operating point, i.e. it is a transient effect as opposed to the quasi-static threshold voltage measurements described in Fig. 25(e). We do point out that ψ_O is different between the start and end of the trace, possibly due to pH differences or molecular binding. The rapid re-equilibration in ψ_O [Fig. 26(b)] however, is explained as follows. Vesicle release is accompanied by protons, ions and a variety of transmitters as previously mentioned. Protons bind directly to the surface hydroxyl groups and shift ψ_O gradually [34], establishing a new surface charge (σ_O). A change in C_{dl} however due to released ionic charges and compounds causes a transient change in ψ_O (Eq. 2), which will further shift the surface proton concentration (H_S^+) through the Boltzmann relationship (Eq. 3). The surface, which acts like a proton buffer, will then try to maintain H_S^+ depending on the bulk pH condition and re-equilibrate to maintain ψ_O satisfying the condition

$\frac{\sigma_O}{C_{DL}} = \psi_O$ [48]. If the surface buffering capacity is weak, the re-equilibration will be slow leading to a delay in equilibrium establishment. Hence ionic charges and pH independently contribute to the observed signals.

$$\sigma_O = \psi_O C_{DL} \qquad (2)$$

$$H_S^+ = H_B^+ \exp(\frac{-e\psi_O}{kT}) \qquad (3)$$

Absence of $[Ca]_o$ in tyrodes suppressed these current fluctuations (not shown) while the introduction of monovalent hapten, which is known to disaggregate FcεRI clustering, effectively reduced the fluctuation to the baseline. This strongly indicates that the recordings are correlated with IgE cross linking induced signalling [7]. Figure 26(c) shows the effect of adding tyrodes to a section of an antigen stimulated response (shown by green arrow). The activity persists without any reduction in amplitude. We then add monovalent hapten indicated by the green arrow [Fig. 26(d)] and immediately find that the overall signal reduces in noise and amplitude. With uncorrelated noise sources, the total noise density in the system is the sum of individual noise densities. Power spectral density (PSD) analysis [Fig. 26(e)] performed on 100second chunks of recordings (green and red bars in [Fig. 26(c&d)]) clearly indicates a reduction in the energy density (also known as Nyquist noise) after hapten addition. Since the increase in noise is decided by the cell-transistor cleft activity, i.e. resistance and diffusion of ions [18], the noise reduction upon hapten addition directly relates to lower receptor aggregation and ion flow. The *1/f* noise reduces only slightly and appears to be dominated by the transistor channel noise due

to small reduction in the transconductance values.

C. Signal amplitudes and surface charging

Taking account of both the quasi-static and the transient responses, we attempt to resolve the physical basis of the detected signals. Using the simple relationship, $\Delta Q = C_{DL} * \Delta \psi_O$ the net total charge difference at the interface can be estimated. With an extracted capacitive ratio of ~12 and a specific double layer capacitance of $16 \frac{\mu F}{cm^2}$, $\Delta \psi_O$ of ~5mV corresponds to a net change in overall interface charge of $\Delta Q \sim 10\, pC$. We do point out that the calculation presented is a conservative estimate for surface charging and does not include direct molecular binding. Vesicle size in RBL-2H3 cells are approximately 0.4μm[49] in diameter. If each granule contained ~0.05pC (which is a reasonable estimate) and a total of 100 vesicles were released during exocytosis, the total charge secreted (~5pC) would correspond to mV signal amplitudes. It also suggests that the degranulation response is derived from a collection of vesicles rather than single vesicle events. On an average we have ~10-15 cells covering every SG.

D. Impedance spectroscopy at the RBL cell-transistor interface

As secretory granules fuse with the plasma membrane during exocytosis, the overall cell area increases in proportion to the extruded vesicular surface area. It is well known that the most biological membranes have a specific capacitance of $\sim 1 \frac{\mu F}{cm^2}$ and hence an increase in membrane area directly reflects an increase in overall capacitance [50]. RBL mast cell degranulation is often accompanied by rapid membrane ruffling

and morphological changes [51] within minutes of antigenic stimulation, resulting in a slight increase in total membrane capacitance reaching ~0.5pF[52, 53]. This is in stark contrast to traditional rat mast cells which reveal a near ~30pF change [54] due to the lower number of granules in the RBL line.

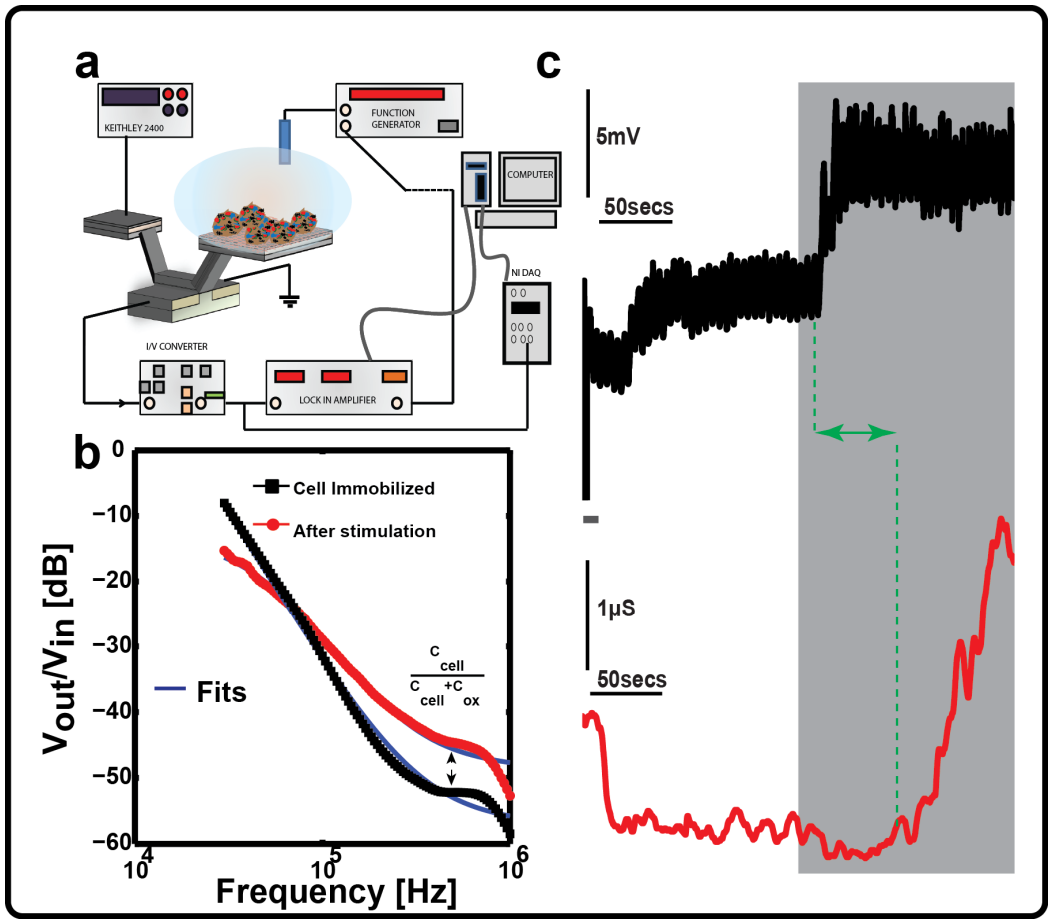

Figure 27: (a) Measurement setup showing the simultaneous impedance and charge detection by the split excitation technique on the CvMOS. The CG delivers the DC excitation while the reference electrode delivers the AC small signal (0.1V). The AC impedance magnitude signifies the transconductance as a function of frequency. (b) The pole-zero (Bode) responses before and after stimulation show the zero moving in, which is possibly due to the increase in cell membrane area during exocytosis. By a crude fit, we extract an overall increase in capacitance of ~0.1pF, which includes the capacitance increase from all the cells immobilized on the surface. The shift in the first pole position is due to an increase in interface resistance and the shift in zero is mainly due to capacitance changes at the cell transistor interface. (c) Simultaneous surface potential and transconductance measurements by measuring the DC and AC components (at 40KHz) independently. Notice that as soon as stimulation is initiated, there is a slight delay in response after which shifts in surface potential are observed (upper). A concomitant increase in g_m and hence capacitance is also observed (bottom) although there exists an initial decrease during stimulation. The change in

capacitance shifts the transistor g_m by ~1μS.
This effect along with granule fusion is normally captured by patch clamp capacitance recordings. Time-resolved impedance measurements thus allow for simultaneous measurements of membrane capacitance and conductance, thus providing a powerful tool to detect such secretion coupling events.

In order to further corroborate cell stimulation and exocytosis detection, we sought to confirm the overall capacitance shift through impedance analysis. Impedance detection along with surface potential was performed using a split excitation technique [Fig. 27(a)] where the AC signal is applied through the reference electrode and the DC bias through the CG. In order to concomitantly measure charge and net impedance, the TIA output was split two ways with one end fed to the NI DAQ board sampling voltage at 10 KHz while the other end was fed to the LIA. By monitoring the transconductance g_m as a function of frequency, one can measure the fluctuations in capacitance and interfacial resistance [55] as a shift in the pole-zero response [Fig 27(b)] upon mast cell immobilization. Previous efforts with the ISFET [56] used the AC impedimetric change to ascertain the seal resistance in the cell-transistor cleft, while in this chapter we employed the approach to capture fluctuations in cell/transistor interfacial impedance away from the quasi-static regime. The impedance readout at this operating point mainly depended on the net capacitance, and much less on charge fluctuations at the interface. The model for the cell-SG interface in frequency domain follows a similar theory to biomolecular modeling under frequency analysis [35] with the first pole dominated by interface resistance and the first zero dominated by the cell passive properties (see Appendix-E). In [Fig. 27(b)]

we show the effect of the antigen stimulation on the Bode response and observe a shift in the zero indicating an increase in the cell capacitance after stimulation. This result is consistent with the overall simulations and models presented earlier [35, 55, 56]. We fit the data in spite of the limited frequency range to gain an estimate for circuit parameters. We extract a capacitance change between ~0.05pF-0.1pF, depending on selection of fitting parameters. This is lower in comparison to the whole-cell patch clamp recordings of mast cell exocytosis [53] where shifts on the order of 0.4pF have been observed. We rationalize that in impedance mode we have access only to the attached membrane in the cell-transistor overlap region which varies less in surface area while the free membrane (portion away from the transistor surface) varies a lot more in surface area during exocytosis. Moreover the impedance change is also affected by total cell coverage. We do point out that in a recent impedance study [55], although performed on a different cell line, the extracted values of seal resistance and cell capacitance agree well with the values reported here.

In [Fig. 27(c)] we perform a concomitant ψ_O and impedance measurement at a fixed frequency (40 KHz). We find a step increase in ψ_O upon antigenic stimulation with a distinct time course indicative of surface charging. The recording is not high pass filtered in this study so as to reflect this DC shift. The AC impedance reflected by the transconductance measurement initially decreases upon stimulation but then subsequently increases (shaded region), suggesting cell secretion and capacitance change due to morphology. We do observe about 50-second delay between the surface charging and impedance change, possibly reflecting differences in dynamics between

cell secretion and gradual membrane expansion. Although performed on a population of immobilized cells, this experiment points out a clear indication that transistors can be used to simultaneously measure capacitance (impedance) and charge (surface potential). Future experiments will be aimed at experiments involving single cell studies.

E. The Chromaffin cell-transistor coupling

To further demonstrate exocytosis detection by CvMOS with high-resolution transients, we chose the chromaffin cell of the bovine adrenal medulla as a known exocytotic model [57, 58] albeit through a different mode of stimulation. The chromaffin cell helps serve as a model system of voltage-gated ion-channel activity and exocytosis induced by membrane depolarization. Chromaffin cells are known to secrete catecholamines as a consequence of exocytosis and the granular content is known to be highly acidic which should contribute to a net shift in surface potential upon release. One important difference between the chromaffin and mast cell studies is that the electrical currents in the form of AP can flow in the cell transistor junction as a result of activated ion channel activity in neuro-endocrine cells [59, 60]. In previous transistor-based studies of chromaffin cells, this aspect of signalling (i.e. AP's) was ignored [27].

Chromaffin cells suspended in ringer's solution were then dispensed on the poly-l-lysine coated SG. After about 45~60 minutes concentrated KCl solution was added with a pipette to reach a final KCl concentration of ~80mM. Upon KCl stimulation which causes membrane depolarization, we observed sharp fluctuations in readout

current [Fig. 28(a)]. The recorded signals were found to be strongly dependent on extracellular $[Na]_o$ and $[Ca]_o$, suggesting contributions from AP and catecholamine release.

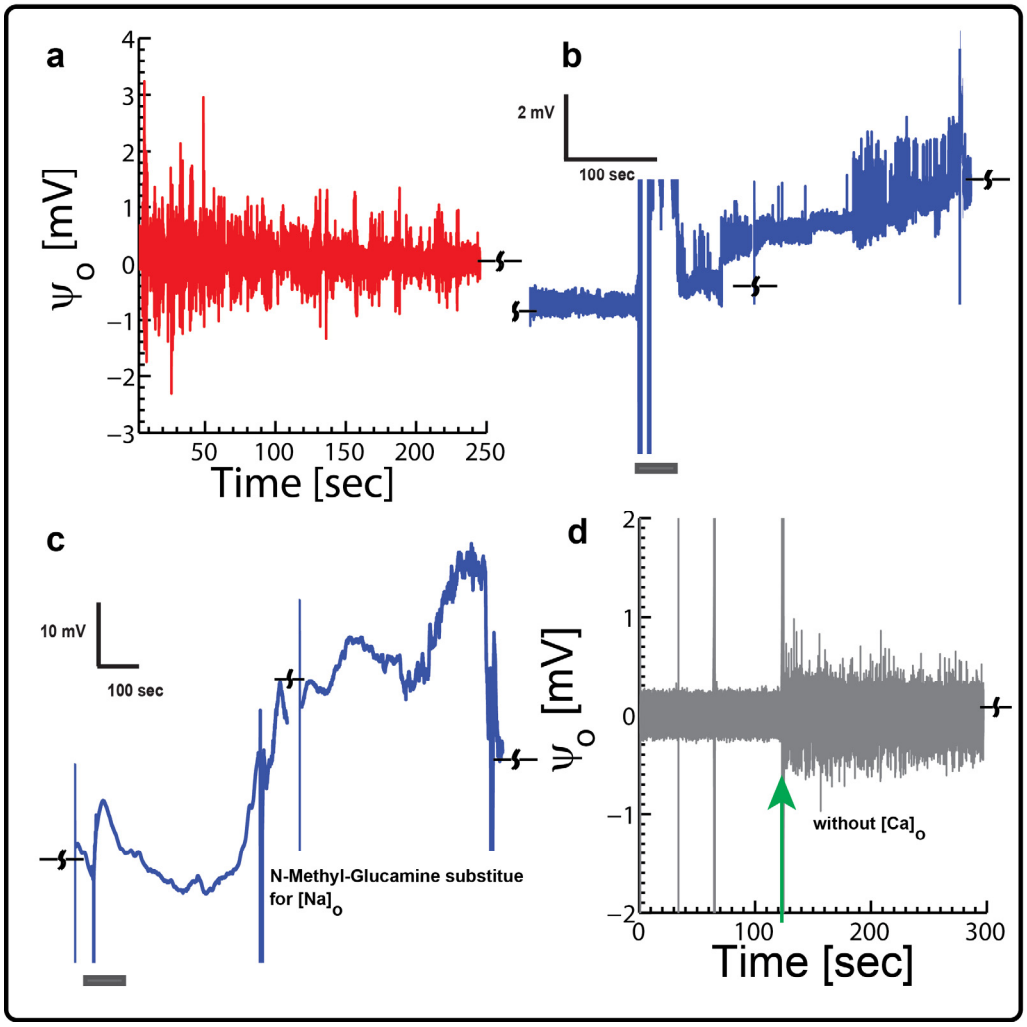

Figure 28: Transient responses of chromaffin cells: (a) Sample of activity after high KCl induced depolarization (high pass filtered) shows rapid fluctuations in surface potential, which suggests AP with peak-peak amplitudes reaching ~2mV. (b) Effect of adding Ringer's solution rich in $[Na]_o$ to the transistors with cells previously bathed in NMG substituted Ringer's and stimulated with high KCl. Notice the steady shift in surface potential (not high pass filtered) indicates positive secreted charge along with rapid spikes resembling AP, suggesting that the transistor response is closely tied with $[Na]_o$. (c) A 300-second recording of stimulated activity (not high pass filtered) in the presence of NMG substituted Ringer's shows clear increase of surface potential shifts with time, but AP's are reduced. (d) Stimulated response of chromaffin cells in the absence of $[Ca]_o$. The presence of AP persists.

We independently confirm the presence of AP and exocytosis through the following control experiments. Figure 28(b) depicts the effect of $[Na]_o$ replenishment by adding ringers solution rich in $[Na]_o$ (marked by grey bar) to cells previously stimulated by high KCl in NMG substituted ringers media. The high-pass filter criterion was relaxed to observe slow ψ_O shifts. We immediately observe surface charging and rapid fluctuations upon $[Na]_o$ being introduced indicating that fluctuations are a true consequence of AP activity. In a separate study [Fig. 28(c)] we once again add high KCl (grey bar) to immobilized chromaffin cells in NMG rich ringer's media. We notice a gradual increase in ψ_O as a function of time upon KCl depolarization although AP's are not evident. The rise in ψ_O denotes a net positive surface charging effect similar to the mast cell degranulation study, indicating that exocytosis is possibly being detected. We do observe fluctuations in ψ_O with large time courses (~100msec) typical of delayed surface re-equilibration (not shown). In the absence of $[Ca]_o$, slow ψ_O shifts were absent altogether (not shown) while AP waveforms characterized by their milli-second time scales and rapid activity continued to persist [Fig. 28(d)] upon stimulation by high KCl (green arrow). This experiment clearly indicates that the gradual ψ_O shifts measured previously are possibly a consequence of exocytosis and subsequent SG surface charging. The observed amplitude of extracellular AP's were smaller in the absence of $[Ca]_o$ over ~3 experimental runs, although we present only one representative result here. This observation could be attributed to the following reasons: a) there exists a feedback between granular

secretion and ion channel activity, b) calcium activated potassium currents (IKCa) are significant, and c) there exists a relatively low ion channel conductance in the cell-transistor cleft as opposed to the free membrane in the absence of $[Ca]_o$. Past works have established that IKCa in chromaffin cells comprises of almost 70-90% of the outward potassium current [61]. Also AP stimulus and firing rates are known to play a key role in stimulus secretion coupling [62]. The present study however does not provide sufficient evidence and requires further experimental investigation.

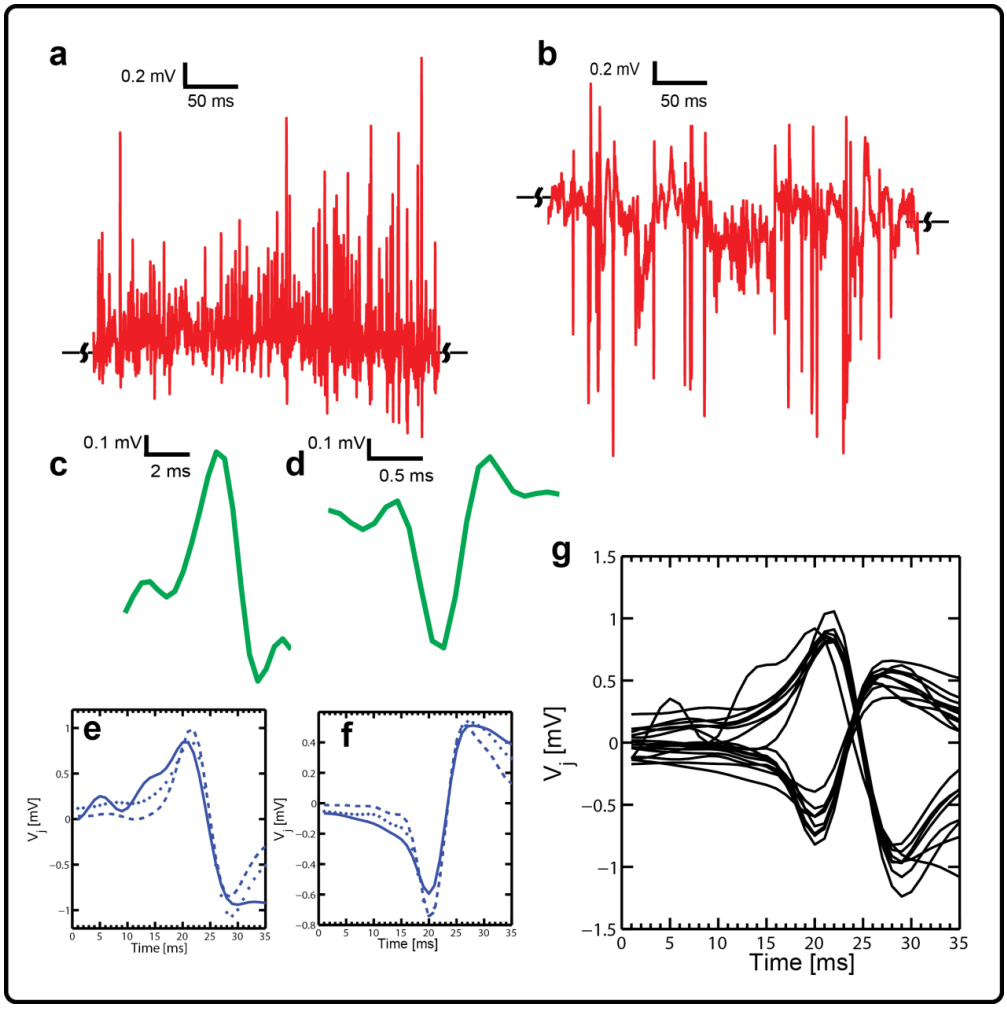

Figure 29: Transient activity for chromaffin cell stimulation depicting biphasic waveforms observed during the rising phase of an intracellular AP. (b) A trace of inverted capacitive waveforms. (c)&(d) Templates of the biphasic and inverted AP waveforms used for matched filtering. (e) Average match

filter response for 3 independent experiments shows the shape and amplitude of the biphasic response recovered. (f) Inverted capacitive response for the same. (g) Clusters of biphasic and inverted waveforms after performing an amplitude threshold and match filter operation. The shape and amplitudes are very homogenous and are ~ 0.8-2mV peak to peak.

The effect of ion channel distribution between the free and transistor-attached parts of the cell membrane is a key parameter that determines the amplitude and shape of the AP. As shown in [Fig. 29(a&b)], we observe both biphasic and inverted capacitive responses [Fig. 29(c&d)]. Such waveforms are classically interpreted [63] as (a) a capacitive (i.e. biphasic) response across the cell membrane due to the intracellular AP which gives rise to a shift in junction voltage (V_J) and (b) the ion-channel conductance in the cell-transistor cleft (inverted capacitive) of either the Na, K or both are raised against the free membrane. We perform match filtering and amplitude threshold signal processing on three independent experiments lasting between 200-300 seconds each where chromaffin cells are stimulated by high KCl. Over the time course of the entire experiment, recurring AP waveforms with a clear biphasic and inverted capacitive response are observed [Fig. 29(e&f)]. The inverted response has on average slightly lower amplitudes in comparison to the biphasic response. Figure 29(g) depicts a cluster of the biphasic and inverted waveforms for ~100 seconds of recorded data after match filtering and threshold operations. In order to elucidate the physical basis of the waveforms we used the point-contact model including the Hodgkin-Huxley (HH) description for ion channel activity in the cell-transistor cleft developed previously[63] (see Appendix-E, Fig. 46(b)). Following the approach used in[63] , the intracellular membrane potential V_M elicited through a current stimulus was calculated using Eq. (5) [Fig. 30(a)] along with the rate equations outlined in[64] for Na^+, K^+ ,

Ca^{2+} and Ca^{2+} dependent K^+ conductances at room temperature. V_M was then used to calculate the cleft potential V_J in Eq. (6).

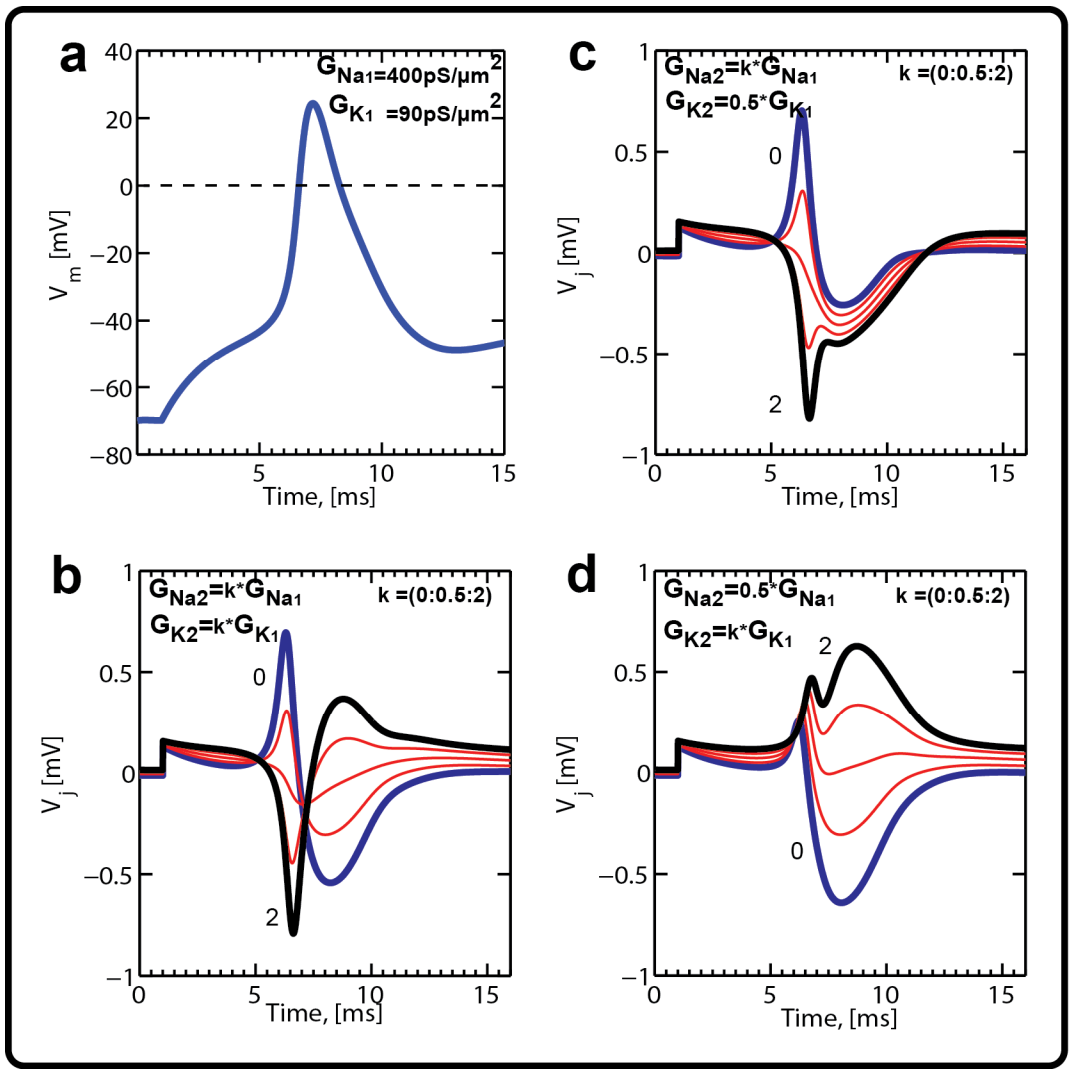

Figure 30: Simulation of electrical response using the point contact model. (a) A typical intracellular membrane voltage when an AP is elicited. (b) Effect of raising the overall junction conductance with respect to the free membrane conductance. Notice, that when conductance values for both Na^+ and K^+ are simultaneously raised in the junction, the extracellular waveforms shift from biphasic to inverted capacitive. (c) Similar operation to (b) with the K^+ conductance in the junction decreased with respect to the free membrane. When the Na^+ and K^+ conductance in the junction is now raised, the Na^+ activity becomes much larger than the K^+ activity. This causes a trough in the AP waveform. (d) Similar operation to (c) but with the Na^+ conductance decreased in the junction. This causes an intracellular-like waveform although with a diminished amplitude.

$$\frac{I_{INJ}}{A_{FM}} = \sum_i (g_{FM} + \beta g_{JM}) \cdot (V_M - V_o) + C_M \cdot \frac{dV_M}{dt} \qquad (5)$$

$$V_J \cdot g_J = \sum_i (V_M - V_o) \cdot g_{JM} + C_M \cdot \frac{dV_M}{dt} \qquad (6)$$

$$V_J \cdot g_J = \sum_i (V_M - V_o) \cdot (g_{JM} - g_{FM}) + \frac{I_{INJ}}{A_{FM}} \qquad (7)$$

The main assumption made here is that dynamics of the intracellular and extracellular voltages are coupled. The free membrane creates a potential $V_M(t)$ (Eq. 5) and the cleft reacts with a signal $V_J(t)$. By substituting Eq. (5) in Eq. (6) we achieve Eq. (7) which depicts the interplay between the free and attached membrane conductances. Here g_{JM} represents the conductance in the cell membrane in contact with the transistor SG, β represents the ratio of immobilized membrane surface area to the free membrane area, g_{FM} represents the conductance in the free membrane not in contact with the transistor and g_J represents the conductance in the cell-transistor cleft due to displaced ions (i.e., the effective seal resistance). Also C_M is the specific membrane capacitance. Here, *i* represents the different types of channels (i.e. Na^+, K^+ and leakage channels). The cell thus acts like a current source creating an extracellular potential due to the net resistance in the cleft [55].

In the model we chose to maintain the specific free membrane conductance for Na^+ (G_{Na1}) , K^+ (G_{K1}) as and Ca2+ dependent K+ conductance as 400pS/μm^2 , 90pS/μm^2

and 70pS/μm^2 respectively. The resting potential values for Na, K and leak currents were 50mV, -70mV and -75mV respectively. A cell diameter of ~15um was assumed. All Ca^{2+} dependent activity was simulated based on the theory outlined in previous studies [64, 65]. The overall attached membrane conductance (G_{Na2} and G_{K2}) was scaled by factors ranging from 0 to 2 in steps of 0.5 (i.e. $G_{Na2} = G_{Na1} \cdot k$ and $G_{K2} = G_{K1} \cdot k$) with respect to the attached membrane values [Fig. 30(b-d)]. It is important to note that the values of conductances used here are pertinent to rat chromaffin cells and likely to be different for bovine chromaffin cells[64]. Although it would be of high interest to elucidate the functional role of each channel type in the overall secretory response, the information at present is not enough to model all conductances and merely serves as a guide to what is to be expected. For example the authors in[64] used an integrated version of all Ca^{2+} channel subtypes to describe chromaffin cell AP activity by modifying the properties of L-type channels in thalamocortical relay neurons[65]. The validity of the model was corroborated against experimental data. We make the assumption that Bovine and rat adrenal chromaffin cells have similar signalling mechanisms and ion channel activity at play and hence can be described by similar rate equations and constants. We find that with this assumption, the recorded amplitudes and waveform shapes are remarkably similar to theoretical predictions. One difference, however, is that the half width time scales of the average AP's recorded was higher ~5msec compared to the simulated waveforms (~2msec). While the reason for this is still experimentally not corroborated we attribute this slight discrepancy to the slow ionic relaxation in the cleft due to the large SG capacitance.

When the overall ionic conductance in the cleft was raised with respect to the attached membrane with G_{Na2} = k*400pS/μm^2 and G_{K2} = k*90pS/μm^2, the waveforms resemble inverted transients (for *k* = 2) [Fig. 30(b)]. We also find that if G_{K2} is lowered in the cleft to 45pS/μm^2, GNa_2 and hence the overall Na^+ conductance appears higher when scaled than K^+ in the cleft, which causes the inverted response to become broader [Fig. 30(c)]. This happens because Na^+ rushes into the cell during the rising phase of the AP, and ionic charges get depleted in the cleft resulting in a steeper trough in the AP waveform. Decreasing the Na^+ conductance by half in the cleft and subsequent scaling of the K^+ conductance in comparison creates a stronger rise in the extracellular AP and a diminished intra-cellular waveform [Fig. 30(d)] with a slightly broader time course, which is indicative of K^+ channel dominance. Such waveforms however were found to be statistically insignificant (data not shown). With respect to extracellular AP amplitudes, a cleft conductance of approximately ~5000pS/μm^2 which is reflective of a moderate seal resistance, results in extracellular peak-peak amplitudes of approximately ~800μV-1mV [Fig. 30(b)], in accordance with previous transistor studies on neurons [16, 17]. Higher cleft resistances, i.e. a lower cleft conductance, will amplify the extracellular potential even further and hence improve the coupling between the cell and transistor, which is paramount to ensure high signal-to-noise ratio. A considerable amount of experimental effort has been previously performed on neurons to elucidate the underlying physical basis of such signals [15, 16, 66] based on ion channel re-distribution, enhancement and depletion. From figures [29&30] we infer that since both biphasic and inverted capacitive responses were recorded by the CvMOS, ion channel re-distribution across the chromaffin cell membrane is an

important source of signal and up-regulated Na^+ , Ca^{2+} dependent K^+ and K^+ conductances in the cleft with respect to the free-membrane as the likeliest scenario for waveform difference. The experimental evidence presented in this study further validates extends the applicability of the point-contact model to primary neuro-endocrine cells.

CONCLUDING REMARKS

Degranulation in mast cells and action potential activity in chromaffin cells were monitored through quasi-static surface potential measurements, high resolution transient recordings and impedance spectroscopy using CvMOS transistors. The kinetics of vesicle release recorded by such charge sensitive detectors was found to agree well with fluorescence data. High temporal resolution recordings traditionally not achievable by fluorescence microscopy are also presented. In addition to electrochemical signatures of charged vesicle release, the transistor also detected fast ionic activities in the form of action potentials with sensitivity similar to traditional ISFET's. The neuromorphic approach renders independent pixel-level sensitivity control via the CG which also enables a new split-gate AC impedimetric measurements, where the DC bias and a global small signal AC perturbation can be delivered through the CG and the reference electrode, respectively. This effect is particularly relevant in large sensor arrays where different pixels may require individual control over sensitivity. Further the extended gates and channel area can be independently designed to improve capacitive coupling and frequency tuning. Future

work aims at demonstrating such neuromorphic array, which can be coupled to cell populations with sub-cellular resolution and sensitivity.

Supplemental Material: Supplementary material accompanies this chapter, refer Appendix-E.

REFERENCES

[1] D. Zenisek, J. A. Steyer, and W. Almers, Nature **406**, 849 (2000).

[2] S. Y. Yang *et al.*, Advanced Materials **23**, H184 (2011).

[3] A. Yakushenko, E. Kätelhön, and B. Wolfrum, Analytical Chemistry **85**, 5483 (2013).

[4] J. A. Steyer, H. Horstmann, and W. Almers, Nature **388**, 474 (1997).

[5] A. Albillos *et al.*, Nature **389**, 509 (1997).

[6] E. Pothos, M. Desmond, and D. Sulzer, Journal of Neurochemistry **66**, 629 (1996).

[7] D. Holowka, and B. Baird, Annual Review of Biophysics and Biomolecular Structure **25**, 79 (1996).

[8] M. Lindau, and E. Neher, Pflugers Arch - Eur J Physiol **411**, 137 (1988).

[9] R. M. Wightman *et al.*, Proceedings of the National Academy of Sciences **88**, 10754 (1991).

[10] I. Hafez *et al.*, Proceedings of the National Academy of Sciences of the United States of America **102**, 13879 (2005).

[11] S. Ayers *et al.*, Circuits and Systems I: Regular Papers, IEEE Transactions on **54**, 736 (2007).

[12] S. Ayers *et al.*, Biomedical Circuits and Systems, IEEE Transactions on **4**, 86 (2010).

[13] B. N. Kim *et al.*, Biosensors and Bioelectronics **41**, 736 (2013).

[14] A. Cohen *et al.*, Biosensors and Bioelectronics **19**, 1703 (2004).

[15] A. Cohen *et al.*, Biosensors and Bioelectronics **23**, 811 (2008).

[16] R. Schätzthauer, and P. Fromherz, European Journal of Neuroscience **10**, 1956 (1998).

[17] F. Patolsky *et al.*, Science **313**, 1100 (2006).

[18] M. Voelker, and P. Fromherz, Physical Review Letters **96**, 228102 (2006).

[19] S. Ingebrandt *et al.*, Biosensors and Bioelectronics **16**, 565 (2001).

[20] B. Tian *et al.*, Science **329**, 830 (2010).

[21] P. Fromherz, ChemPhysChem **3**, 276 (2002).

[22] E. Stern *et al.*, Nano Letters **8**, 3310 (2008).

[23] M. Brittinger, and P. Fromherz, Appl Phys A **81**, 439 (2005).

[24] R. A. Kaul, N. I. Syed, and P. Fromherz, Physical Review Letters **92**, 038102 (2004).

[25] S. Meyburg *et al.*, Sensors and Actuators B: Chemical **128**, 208 (2007).

[26] P. Bergveld, Biomedical Engineering, IEEE Transactions on **BME-17**, 70 (1970).

[27] J. Lichtenberger, and P. Fromherz, Biophysical journal **92**, 2262 (2007).

[28] B. Eversmann *et al.*, Solid-State Circuits, IEEE Journal of **38**, 2306 (2003).

[29] A. Lambacher *et al.*, Appl Phys A **79**, 1607 (2004).

[30] G. Zheng *et al.*, Nat Biotech **23**, 1294 (2005).

[31] J.-H. Ahn *et al.*, Nano Letters **10**, 2934 (2010).

[32] B. C. Jacquot *et al.*, Biosensors and Bioelectronics **23**, 1503 (2008).

[33] N. Y. M. Shen *et al.*, Electron Devices, IEEE Transactions on **50**, 2171 (2003).

[34] K. Jayant *et al.*, Phys.Rev.E **88**, 012801 (2013).

[35] K. Jayant *et al.*, Phys.Rev.E **88**, 012802 (2013).

[36] T. Shibata, and T. Ohmi, IEEE Trans. Electron Devices **39**, 1444 (1992).

[37] C. Mead, Proceedings of the IEEE **78**, 1629 (1990).

[38] C. Diorio *et al.*, in *Neuromorphic Systems Engineering*, edited by T. Lande (Springer US, 1998), pp. 315.

[39] P. Hasler, B. A. Minch, and C. Diorio, Circuits and Systems II: Analog and Digital Signal Processing, IEEE Transactions on **48**, 74 (2001).

[40] B. Minch *et al.*, Analog Integr Circ Sig Process **9**, 167 (1996).

[41] M. Lindau, Fernandez, J. M., Nature **319**, 150 (1986).

[42] T. D. Parsons *et al.*, Neuron **15**, 1085 (1995).

[43] K. A. Field, D. Holowka, and B. Baird, Journal of Biological Chemistry **274**, 1753 (1999).

[44] K. Jayant, K. Auluck, and E. C. Kan, in *Sensors, 2013 IEEE*2013), pp. 1.

[45] C. Fewtrell, Annual Review of Physiology **55**, 427 (1993).

[46] R. Cohen *et al.*, Journal of Cell Science (2012).

[47] T. D. Kim *et al.*, Journal of Biological Chemistry **272**, 31225 (1997).

[48] J. C. van Kerkhof, J. C. T. Eijkel, and P. Bergveld, Sensors and Actuators B: Chemical **18**, 56 (1994).

[49] R. M. Williams, and W. W. Webb, Journal of Cell Science **113**, 3839 (2000).

[50] N. E. G. B. D. Fernandez JM, Nature **312**, 29 (1984).

[51] D. E. Chandler, and J. E. Heuser, The Journal of Cell Biology **86**, 666 (1980).

[52] A. R. Artalejo, J. C. Ellory, and A. B. Parekh, Pflugers Arch - Eur J Physiol **436**, 934 (1998).

[53] R. E. Thompson, M. Lindau, and W. W. Webb, Biophysical journal **81**, 937 (2001).

[54] M. Lindau, and B. D. Gomperts, Biochimica et Biophysica Acta (BBA) - Reviews on Biomembranes **1071**, 429 (1991).

[55] S. Schäfer *et al.*, Biosensors and Bioelectronics **24**, 1201 (2009).

[56] V. Kiessling, B. Müller, and P. Fromherz, Langmuir **16**, 3517 (2000).

[57] E. Neher, and A. Marty, Proceedings of the National Academy of Sciences **79**, 6712 (1982).

[58] D. E. Knight, and P. F. Baker, J. Membrain Biol. **68**, 107 (1982).

[59] Z. Zhou, S. Misler, and R. H. Chow, Biophysical journal **70**, 1543 (1996).

[60] E. M. Fenwick, A. Marty, and E. Neher, The Journal of Physiology **331**, 599 (1982).

[61] J. J. Pancrazio, P. A. Johnson, and C. Lynch Iii, Brain Research **668**, 246 (1994).

[62] Z. Zhou, and S. Misler, Journal of Biological Chemistry **270**, 3498 (1995).

[63] P. Fromherz, Eur Biophys J **28**, 254 (1999).

[64] A. Warashina, and T. Ogura, Pflugers Arch - Eur J Physiol **448**, 161 (2004).

[65] D. A. McCormick, and J. R. Huguenard, Journal of Neurophysiology **68**, 1384 (1992).

[66] M. Jenkner, and P. Fromherz, Physical Review Letters **79**, 4705 (1997).

CHAPTER-7: CONCLUSION AND FUTURE WORK

This dissertation focuses on transistor based bio-sensing technology realized in foundry CMOS. The transistor design is inspired from flash memory and its operation is based on neuromorphic principles. Fundamental issues relating to solid-liquid interface phenomena with and without biomolecules have been addressed both experimentally and theoretically. Dual gate ISFET operation is presented and is shown to have tremendous advantage over conventional ISFET's by including features such as simultaneous sensing and actuation, offset control, intrinsic threshold voltage magnification, co-localized impedance and charge detection.

Critical aspects with regard to the nature of the surface equilibrium constants is investigated theoretically and verified experimentally. Observations suggest that a non-Nernstian interface (such as poly-silicon) can be tuned from being pH sensitive to pH insensitive and vice versa by the application of underlying electric fields. Field effect pH sensitivity tuning is found to be maximal around the pH insensitive region (i.e. region between the 2pK's). In addition to applying a separate control gate bias electric field modulation in the sensing gate oxide is also realized through non-volatile charge storage (hole/electron storage) giving rise to the concept of programmable ISFET interface. Such a surface charge tuning mechanism can potentially be used to tune surface potential, push the interface into a pH insensitive region and hence serve as a nanoscale reference bias in solution for pH sensing applications. Ion-ion interactions and evidence of charge inversion is presented (pertinent when dealing

with multivalent ions). Effect of ion size is considered when dealing with the interface and is found to be critical only under extremely surface potentials. Tunneling operation is outlined both theoretically and experimentally. Capacitive asymmetry is shown to influence the tunneling mechanism by inducing a positive feedback effect during control gate bias application.

In addition to surface pH tuning, non-volatile charge injection is used to desorb electrostatically adsorbed biomolecules. This functionality gives rise to the concept of electrical refreshabilty wherein, a bio-sensing surface can be regenerated for re-use after a sensing operation is performed. In addition field dependent sensitivity enhancement is also presented. Factors that affect sensitivity are theoretically treated and experimentally verified. The use of trace amounts of multivalent ions in the electrolyte bath is found to enhance hybridization sensitivity by locally modifying the screening charge at the transistor interface during DNA adsorption.

One limitation of charge based detection of DNA interactions using FET's is the issue of Debye screening and DNA-DNA repulsion at low salt concentrations. In order to avoid such issues, the use of self-amplifying DNA nanostructures is introduced and when coupled with impedance mode detection is shown to improve LOD to ~1pM. The addition of functionalized AuNP's along with branched DNA nanostructures is found to additionally improve the LOD to ~100fM.

Chromaffin and RBL-2H3 mast cells are coupled to transistors to detect exocytosis. With chromaffin cells, in addition to vesicle release (evidenced by surface potential shifts), AP activity is also recorded. AP activity is found to be highly dependent on ion channel distribution across the attached and free membrane. Signal generation due to

vesicle release from RBL-2H3 Basophils is found to be highly dependent on buffer strength indicating sensitivity to net proton content released during degranulation.

FUTURE WORK

Immediate future work includes the following:

1. Incorporate different dielectric coatings (Al2O3, HfO2, Si3N4 etc) on the sensing gate surface and study the gating properties to extract pH tuning range.
2. Extract surface equilibrium constants, PZC etc.
3. Incorporate ionic flow (Poisson Nernst-Planck) into the present quasi-static model to reveal non-equilibrium effects.
4. Perform biomolecular sensing with co-localized flow control to improve screening limited response.
5. Study the physical effects that cause relaxations of biomolecules in an AC field and whether can be adopted for non-spherical objects
6. Perform simultaneous pH and impedance sensing.
7. Investigate differential sensing capabilities to reject common mode non-idealities during quasi-static and impedance sensing
8. Scale the floating gate to nanoscale dimensions to probe nanoscale interface phenomena (Ex: nanowires, nanotube etc)
9. Integrate CνMOS with supporting signal conditioning circuitry to realize large scale arrays.
10. Integrate active feedback to monitor charge and impedance simultaneously.

11. Realize arrays of CνMOS based amplifiers and co-localized photo-diodes for simultaneous optical and electrical recording with multiplexing capabilities.
12. Culture populations of chromaffin and mast cells on arrays to probe spatio-temporal dynamics of signalling responses.

APPENDIX-A

Supplemental information for chapter-2 includes additional details of the physical principles that describe the device operation, control experiments that support details presented in the main text, simulation of the tunneling operation. Table outlining the equation set describing the working of the $C\upsilon MOS$ transistor is also included.

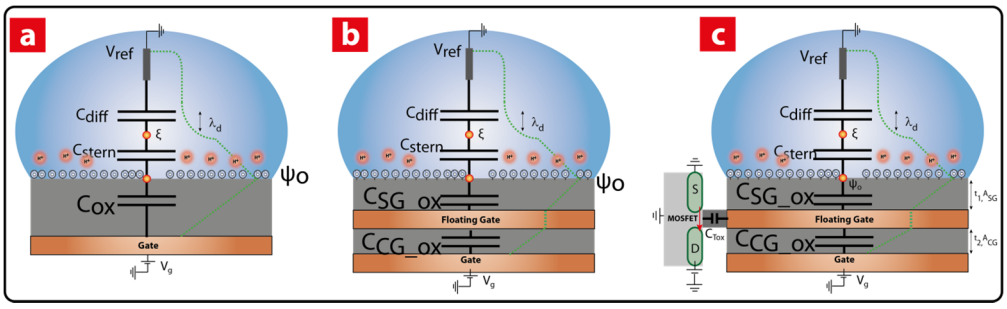

Figure 31: Electrochemical gating concept. a) The capacitive model of the EOS structure under study. A potential difference between the control gate and the reference electrode disturbs the chemical equilibrium at the oxide electrolyte interface. (b) Introduction of a floating conductor between the CG and oxide electrolyte interface. C_{CG_OX} and C_{SG_OX} are the capacitances between the CG and FG, and between FG and solution interface, respectively. The electrolyte is gated via the field in the underlying oxide set by the FG potential. (c) Capacitive coupling of a transistor to the FG. The CG bias and the difference between $\psi_O - V_{REF}$ capacitively set the FG potential via the capacitive divider which modulates the transistor output. The CG is thus a handle to control both the transistor output and $\psi_O - V_{REF}$.

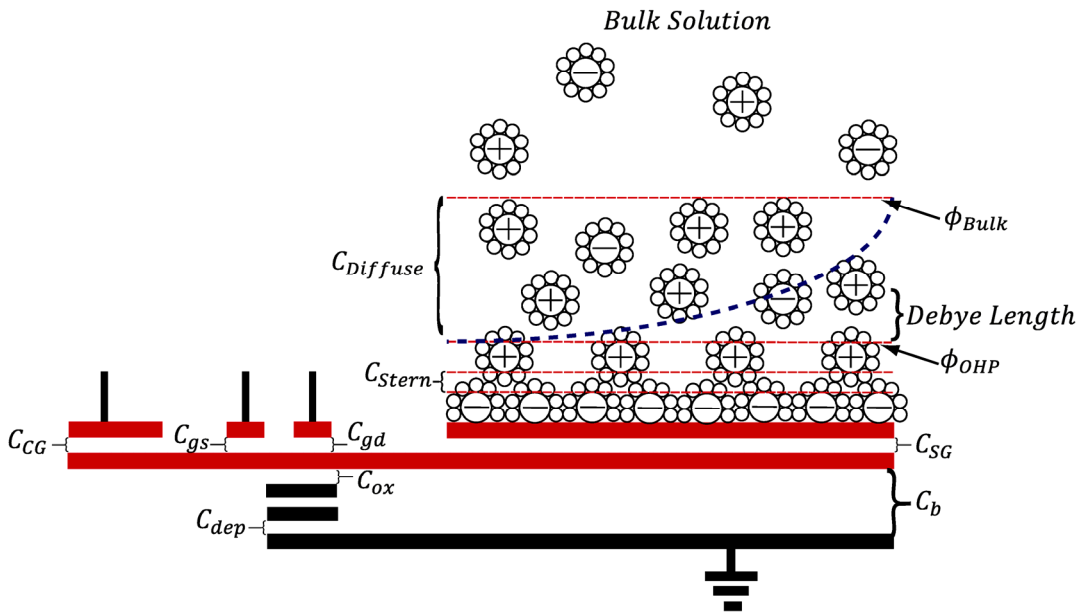

Figure 32: The capacitive model with various capacitance inputs. C_{CG} and C_{SG} are the control and sensing gate capacitance, respectively. The double layer capacitances are depicted as the Stern and diffusive component, respectively. Beyond the Debye length, the charge on the adsorbed molecule is effectively screened. Here ϕ_{OHP} represents the outer helmholtz potential commonly termed ξ potential i.e. the potential at the slip plane.

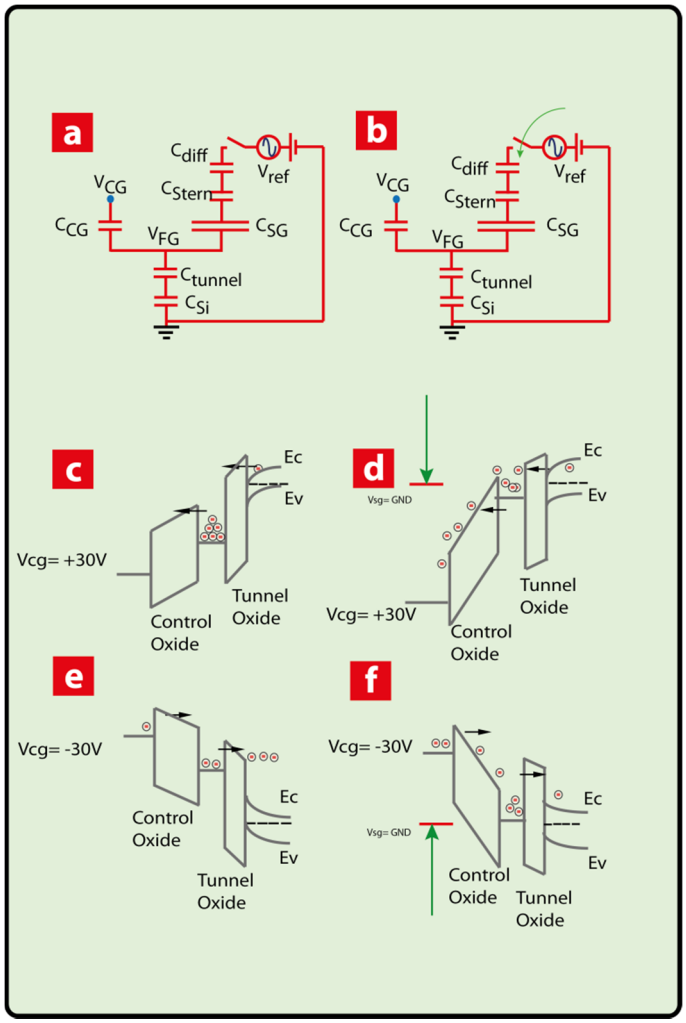

Figure 33: (a) Capacitive network of the CvMOS with V_{REF} open circuited and (b) V_{REF} grounded. (c) Band diagram with V_{REF} open circuited and a +30V application on the CG depicts electron injection into the FG. Notice how the FG potential tracks the CG bias (d) Band diagram with V_{REF} at ground and a +30V CG bias results in large electron out tunneling which results in hole storage on the FG. The FG potential is strongly pinned by the reference electrode bias (e) same condition as (c) with a -30V CG bias. This creates hole storage on the FG. (f) Same condition as (d) with a -30V CG bias, this results in electron injection from the CG into the FG.

Accounting for finite size of ions using a Modified Poisson Boltzmann (MPB) model:

The electrochemical potential can be described as follows[1]:

$$\mu_{\pm} = \pm ze\psi - k_B T \ln n_{\pm} - k_B T \ln(1 - n_+ a^3 - n_- a^3) \quad (1)$$

where $\mu_{\pm}$ is the electrochemical potential of the associated ions, a the radius of the ion, z the ion valency, e the elementary charge, ψ the electrostatic potential, $k_B T / e$ the thermal voltage, and $n_+ \; and \; n_-$ are the concentrations of the positive and negative ions.

Under equilibrium the spatial derivative of the electrochemical potential is zero. Explicit solution

of $\nabla \mu_{\pm} = 0$ relates the applied potential to the ionic densities given by

$$n_{\pm} = \frac{n_\infty e^{\mp \frac{ze\psi}{k_B T}}}{1 + 2\nu \sinh^2\left(\frac{ze\psi}{2k_B T}\right)} \quad (2)$$

For z:z electrolytes and

$$n_- = \frac{n_\infty e^{\frac{ze\psi}{k_B T}}}{1 - \nu + \nu\left(\frac{e^{\frac{ez\psi}{k_B T}} + ze^{\frac{-e\psi}{k_B T}}}{1+z}\right)} \quad (3)$$

and

$$n_+ = \frac{n_\infty e^{\frac{-e\psi}{k_B T}}}{1-\nu+\nu\left(\frac{e^{\frac{ez\psi}{k_B T}}+ze^{\frac{-e\psi}{k_B T}}}{1+z}\right)} \qquad (4)$$

For a 1:z electrolyte respectively

where ν is the bulk volume fraction and n_∞ is the bulk ionic concentration. The counter ion density saturates at $2\frac{n_\infty}{\nu}=\frac{1}{a^3}$ when $\psi >> 2\frac{k_B T}{ze}$. One should note that the radius and valence of the cation and anion are assumed to be the same for convenience. Solving Poisson's equation with constraints set by (1) and (2) becomes

$$\varepsilon\nabla^2\psi = 2zen_\infty \frac{\sinh\left(\frac{ze\psi}{k_B t}\right)}{1+2\nu\sinh^2\left(\frac{ze\psi}{2k_B T}\right)} \qquad (5)$$

Integrating (5) we get the normal electric field ,

$$\frac{\partial\psi}{\partial x} = -\mathrm{sgn}(\psi)\frac{2zen_\infty\lambda_D}{\varepsilon}\sqrt{\frac{2}{\nu}\ln\left(1+2\nu\sinh^2\left(\frac{ze\psi}{2kT}\right)\right)} \qquad (6)$$

Substituting (6) in the relationship $\frac{\partial\psi}{\partial x}(x=0)=\frac{q_c}{\varepsilon}$, we arrive at the charge-potential relationship given by

$$q_{MPB} = -\mathrm{sgn}(\psi_{DL})2zen_\infty\lambda_D\sqrt{\frac{2}{\nu}\ln\left(1+2\nu\sinh^2\left(\frac{ze\psi_{DL}}{2kT}\right)\right)}$$

(7)

where q_{MPB} is the total charge in the diffusive layer, λ_D is the Debye screening length and ψ_D is the diffusive layer potential with respect to the bulk. From the charge-potential relationship we then deduce the differential component of the diffusive double layer:

$$C_D^{\nu} = \frac{\frac{\varepsilon}{\lambda_D}\sinh\left(\frac{ze\psi_D}{k_B T}\right)}{\left(1+2\nu\sinh^2\left(\frac{ze\psi_D}{2k_B T}\right)\right)\times\sqrt{\frac{2}{\nu}\ln\left(1+2\nu\sinh^2\left(\frac{ze\psi_D}{2kT}\right)\right)}} \tag{8}$$

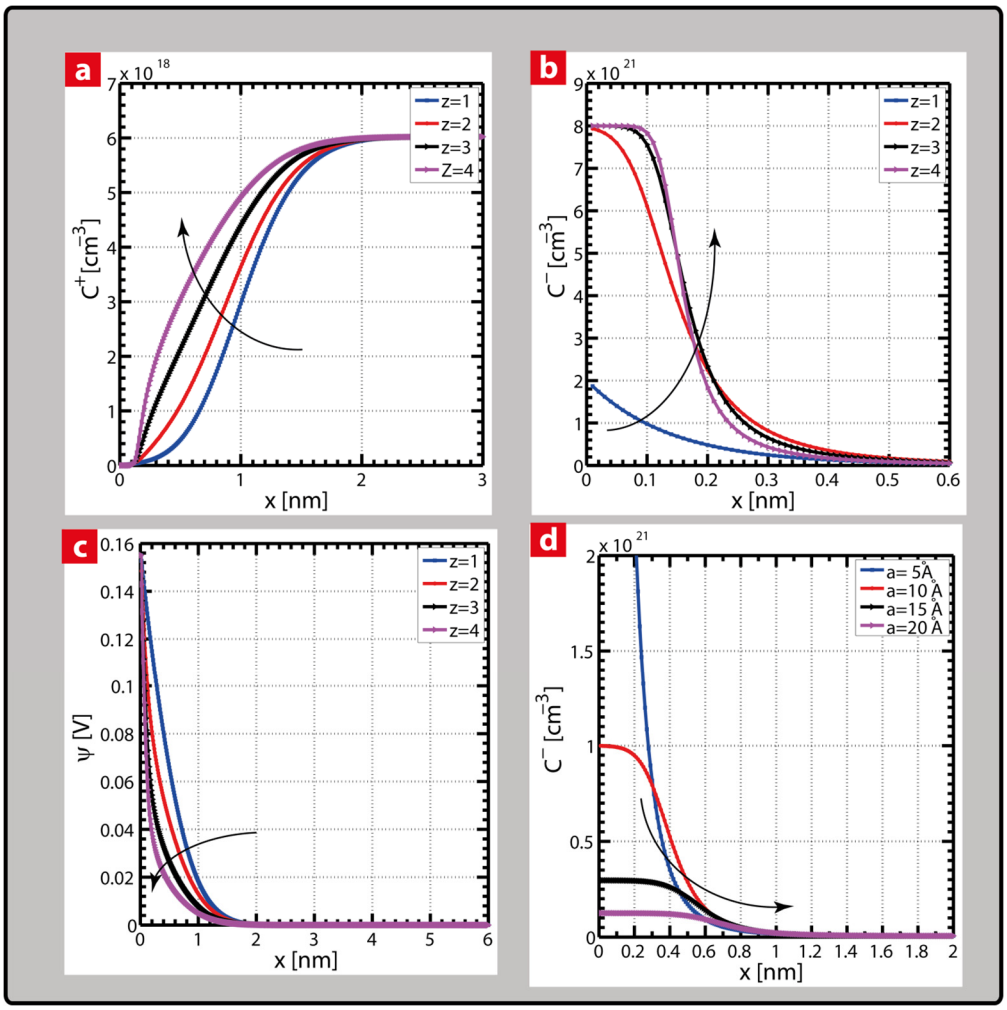

Figure 34: PB model including effect of ion size. (a) Co-ion and (b) counter ion density profiles for varying anionic valency as a function of distance from the electrode interface to an applied ψ_O of $150\,mV$ in a 1:z electrolyte. The size of the ion is $5\,\mathring{A}$. As the valency increases, the counterion decay is more abrupt but results in a saturation of charge density at the interface, (c) Potential distribution for varying valency. (d) Role of varying the hydrated ion size. As the ionic radius increases the maximum achievable charge density at the interface reduces due to the Steric effect.

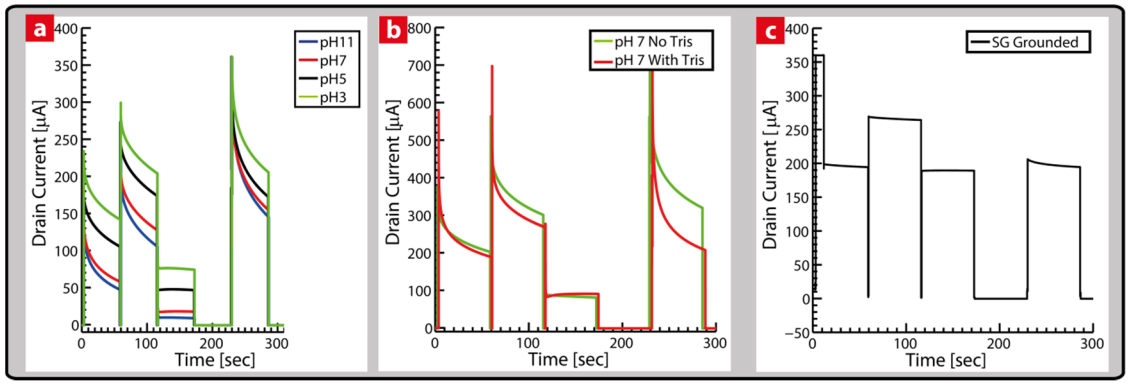

Figure 35: (a) High resolution transient recording showing variation in drain current for the CG pulse train (described in the main body) for variations in pH_B. The increase in the current levels after the application of -15V on the CG is attributed to surface protonation resulting in a remnant positive ψ_O, (b) Effect of adding a competing solution buffer (Tris buffer) at pH_B 7. The current level after the application of -15V does not increase to the same extent as before owing to scarcity of available protons, (c) transient current with the SG directly probed and CG pulsed. The current levels before and after the +15V and -15V CG pulse remain the same, indicating a charge neutral FG condition.

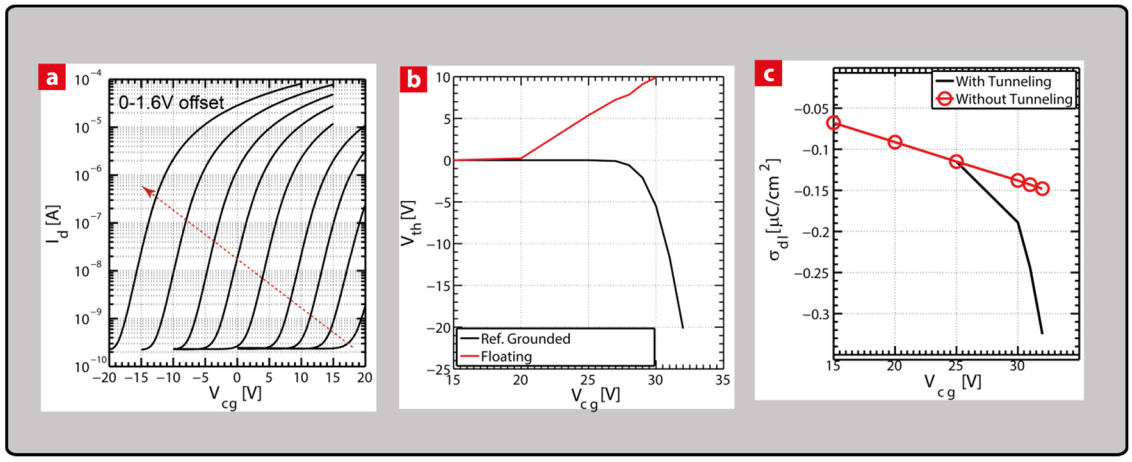

Figure 36: Typical capacitive amplification ratio experimentally extracted by modulating the electrolyte and probing the channel current via V_{CG}. The extracted ratio above has an amplification factor of ~20 (b) Simulation of the tunneling characteristic showing the difference between V_{REF} being pinned and floating. Pinning V_{REF} results in hole storage on the FG while floating V_{REF} results in electron storage when the CG is pulsed. (c) Change in electrolyte charge when V_{CG} is pulsed shows that tunneling serves as a boost to twice the charge modulation in comparison with pure capacitive charging.

Table 3: CvMOS equation set.

$I = I_o e^{\frac{\kappa V_{FG}}{U_T}} (e^{\frac{-V_S}{U_T}} - e^{\frac{-V_D}{U_T}})$	Drain current in subthreshold
where U_T is the thermal voltage	
$\kappa = \frac{C_{OX}}{C_{OX} + C_{dep}}$	Channel coupling coefficient
$I = \frac{\mu C_{OX} W}{2L} (V_{FG} - V_{TFG})^2$	Drain current in saturation
$V_{FG} = \frac{Q}{C_T} + \frac{C_{gs}}{C_T} V_S + \frac{C_{gd}}{C_T} V_D + \frac{C_{CG}}{C_T} V_{CG} + \frac{C_{SG}}{C_T} V_{SG}$	Floating gate potential
$C_T = (\frac{C_{OX} * C_{dep}}{C_{OX} + C_{dep}}) + C_b + C_{gs} + C_{gd} + C_{CG} + C_{SG}$	Total floating gate capacitance
$S = \frac{U_T * \ln(10)}{\kappa} (\frac{C_T}{C_{SG}})$	Subthreshold slope
$A_C = \frac{\frac{W_{SG} L_{SG} * \varepsilon_{ox}}{t_{ox}} // C_{dl}}{\frac{W_{CG} L_{CG} * \varepsilon_{ox}}{t_{ox}}}$	Capacitive amplification ratio
$\Delta V_{TCG} = \frac{-Q}{C_T} - \frac{C_{gs}}{C_T} V_S - \frac{C_{gd}}{C_T} V_D - A_C V_{SG}$	Shift in threshold voltage seen from control gate

References

[1] M. S. Kilic, M. Z. Bazant, and A. Ajdari, Phys.Rev.E **75**, 021502 (2007).

APPENDIX-B

Supporting information for chapter-3 includes details of the instrumentation set up, control experiments for DNA hybridization experiments and Simulation of the DNA transistor impedance model. Tables outlining the oligonucleotides used and equation set describing the working of the *CυMOS* transistor are also included.

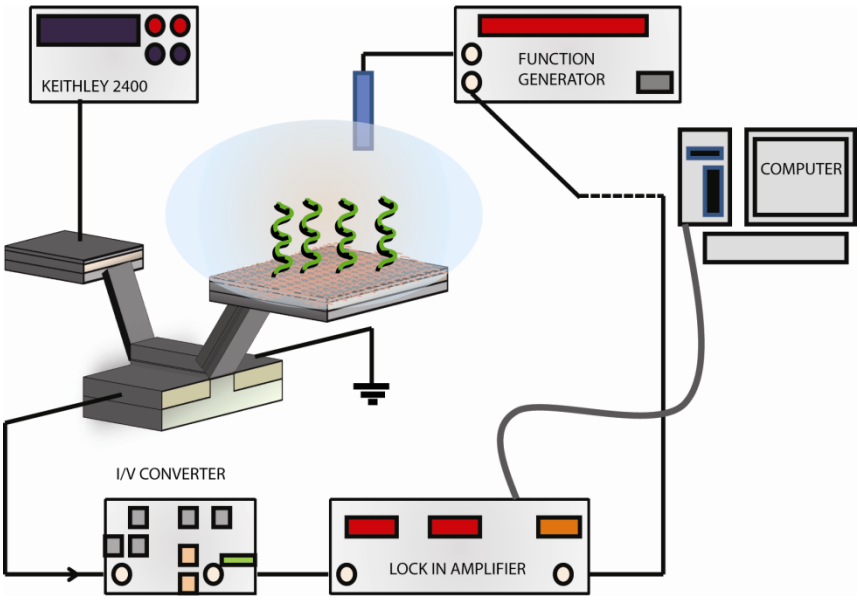

Figure 37: Impedance spectroscopy setup showing the ac small signal parameters monitored through a lock-in amplifier.

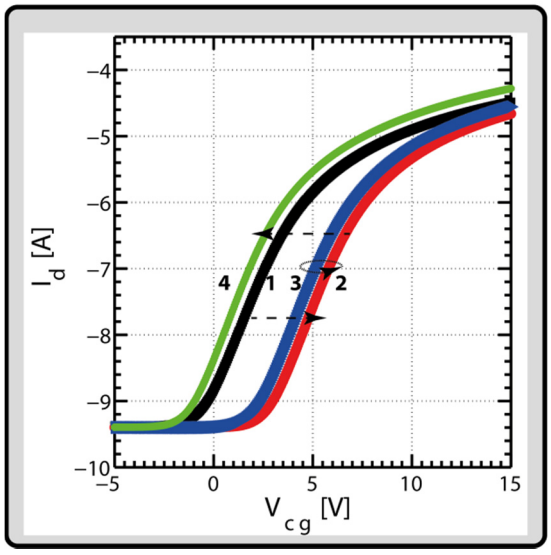

Figure 38: Effect of repeated cycling of the tunneling electrons after DNA immobilization with and without buffer exchange. IV sequence: (1) Electrons tunneled out with NaCl on sensing surface alone; (2) Pre annealed dsDNA (C1,C2) immobilized; (3) Electrons tunneled in and then out without buffer exchange; (4) Electrons tunneled in , buffer exchanged and electrons subsequently tunneled out indicating a refreshed surface.

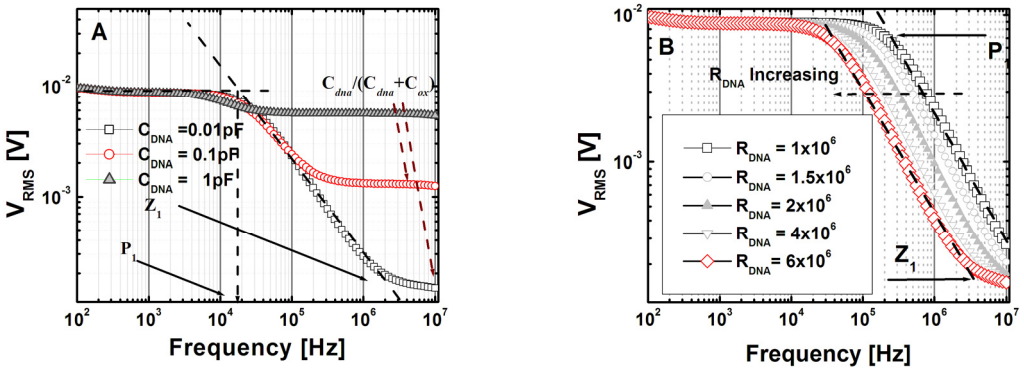

Figure 39: (a) SPICE simulations using the split gate frequency response of CvMOS with DNA immobilized. P_1 is shown to have a very negligible effect on the capacitance of the adsorbed film whereas Z_1 shifts in significantly. (b) When the interfacial resistance is varied we observe a parallel shift in the bode response. P1 shifts significantly.

Table 4: Various DNA strand sequences and associated lengths used for experimental runs in Chapter 3.

Type	DNA sequence
B1 (20bP ssDNA) probe	5'-CATAGGCCTTGGAACCTATG-3’
B2 (20bP ssDNA) target	5'-CATAGGTTCCAAGGCCTATG-3’
C1 (24bP ssDNA) probe	5’-GCATCTGGGCTATAAAAGGGCGTCG-3’
C2 (24bP ssDNA) target	5’-CGACGCCCTTTTATAGCCCAGATGC-3’
D1 (48bP ssDNA) probe	5’-GCATCTGGGCTATAAAAGGGCGTCGGTATCCAAGGTTCCGGATACGAG-3’
D2 (48bP ssDNA) target	5’-CTCGTATCCGGAACCTTGGATACCGACGCCCTTTTATAGCCCAGATGC-3’

Table 5: CvMOS equation set.

$I = I_o e^{\frac{\kappa V_{FG}}{U_T}} (e^{\frac{-V_S}{U_T}} - e^{\frac{-V_D}{U_T}})$	Drain current in subthreshold
where U_T is the thermal voltage	
$\kappa = \frac{C_{OX}}{C_{OX} + C_{dep}}$	Channel coupling coefficient
$I = \frac{\mu C_{OX} W}{2L} (V_{FG} - V_{TFG})^2$	Drain current in saturation
$V_{FG} = \frac{Q}{C_T} + \frac{C_{gs}}{C_T} V_S + \frac{C_{gd}}{C_T} V_D + \frac{C_{CG}}{C_T} V_{CG} + \frac{C_{SG}}{C_T} V_{SG}$	Floating gate potential
$C_T = (\frac{C_{OX} * C_{dep}}{C_{OX} + C_{dep}}) + C_b + C_{gs} + C_{gd} + C_{CG} + C_{SG}$	Total floating gate capacitance
$S = \frac{U_T * \ln(10)}{\kappa} (\frac{C_T}{C_{SG}})$	Subthreshold slope
$A_C = \frac{\frac{W_{SG} L_{SG} * \varepsilon_{ox}}{t_{ox}} // C_{dl}}{\frac{W_{CG} L_{CG} * \varepsilon_{ox}}{t_{ox}}}$	Capacitive amplification ratio
$\Delta V_{TCG} = \frac{-Q}{C_T} - \frac{C_{gs}}{C_T} V_S - \frac{C_{gd}}{C_T} V_D - A_C V_{SG}$	Shift in threshold voltage seen from control gate

APPENDIX-C

Supporting information for chapter-4 contains information on control experiments for frequency mode biosensing performed on floating gate ISFET's.

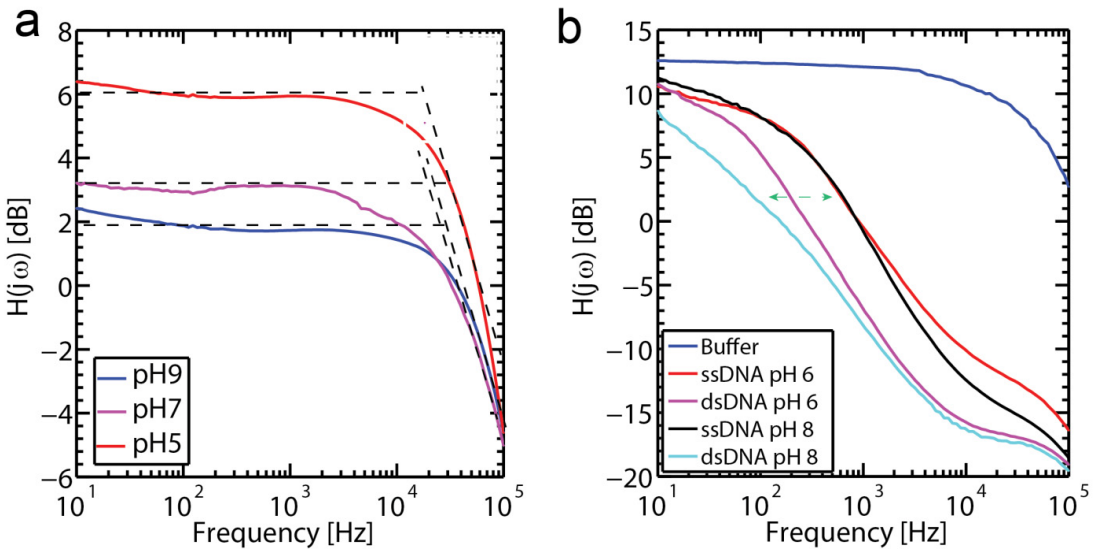

Figure 40: (a) Bode responses performed under different pH_B conditions. Notice how the pole (p2) (the only pole in the system) does not shift with varying bulk pH_B for pH insensitivity. (b) DNA hybridization under different pH_B conditions. The increase in capacitance upon complementary strand addition is similar, although a slight increase in interfacial resistance at pH=8 is observed. This increase in resistance is within the error bar in this frequency mode of operation (not shown).

APPENDIX-D

Supporting information for chapter-5 contains control experiments on electrolytes, Y-DNA and AuNP's corroborating experiments presented in the main manuscript.

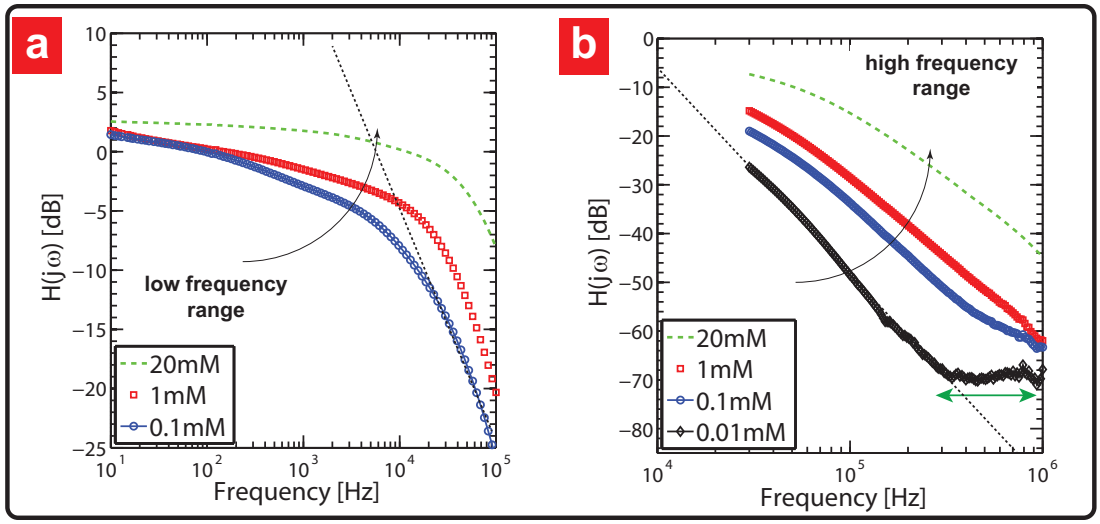

Figure 41: (a) Low and (b) High frequency response of the CvMOS under different background saline conditions. Arrows indicate direction of increasing salt concentration. Notice how the solution resistance determines the effective bandwidth of the measurement. Under extremely low salt conditions and high frequency perturbation the transistor appears to completely stop responding to the input frequency (green arrow) and is effectively cut-off due to the large input gate resistance (b).

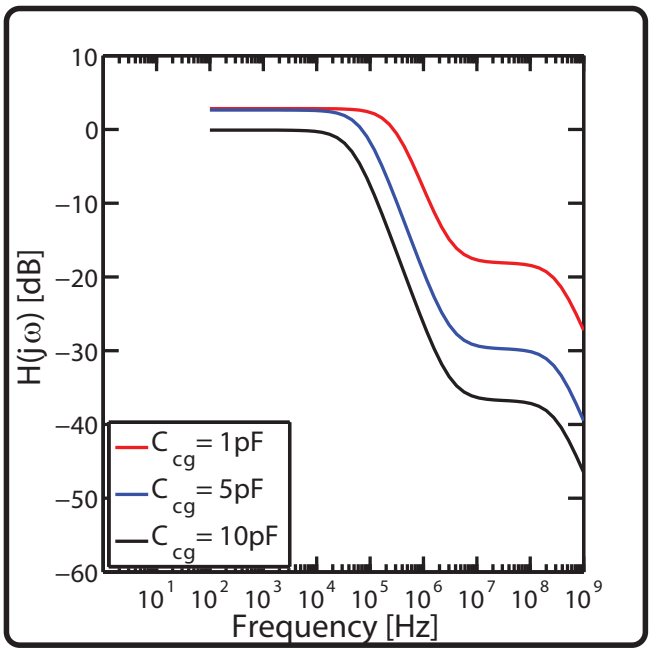

Figure 42: Effect of scaling C_{CG} on the overall frequency response; Increasing C_{CG} shifts p1 in to lower frequencies while z1 is not affected.

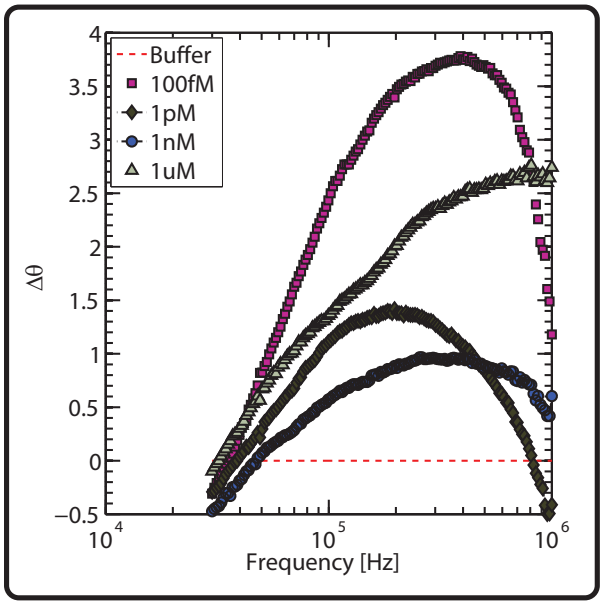

Figure 43: High frequency phase response of the CvMOS under different target conditions with AuNP and Y-DNA present. Notice the clear peak in the response indicative of a "molecular resonance" due to enhanced molecular mass. A slight concentration dependent shift in relaxation frequency is observed.

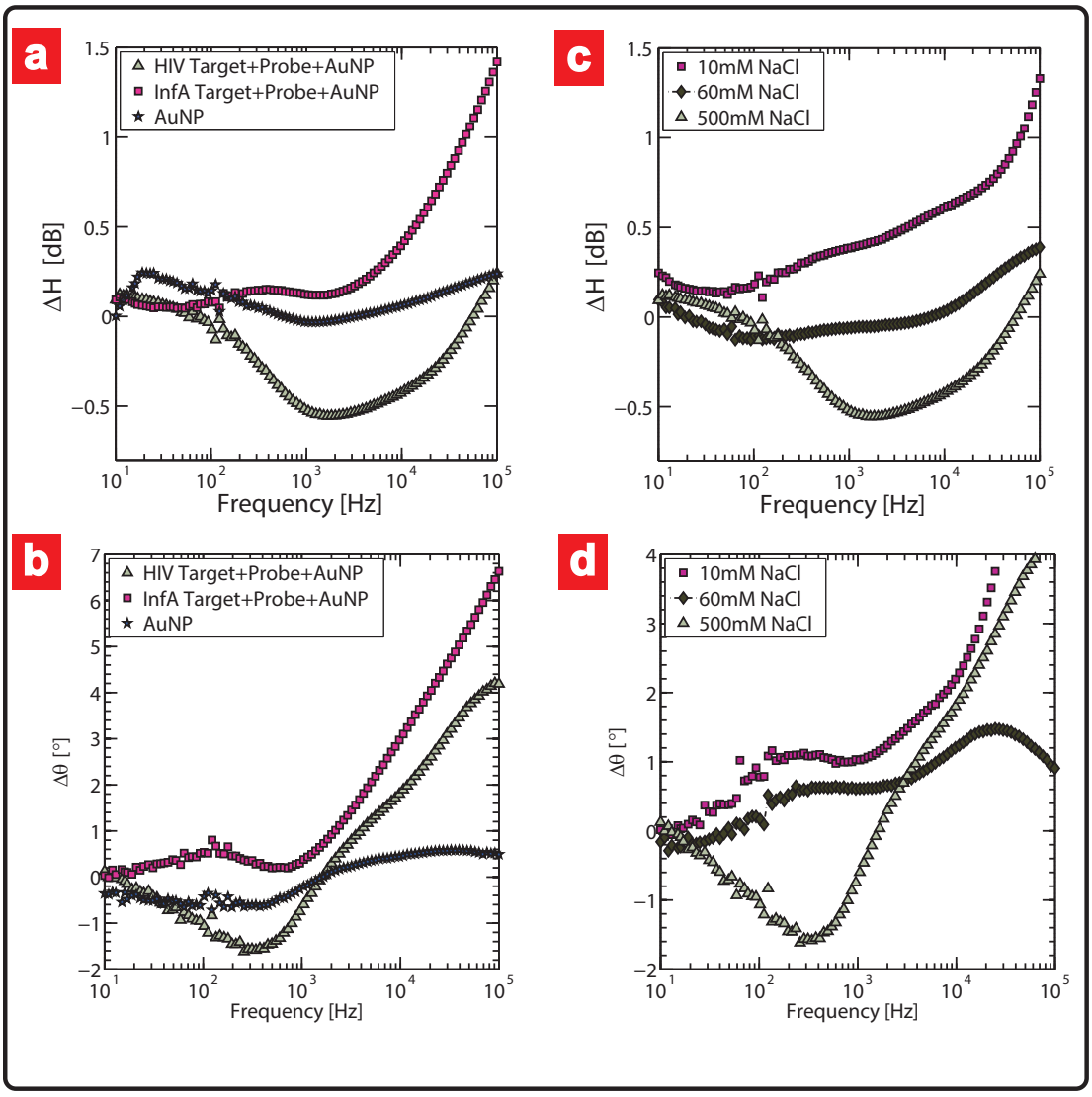

Figure 44: Magnitude and phase response of the CvMOS with AuNP-Y_DNA-Target fragments under different control conditions, (a-b) different target conditions (c-d) different saline conditions. (a, b) With wrong or in the absence of target, the trough in the response disappears and a peak begins to appear indicating less aggregate formation and lower interfacial resistance respectively. (c,d) The effect of varying background saline conditions clearly depicts reduction in the trough with decreasing salt concentrations clearly showing that higher saline conditions result in more pronounced aggregate formation due to enhanced hybridization efficiency.

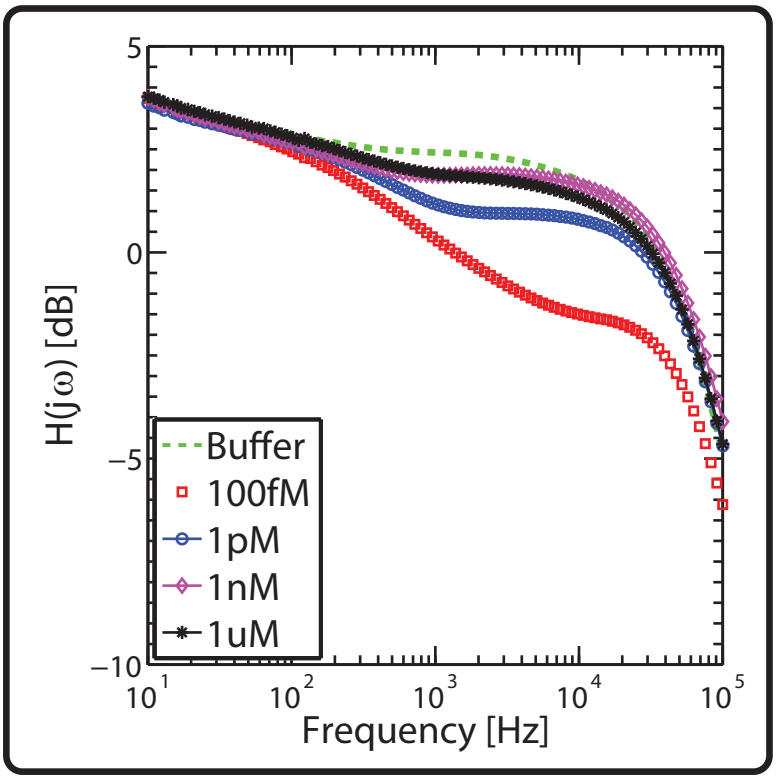

Figure 45: Impedance response with AuNP-Y-DNA aggregates present on the SG surface. Various curves indicate different target conditions. As target concentrations increase the interfacial resistance decreases indicating larger aggregates and less free DNA.

APPENDIX-E

Supporting information for chapter-6 outlines the overall transistor transfer function and a figure of the point contact model which is used to model action potential activity outlined in the main manuscript.

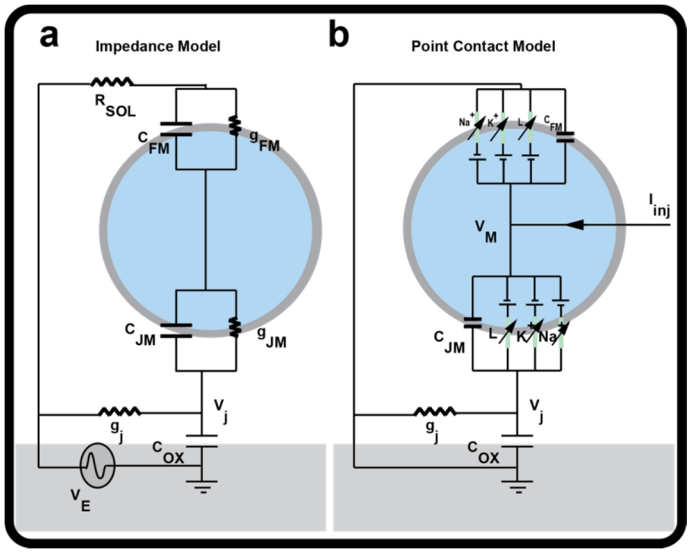

Figure 46: (a) Impedance model of the cell-transistor interface and (b) the point contact model describing the methodology to simulate the ionic waves in the cell transistor cleft.

The equivalent circuit shown in Figure 46(a) is used for impedimetric analysis when working both ISFET and CvMOS. With the ISFET, C_{OX} serves as the gate capacitance of the transistor while with the CvMOS, using the split excitation technique, the CG serves as AC ground and the overall C_{OX} is given by $C_{OX} = \frac{(C_{tun} + C_{CG}) \times C_{SG}}{(C_{tun} + C_{CG}) + C_{SG}}$ where C_{tun} is the tunnel oxide capacitance and C_{tun} is the sensing gate capacitance.

The transfer function, $H(j\omega)$ for the circuit shown in Fig. 46(a) can be given by,

$$H(j\omega)=\frac{(1+g_j R_{sol})(j\omega C_{FM}+g_{FM})(j\omega C_{JM}+g_{JM})+g_j((C_{FM}+C_{JM})j\omega+g_{FM}+g_{JM})}{(1+R_{sol}(g_j+j\omega C_{OX}))(j\omega C_{FM}+g_{FM})(j\omega C_{JM}+g_{JM})+(g_j+j\omega C_{OX})((C_{FM}+C_{JM})j\omega+G_{FM}+G_{JM})}$$

Neglecting g_{FM} and g_{JM} , the first zero and the first two poles can be determined as,

$$z1=\frac{g_j}{C_{Meff}}\frac{1}{1+g_j R_{sol}}$$

$$p1=\frac{g_j}{C_{Meff}}\frac{1}{1+g_j R_{sol}+C_{OX}/C_{Meff}}$$

$$p2=\frac{1+g_j R_{sol}+C_{OX}/C_{Meff}}{R_{sol}C_{OX}}$$

Where C_{Meff} is the parallel combination of C_{JM} and C_{FM} . If R_{sol} is negligible, further simplifications directly reflect the influence of C_{Meff} and g_j .